Scuola di Scienze
Corso di Laurea Magistrale in Fisica

STABLE LASER AND UPGRADED VACUUM SETUP FOR AN EXPERIMENT WITH ULTRACOLD ATOMS

Relatore: Presentata da:
Prof. Elisa Ercolessi   Luca Lorenzelli

Correlatore:
Dott. Francesco Minardi

Contents

Abstract

In questo lavoro ci si propone di descrivere la realizzazione di un sistema laser con cavitá esterna e di un apparato da ultra-alto-vuoto, che verranno impiegati in un esperimento di miscele di atomi ultrafreddi che utilizza due specie atomiche di bosoni: ^{87}Rb e ^{41}K. Speciale attenzione viene rivolta verso le caratteristiche dello schema utilizzato e sul sistema di controllo in temperatura, che rendono questo sistema laser particolarmente stabile in frequenza e insensibile alle vibrazioni e variazioni di temperatura. Si sono poi analizzate le proprietá dei materiali impiegati e delle procedure sperimentali adottate per la realizzazione del nuovo apparato da vuoto, al fine di garantire migliori prestazioni rispetto al sistema attualmente in uso.

Introduction

The starting point for the prediction of Bose-Einstein condensation has to be looked for in Bose historic paper of 1924, where he derived Plack's formula by a treatment of black-body radiation as a gas of photons. Einstein argued that what Bose had implied for photons should be true for material particles as well, and he defined Bose's derivation of Planck's formula as an important step towards the quantum theory of ideal gases. In two papers, published soon after that of Bose, Einstein extended Bose's method to the study of an ideal gas and thereby developed what is now known as Bose-Einstein statistics. The first prediction of Bose-Einstein condensation dates back to the second paper (1925), in which Einstein, considering a gas of non-interacting massive bosons, predicted that, below a certain critical temperature, a finite fraction of the total number of particles would occupy the same lowest-energy single-particle quantum state.

Since that time, the first Bose-Einstein condensate (BEC) was produced 70 years later, thanks to the powerful laser-cooling methods developed in those years. If solids are considered, due to their high atomic density (of order 10^{22} cm^{-3}), quantum effects become strong for electrons in metals below the Fermi temperature, which is typically $10^4 - 10^5$ K. On the other hand, to observe quantum phenomena in dilute atomic gases (the particle density in a Bose-Einstein condensate is typically $10^{13} - 10^{15}$ cm^{-3}), temperatures lower than 10^{-6} K are required and this has for such a long time prevented their observation.

13 years after Einstein's paper, London adopted the phenomenon of Bose-Einstein condensation to develop his Two-Fluid theory for the explanation of liquid ^{4}He superfluid behaviour at low temperatures. Helium liquids were also the first attractive systems for experimental realization of Bose-Einstein condensates, as the temperatures required for observing quantum phenomena are of order 1 K. On the other hand, due to the strong correlations induced by the interactions between ^{4}He atoms, only a reduced fraction (of order 10%) of the total number of atoms can occupy the zero-momentum state, even at absolute zero, with consequent difficulties in its detection.

This led to the search for weakly-interacting Bose gases with a higher condensate fraction, and spin-polarized hydrogen was considered a good candidate for this purpose. Indeed, the attractive interaction between two

hydrogen atoms with their electronic spins aligned was estimated to be so weak that a gas of hydrogen atoms in a magnetic field would be stable against formation of molecules and would thus remain in the gaseous state to arbitrary low temperatures. Since hydrogen can't be laser cooled, cryogenic techniques to force atoms against cold surfaces were employed to realize a precooled state. Nevertheless, interactions of hydrogen with the surface limited the densities achieved in the early experiments and only in 1998 it was possible to realize for the first time a hydrogen atoms Bose-Einstein condensate (the first attempt to realize a BEC with hydrogen atoms was at Massachusetts Institute of Technology MIT where, for the first time, magnetic techniques for atoms trapping were developed). Besides laser cooling techniques, a peculiar process that allow to achieve the low temperatures and high densities required for the onset of Bose-Einstein condensation, is an evaporative cooling stage of magnetically trapped gases, in which the more energetic atoms are removed from the trap, thereby cooling the remainings. Finally, as a consequence of the progress made in laser cooling of alkali atoms and evaporative cooling techniques, the first gaseous Bose-Einstein condensates for rubidium, sodium and lithium were realized in 1995. A peculiar feature of this kind of systems is the possibility to manipulate them by the use of lasers and magnetic fields, that allow for example to study their behaviour, while varying the interactions between atoms exploiting Feshback resonances.

The reason why the physics of ultracold atoms is still nowadays an important field of theoretical and experimental research, is because ultracold gases loaded into optical lattices can provide highly controlled quantum systems for simulations of other quantum systems. Bose-Einstein condensates give the unique opportunity for exploring quantum phenomena on a macroscopic scale and ultracold atoms in optical lattices can be used for condensed matter physics simulations, as their behaviour is similar to that of electrons in solids, where the real periodic potential formed by the ions is replaced by an artificial crystal potential formed by an optical lattice. Indeed, although these systems are quite different in the absolute energy and length scales, one can use ultracold atoms to implement the model Hamiltonians that have long been studied in the context of strongly correlated electronic systems. Furthermore, they constitute a clean system without any lattice defect and show a high scalability, in that, with such systems, it is possible to tune the lattice parameters over a wide range, with a high degree of controllability. Besides the quantum simulation aspect, recent experiments on ultracold atoms in optical lattices (such as single-site resolution imaging techniques), have opened the door to quantum information processing, due to their long coherence times.

Eventually, two basic, but at the same time fundamental aspects concerning ultracold atoms experiments are the laser and vacuum techniques. Indeed, these experiments require an extremely high degree of vacuum, in

the range of ultra-high-vacuum (i.e. pressures of the order of 10^{-11} mbar), to prevent thermalization between the atoms and the walls of the experimental apparatus, through collisions with the particles of the residual gas. Such extremely low values for the pressure involves a careful choice of the building materials, as well as the requirement to optimize the experimental techniques for the realization of vacuum systems. In the same way, laser cooling is of crucial importance and the great number of lasers involved in these experiments, as well as the complexity of the optical elements setup, imply inexpensive ways to realize compact laser systems with high reliability, expecially as far as their wavelength stability, tunability and output power are concerned. It is for this reason that so basic experimental aspects, like vacuum and laser techniques, are at the same time so important in ultracold atoms experiments and need a continuous research aimed to improve their performance.

The purpose of this thesis is to present the development of a particularly stable external-cavity diode laser that uses an interference filter as wavelength selector and of an upgraded vacuum system, that will be employed in an experiment with ultracold atoms that involves two different species of bosonic alkali atoms: ^{87}Rb and ^{41}K. The systems described in the present work involve new and advanced techniques in their respective fields. They are aimed to the specific necessities of a laser for cooling ^{87}Rb atoms, that has to be particularly stable against mechanical vibrations and thermal fluctuations, in order to ensure the best performance. The aged vacuum apparatus currently in use needs to be improved with a new one, that should guarantee a better optical access for laser interaction with atoms and the use of high-intensity trapping magnetic fields, without residual magnetization effects. The introduction given in this thesis will concern an upgraded vacuum system, that makes use of advanced materials for ultra-high-vacuum (UHV) technology, so that the lowest level of residual gas particles released from material surfaces and the minimization of mechanical stresses due to thermal strains, at the interface of different materials, can be achieved.

As far as the organization of this work is concerned, chapter 1 gives an introduction to the quantitative description of Bose-Einstein condensation in dilute gases. We will deal first with the ideal case, while interactions will be introduced in sections 1.3 and 1.4, where the Gross-Pitaevskii equation and the Thomas-Fermi approximation will be presented.

Chapters 2 and 3 are devoted to the description of my experimental work at the European Laboratory for Non-Linear Spectroscopy (LENS), at the University of Florence. Sections 2.1 and 2.2 introduce to the theory of interference-filter-stabilized external-cavity diode lasers and section 2.3 gives the details of our system, that provides advantages for what concerns the wavelength stability and the optical feedback optimization, with respect to the common grating-stabilized diode lasers previously used. Section 2.4 gives then the detailed description of the feedback system for the

diode's temperature control, that includes the software implementation of LabVIEW projects on the Field Programmable Gate Array (FPGA) chip and Real-Time processor of a National Instruments device. Finally, in section 2.5, we will report and discuss the results attained with our system.

Chapter 3 is focussed on the realization of an ultra-high-vacuum (UHV) system: section 3.1 introduces the basic concepts that concern vacuum technology. Section 3.2 describes the setup of our system, with particular attention to the behaviour of materials in UHV and points out the main features that make titanium vacuum chambers (like the one we used) particularly suitable for UHV applications. Eventually, in subsection 3.2.4 and section 3.3, we will analyze the results obtained from the characterization of our system and give hints aimed to improve the vacuum setup experimental techniques developed in this work.

Chapter 1

Bose-Einstein condensation

1.1 Bose - Einstein condensation in non interacting systems

Consider an ideal Bose gas with a fixed number of particles N, i.e. subject to the constraint

$$N = \sum_{\varepsilon=0}^{+\infty} n_\varepsilon \tag{1.1}$$

The Bose-Einstein statistics for the mean occupation number of single-particle states is

$$< n_\varepsilon > = \frac{1}{e^{\frac{(\varepsilon-\mu)}{k_B T}} - 1} \tag{1.2}$$

which means that we must have $\mu < l \quad \varepsilon$, $\forall \varepsilon$ (otherwise unphysical negative populations may result). For $\mu < \varepsilon_{min} = 0$, all values of $(\varepsilon - \mu)$ are positive and the behaviour of all $< n_\varepsilon >$ is nonsingular.

In the high temperature limit, the quantum Bose-Einstein and Fermi-Dirac statistics $(< n_\varepsilon > = \frac{1}{e^{\frac{(\varepsilon-\mu)}{k_B T}} \mp 1})$ tend to behave in the same classical fashion, described by the Maxwell-Boltzmann statistics $(< n_\varepsilon >_{M.B.} = e^{\frac{(\varepsilon-\mu)}{k_B T}})$.

This is equivalent to the non-degeneration condition

$$e^{\frac{(\varepsilon-\mu)}{k_B T}} >> 1 \tag{1.3}$$

which physical meaning is that the probability of double occupance is negligible for any of the single-particle levels ε

$$< n_\varepsilon > << 1 \quad \forall \varepsilon \tag{1.4}$$

For bosons, condition 1.3 implies that μ, the chemical potential of the system, must be negative and large in magnitude. This means that the fugacity $z \equiv e^{\frac{\mu}{k_B T}}$ of the system must be much smaller than unity.

One can see [2] that this is equivalent to the requirement

$$n\lambda^3 << 1 \tag{1.5}$$

where $n = \frac{N}{V}$ is the total density of particles and $\lambda = \dfrac{h}{(2\pi m k_B T)^{\frac{1}{2}}}$ is the thermal deBroglie wavelength.

On the other hand, when the temperature tends to zero, μ becomes equal to the lowest value of ε. In this regime the non-degeneration condition 1.3 breaks down and the occupancy of the single-particle ground-state $\varepsilon = 0$ becomes infinitely high, leading to the phenomenon of Bose-Einstein condensation.

A statistical treatment of an ideal Bose gas provides the thermodynamic expressions

$$\frac{PV}{k_B T} \equiv ln Z(z, V, T) = -\sum_{\varepsilon} ln(1 - ze^{-\beta\varepsilon}) \tag{1.6}$$

$$N \equiv \sum_{\varepsilon} <n_\varepsilon> = \sum_{\varepsilon} \frac{1}{z^{-1}e^{\beta\varepsilon} - 1} \tag{1.7}$$

with $Z(z, V, T)$ the grand partition function of the system.

If we consider the thermodynamic limit $(N, V \to \infty; \frac{N}{V} = n = const)$, the spectrum of the single-particle states is almost a continuum one and the summations may be replaced by integrations, according to

$$\frac{1}{V}\sum_{\varepsilon} \to \frac{2\pi}{h^3}(2m)^{\frac{3}{2}} \int_0^\infty \varepsilon^{\frac{1}{2}} d\varepsilon \tag{1.8}$$

where $g(\varepsilon)d\varepsilon \simeq \frac{V}{h^3}(2m)^{\frac{3}{2}}\varepsilon^{\frac{1}{2}}d\varepsilon$ is the number of single-particle states in the infinitesimal range from ε to $\varepsilon + d\varepsilon$.

We observe that, taking the thermodynamic limit, we are giving a weight zero to the ground energy level $\varepsilon = 0$. As in a quantum mechanical treatment we must give a statistical weight unity to each nondegenerate single-particle state in the system, it is advisable to take this particular state out of the sum before carrying out the integration. We thus obtain the general expressions:

$$\frac{P}{k_B T} = -\frac{2\pi}{h^3}(2m)^{\frac{3}{2}}\int_0^\infty \varepsilon^{\frac{1}{2}} ln(1 - ze^{-\beta\varepsilon})d\varepsilon - \frac{1}{V}ln(1-z) \tag{1.9}$$

$$\frac{N}{V} = \frac{2\pi}{h^3}(2m)^{\frac{3}{2}}\int_0^\infty \frac{\varepsilon^{\frac{1}{2}}d\varepsilon}{z^{-1}e^{\beta\varepsilon} - 1} + \frac{1}{V}\frac{z}{1-z} \tag{1.10}$$

Since, from equation 1.2: $\frac{z}{1-z} = N_0$ (number of particles in the ground state $\varepsilon = 0$) and hence $z = \frac{N_0}{N_0+1}$, the last term in equation 1.9 is equal to $\frac{1}{V} ln[(N_0 + 1)^{-1}]$, and we can neglect it for all values of z.

Now, substituting $\beta \varepsilon = x$ and taking into account that $\frac{1}{V}\frac{z}{1-z} = \frac{N_0}{V}$, we can rewrite expressions 1.9 and 1.10 in terms of Bose-Einstein functions, defined by:

$$g_\nu(z) = \frac{1}{\Gamma(\nu)} \int_0^\infty \frac{x^{\nu-1}dx}{z^{-1}e^x - 1} \qquad (1.11)$$

where $\Gamma(\nu) = \int_0^\infty e^{-x}x^{\nu-1}dx$.
Thus:

$$\frac{P}{k_BT} = -\frac{2\pi(2mk_BT)^{\frac{3}{2}}}{h^3} \int_0^\infty x^{\frac{1}{2}} ln(1 - ze^{-x})dx = \frac{1}{\lambda^3}g_{\frac{5}{2}}(z) \qquad (1.12)$$

$$\frac{N - N_0}{V} = \frac{2\pi(2mk_BT)^{\frac{3}{2}}}{h^3} \int_0^\infty \frac{x^{\frac{1}{2}}dx}{z^{-1}e^x - 1} = \frac{1}{\lambda^3}g_{\frac{3}{2}}(z) \qquad (1.13)$$

This last equation determines the value of the fugacity z.

From these expressions we can calculate other thermodynamic quantities, such as the internal energy

$$U \equiv -(\frac{\partial}{\partial\beta}lnZ)_{z,V} = k_BT^2\Big[\frac{\partial}{\partial T}(\frac{PV}{k_BT})\Big]_{z,V} = k_BT^2Vg_{\frac{5}{2}}(z)\Big[\frac{d}{dT}(\frac{1}{\lambda^3})\Big] = \frac{3}{2}k_BT\frac{V}{\lambda^3}g_{\frac{5}{2}}(z)$$
$$(1.14)$$

and the specific heat of the gas

$$\frac{C_V}{Nk_B} \equiv \frac{1}{Nk_B}\Big(\frac{\partial U}{\partial T}\Big)_{N,V} = \frac{3}{2}\Big[\frac{\partial}{\partial T}\Big(\frac{PV}{Nk_B}\Big)\Big] \qquad (1.15)$$

From these expressions we can determine the equation of state for the system:

$$P = \frac{2}{3}\Big(\frac{U}{V}\Big) \qquad (1.16)$$

Let us now consider one first step far from the classical limit.

When $z << 1$, we can expand Bose-Einstein functions as

$$g_\nu(z) = z + \frac{z^2}{2^\nu} + \frac{z^3}{3^\nu} + ... \qquad (1.17)$$

If we neglect N_0 in comparison with N and invert the series in 1.13, we obtain an expansion for z in powers of $n\lambda^3$. Then, substituting this into the series appearing in 1.12, it takes the form of the virial expansion

$$\frac{PV}{Nk_BT} = \sum_{l=1}^{+\infty} a_l \left(\frac{\lambda^3}{v}\right)^{l-1} \tag{1.18}$$

where $v \equiv \frac{1}{n}$ is the volume per particle and a_l are the virial coefficients of the system.

The specific heat is expressed as

$$\frac{C_V}{Nk_B} = \frac{3}{2} \sum_{l=1}^{+\infty} \frac{5-3l}{2} a_l \left(\frac{\lambda^3}{v}\right)^{l-1} \tag{1.19}$$

We observe that, as $T \to \infty$ (and hence $\lambda \to 0$), both the pressure and the specific heat of the gas approach their classical values: nk_BT and $\frac{3}{2}Nk_B$, respectively.

We are now going to consider another situation, in which z increases and assumes values close to unity, so that expansion 1.17 is no longer valid.

We see that the term $\frac{z}{(1-z)V}$ (which is identically equal to $\frac{N_0}{V}$, N_0 being the number of particles in the ground state $\varepsilon = 0$) can become a significant fraction of the quantity $\frac{N}{V}$.

The physical meaning of this result is that a macroscopic fraction of particles occupy the quantum single-particle state $\varepsilon = 0$.

Expansions such as 1.18 and 1.19 do not remain useful and we have to work with the general thermodynamic expressions 1.12, 1.13 and 1.14. From 1.13 we can express the number of particles in the excited states

$$N_e = V \frac{(2\pi m k_B T)^{\frac{3}{2}}}{h^3} g_{\frac{3}{2}}(z) \tag{1.20}$$

As $T \to 0$, $z = \frac{N_0}{N_0+1} \to \frac{N}{N+1} \simeq 1$ and, as $g_{\frac{3}{2}}(z)$ is a monotonically increasing function of z (its largest value being $g_{\frac{3}{2}}(1) \equiv \zeta(\frac{3}{2}) \simeq 2,612$), the total number of particles inl the excited states is bounded by

$$N_e \leq V \frac{(2\pi m k_B T)^{\frac{3}{2}}}{h^3} \zeta(\frac{3}{2}) \tag{1.21}$$

As long as the actual number of particles in the system is less than this limiting value, nearly all the particles in the system are distributed over the excited states and the precise value of z is determined by equation 1.20. However, for a higher number of atoms, the exiding ones will be pushed into the ground state $\varepsilon = 0$:

$$N_0 = N - \left[V \frac{(2\pi m k_B T)^{\frac{3}{2}}}{h^3} \zeta(\frac{3}{2}) \right] \tag{1.22}$$

Hence, the condition for the onset of Bose-Einstein condensation is

$$N > VT^{\frac{3}{2}} \frac{(2\pi m k_B)^{\frac{3}{2}}}{h^3} \zeta(\frac{3}{2}) \qquad (1.23)$$

or, if we hold N and V constant and vary T

$$T < T_C = \frac{h^2}{2\pi m k_B} \left[\frac{N}{V\zeta(\frac{3}{2})} \right]^{\frac{3}{2}} \qquad (1.24)$$

T_C is a characteristic temperature that depends on the mass of the particles m and on the density $\frac{N}{V}$ of the system. One characteristic feature is that, at T_C, the thermal wavelength $\lambda = \frac{h}{(2\pi m k_B T)^{\frac{1}{2}}}$ is comparable to the interparticle spacing.

1.2 The ideal trapped gas

Consider a vapour of nearly non-interacting atoms. The first step needed for its cooling consists of a laser cooling with three counter propagating laser beams, tuned just below the resonant frequency of the atoms in the trap (detuned towards red). With this configuration, moving atoms are Doppler shifted on resonance to the laser beam that is propagating opposite to their velocity, while atoms at rest are just off resonance and so rarely absorb a photon. Those atoms which are on resonance, then reemit photons, with a resulting net momentum kick opposite to the direction of their motion. The final result is an optical molasses that slows the atoms. This cooling method is constrained by the so called recoil limit, in which the atoms have a minimum momentum of the same order of magnitude of the momentum of the photons emploied to cool the gas. This gives a limiting temperature of $\frac{(\hbar\omega)^2}{2mc^2k_B} \simeq 1\mu K$, where ω is the frequency of the spectral line used for cooling and m is the mass of an atom.

The following step of the cooling process is an anisotropic harmonic oscillator potential trapping the atoms near the center of the magnetic trap:

$$V(r) = \frac{1}{2}m(\omega_x^2 x^2 + \omega_y^2 y^2 + \omega_z^2 z^2) \qquad (1.25)$$

(In this situation the lasers are off and the trapping frequencies ω_i are controlled by an applied magnetic field). Then, the highest energy atoms are removed by decreasing the trap barrier potential and the remainings are hence cooled by evaporation.

If the atoms in the trap are not interacting, the total Hamiltonian of the system is the sum of single-particle Hamiltonians, whose eigenvalues are the energy levels for each atom

$$\varepsilon_{l_x l_y l_z} = \hbar\omega_x l_x + \hbar\omega_y l_y + \hbar\omega_z l_z + \frac{1}{2}\hbar(\omega_x + \omega_y + \omega_z) \qquad (1.26)$$

where $l_i = 0, 1, 2, ..., \infty$ are the quantum numbers of the harmonic oscillator. Assuming a grand-canonical theory, we have, for bosons in the trap, the thermodynamic potential Π (determined from the grand canonical partition function)

$$\Pi(\mu, T) = -\frac{(k_B T)^4}{2(\hbar\omega_0)^3} \int_0^\infty x^2 ln(1 - e^{-x}e^{\beta\mu})dx = \frac{(k_B T)^4}{(\hbar\omega_0)^3}g_4(z) \qquad (1.27)$$

that allows to evaluate the avarage number of atoms in the excited states of the trap

$$N(\mu, T) = \left(\frac{\partial\Pi}{\partial\mu}\right)_T = \left(\frac{k_B T}{\hbar\omega_0}\right)^3 g_3(z) \qquad (1.28)$$

For a fixed number N of trapped atoms, the chemical potential monotonically increases as the temperature is lowered, until Bose-Einstein condensation sets up when the chemical potential reaches its highest value $\mu = 0$, at the critical temperature

$$\frac{k_B T_C}{\hbar\omega_0} = \left(\frac{N}{\zeta(3)}\right)^{\frac{1}{3}} \simeq \left(\frac{N}{1,202}\right)^{\frac{1}{3}} \qquad (1.29)$$

Observed critical temperatures are about few hundreds nK.

For $T < T_C$ we can determine the number of atoms in the excited states by separating the term representing the population of the ground state of the harmonic trap, in the expression for the total number of particles

$$N - N_0 = \sum_{l_x, l_y, l_z \neq 0}\left[\frac{1}{e^{\frac{\varepsilon_{l_x l_y l_z}}{k_B T}} - 1}\right] \qquad (1.30)$$

For $N >> 1$, the energy levels spacing $\hbar\omega_0$ becomes much smaller then the typical excitation energy $k_B T$ of the system and the previous summation can be replaced by integration

$$N - N_0 = \int \frac{d^3\vec{n}}{e^{(\frac{\hbar}{k_B T}\vec{\omega}\cdot\vec{n})} - 1} = \zeta(3)\left(\frac{k_B T}{\hbar\omega_0}\right)^3 \qquad (1.31)$$

or equivalently

$$\frac{N_{excited}}{N} = \frac{\zeta(3)}{N}\left(\frac{k_B T}{\hbar\omega_0}\right)^3 = \left(\frac{T}{T_C}\right)^3 \qquad (1.32)$$

Here $\zeta(n) = \sum_{k=1}^\infty k^{-n}$ is the Riemann Zeta function and $\vec{\omega}$, $\vec{n}$ collect the trapping frequencies and quantum numbers along each direction. At $T = T_C$ there is a zero population in the ground state and from expression 1.31 we recover 1.29, that defines the critical temperature T_C. So, below T_C, the fraction of atoms that condense into the ground state of the harmonic trap is:

$$\frac{N_0}{N} = 1 - \left(\frac{T}{T_C}\right)^3 \qquad (1.33)$$

The result is that, in the thermodynamic limit, a non zero fraction of the atoms occupy the ground state for $T < T_C$, while the occupancy fraction of each excited state is zero.

Detection of Bose-Einstein condensation is usually carried out by measuring the momentum distribution of the ultracold gas by a time of flight experiment. In this description we consider as time $t = 0$ the time at which the magnetic field is turned off and the trapping potential goes to zero. The atomic cloud can thus expand according to the momentum distribution the atoms had in the harmonic trap, for an allowed time of about $100ms$. We notice that at such low temperatures the speed of the atoms is a few millimeters per second and so the cloud expands to a few hundred microns in this period of time. The cloud is then illuminated with a resonant laser pulse, leaving a shadow on a CCD in the image plane of the optics. The size and shape of the light intensity pattern directly measures the momentum distribution the atoms had in the trap at $t = 0$. The expanding cloud can be divided into two components, the N_0 atoms that had been Bose condensed into the ground state, whose wavefunction is the product of the single-particle ground state eigenfunctions in the harmonic trap (with $n_x = n_y = n_z = 0$):

$$\Psi_0 = \prod_i \psi_0(\vec{r}_i) \qquad (1.34)$$

with $\psi_0(\vec{r}) = \left(\frac{m\omega_0}{\pi\hbar}\right)^{\frac{3}{4}} e^{-\frac{m\omega_0}{2\hbar}(\omega_x x^2 + \omega_y y^2 + \omega_z z^2)}$, and the remainings $N - N_0$ atoms that were in the excited states of the harmonic oscillator potential. The Bose-condensed atoms had smaller momenta than the atoms that were in the excited states and, after time t, the quantum evolution of the ground state has the spatial number density distribution:

$$n_0(\vec{r}, t) = N_0 |\Psi_0(\vec{r}, t)|^2 = \frac{N_0}{\pi^{\frac{3}{2}}} \prod_{j=x,y,z} \left[\frac{1}{a_j\sqrt{1 + \omega_j^2 t^2}} e^{-\frac{r_j^2}{a_j^2(1+\omega_j^2 t^2)}}\right] \qquad (1.35)$$

$a_j = \sqrt{\frac{\hbar}{m\omega_j}}$ is the linear spatial extention of the ground state wavefunction along cartesian direction j, while the mean width of the noncondensed atomic distribution is $a_{j_{thermal}} = \sqrt{\frac{k_B T}{m\omega_j^2}} = a_j\sqrt{\frac{k_B T}{m\omega_j}}$.

The atoms that are not condensed into the ground state can be treated semiclassically: one assumes a classical position-momentum distribution and a quantum Bose-Einstein statistics for their occupancy.

$$f(\vec{r}, \vec{p}, 0) = \frac{1}{e^{\left[\frac{p^2}{2mk_B T} + \frac{m}{k_B T}(\omega_x^2 x^2 + \omega_y^2 y^2 + \omega_z^2 z^2)\right] - \frac{\mu}{k_B T}} - 1} \qquad (1.36)$$

We conclude this section observing that, at early times ($\omega_j t << 1$), both the condensed and the excited spatial distributions are anisotropic, due to the anisotropic trapping potential, while, during further expansion, the atoms from the excited states form a spherically symmetric cloud, because of the isotropic momentum dependence of the $t = 0$ distribution function 1.36. By contrast, for the atoms that were condensed into the ground state, the direction that has the largest ω_j is quantum mechanically squeezed the most, at $t = 0$. So, according to the uncertainty principle, it expands the fastest.

1.3   The interacting Bose gas at T $=$ 0: *the Gross$-$* *Pitaevskii equation*

Let us now introduce interactions between particles and consider N interacting atoms, confined in an external magnetic trap potential, that can be approximated by an anisotropic harmonic oscillator potential of the form 1.25, as before.

In the second quantization formalism, the total Hamiltonian of the system is

$$\hat{H} = \int d^3\vec{r}\hat{\Psi}^\dagger(\vec{r})\Big[-\frac{\hbar^2}{2m}\nabla^2+V_{trap}\Big]\hat{\Psi}(\vec{r})+\frac{1}{2}\int d^3\vec{r}d^3\vec{r}'\,\hat{\Psi}^\dagger(\vec{r})\hat{\Psi}^\dagger(\vec{r}')[V_{int}(\vec{r}-\vec{r}')]\hat{\Psi}(\vec{r})\hat{\Psi}(\vec{r}')$$

(1.37)

The first term is a single-particle one, while the second is a two body term, representing atom-atom interactions.

$\hat{\Psi}^\dagger(\vec{r})$, $\hat{\Psi}(\vec{r})$ are bosonic field operators, acting in the Fock space

$F = \otimes_{n=1}^\infty H_n$, that create and destroy one particle at position $\vec{r}$, respectively. They can be expressed in terms of single-particle wavefunctions $u_n(\vec{r})$ as

$$\hat{\Psi}^\dagger(\vec{r}) = \sum_{n=1}^\infty a_n^\dagger u_n^*(\vec{r})$$

(1.38)

$$\hat{\Psi}(\vec{r}) = \sum_{n=1}^\infty a_n u_n(\vec{r})$$

(1.39)

The starting point for the theory we are going to develop is the time-dependent Schröedinger equation, written, in Heisenberg formalism, as:

$$[\hat{\Psi}(\vec{r},t), \hat{H}] = i\hbar\frac{\partial}{\partial t}\hat{\Psi}(\vec{r},t) = E\hat{\Psi}(\vec{r},t)$$

(1.40)

Here $\hat{H}$ is the Hamiltonian of the system and E its total energy.

Now we try to solve the problem of determining the temporal evolution of the system with a variational method. The destruction field operator $[\hat{\Psi}(\vec{r}, t)]$ can be decomposed into two terms:

$$\hat{\Psi}(\vec{r}, t) = \Psi_0(\vec{r}, t) + \delta\hat{\Psi}(\vec{r}, t) \qquad (1.41)$$

where $\delta\hat{\Psi}(\vec{r}, t)$ represents a small perturbation and $\Psi_0(\vec{r}, t) = \langle\Psi_0|\hat{\Psi}(\vec{r}, t)|\Psi_0\rangle$ is the ground state expectation value for the field operator $\hat{\Psi}(\vec{r}, t)$. We notice that, as the condensate fraction of the system is not invariant under $U(1)$, the number of condensed particles is not conserved and hence $\Psi_0(\vec{r}, t) \neq 0$. At low energies, a fairly accurate description is provided by approximating interactions by an effective contact potential:

$$V_{int}(\vec{r} - \vec{r'}) = u_0\delta(\vec{r} - \vec{r'}) \qquad (1.42)$$

where u_0 is the interaction constant. This is just the case for ultracold gases, since the kinetic energy and the density of the particles are small.

Approximating $\hat{\Psi}(\vec{r}, t)$ with its ground state mean value $\Psi_0(\vec{r}, t)$ and using assumption 1.42 in equation 1.40, gives the Gross-Pitaevskii equation (GPE)

$$i\hbar\frac{\partial}{\partial t}\Psi_0(\vec{r}, t) = \left[-\frac{\hbar^2\nabla^2}{2m} + V_{trap}(\vec{r}) + u_0|\Psi_0(\vec{r}, t)|^2\right]\Psi_0(\vec{r}, t) \qquad (1.43)$$

to which corresponds the Gross-Pitaevskii energy functional

$$E[\Psi_0] = \int d^3\vec{r}\left[\Psi_0^*(\vec{r}, t)\hat{H}\Psi_0(\vec{r}, t)\right] = \int d^3\vec{r}\left[\frac{\hbar^2}{2m}|\vec{\nabla}\Psi_0(\vec{r}, t)|^2 + V_{trap}(\vec{r})|\Psi_0(\vec{r}, t)|^2 + \frac{1}{2}u_0|\Psi_0(\vec{r}, t)|^4\right] \qquad (1.44)$$

This represents the mean field energy in terms of the macroscopic quantum state wavefunction $\Psi_0(\vec{r}, t)$, where $\Psi_0^*(\vec{r})\Psi_0(\vec{r}) = |\Psi_0(\vec{r}, t)|^2$ is the macroscopic ground-state number density $n_0(\vec{r})$.

We can now minimize the functional $E[\Psi]$ with respect to Ψ^*, taking into account the constraint that the total number of atoms in the system is constant

$$N = \int n(\vec{r})d^3\vec{r} = \int |\Psi(\vec{r})|^2 d^3\vec{r} \qquad (1.45)$$

By introducing the Lagrange multiplier μ (i.e. the chemical potential of the system) and setting $\delta E - \mu\delta N = 0$, the Gross-Pitaevskii equation takes the form:

$$\frac{\hbar^2}{2m}\nabla^2\Psi_0(\vec{r})^2 + V_{trap}(\vec{r})\Psi_0(\vec{r}, t) + u_0|\Psi_0(\vec{r})|^2\Psi(\vec{r}) = \mu\Psi(\vec{r}) \qquad (1.46)$$

This expression is quite appropriate for describing the zero-temperature nonuniform Bose gas when the range of the interaction between atoms is much smaller than the avarage interparticle spacing. We can notice that, when interactions are included, the equation describing the condensate is in the form of a single-particle Schröedinger equation with an additional non-linear term proportional to $u_0|\Psi(\vec{r})|^2$, that provides the mean field coupling of one particle to all the remainings.

In order to determine the mean field ground-state energy, one solves the Gross-Pitaevskii equation 1.46 for $\Psi(\vec{r})$ and uses the solution to evaluate the energy functional 1.44.

We are going now to analyze the various situations corresponding to the different kinds of interactions between particles. The coupling constant $u_0 = \frac{4\pi a \hbar^2}{m}$ depends on the scattering length a. If a is positive, the interaction is repulsive, while if a is negative the interaction is attractive. When $a = 0$, the solution of equation 1.46 is the noninteracting ground-state wavefunction $\Psi(\vec{r}) = \sqrt{N}\phi(\vec{r})$, while in the repulsive case ($a > 0$), if N is sufficiently large, the GPE can be analitically solved employing the Thomas-Fermi approximation. By contrast, in the case of attractive condensates ($a < 0$), only numerical and variational analysis are available.

1.4 Ground state of a repulsive condensate: *the Thomas − Fermi approximation*

The Thomas-Fermi regime is a useful assumption that allows to derive an expression for the system ground state wavefunction when the atomic clouds are sufficiently large. This statement is equivalent to the condition $\frac{N|a|}{a_{ho}} >> 1$, where the dimensionless parameter $\frac{N|a|}{a_{ho}}$ controls the strength of the interaction term ($a_{ho} = (a_x a_y a_z)^{\frac{1}{3}}$ represents the average linear size of the unperturbed harmonic oscillator ground state and $a > 0$ is the scattering length, that characterizes the interaction between atoms). If this situation is satisfied, the kinetic energy term $-\frac{\hbar^2\nabla^2}{2m}$ is much smaller than the interaction one, and the GPE can be written as:

$$[V_{trap}(\vec{r}) + u_0|\Psi(\vec{r})|^2]\Psi(\vec{r}) = \mu\Psi(\vec{r}) \qquad (1.47)$$

leading to the Thomas-Fermi solution:

$$\Psi_0(\vec{r}) \simeq \sqrt{\frac{(\mu - V_{trap}(\vec{r}))}{u_0}} \qquad (1.48)$$

that gives for the density of particles:

$$|\Psi_0(\vec{r})|^2 = n_{T-F} = (\mu - V_{trap}(\vec{r}))u_0^{-1} \qquad (1.49)$$

We notice that, as the solution must be positive, the boundary of the cloud is given by the condition:

$$V_{trap}(\vec{r}) = \mu \tag{1.50}$$

Hence, solution 1.49 is different from zero in the region defined by $\mu > V_{trap}(\vec{r})$, while $|\Psi_0(\vec{r})|^2 = 0$ otherwise. For a harmonic trap, the density distribution is an inverted parabola, whose maximum coincides with the potential minimum.

Taking into account the boundary condition 1.50 and the expression of the harmonic trap potential $V(\vec{r}) = \frac{1}{2}m(\omega_x^2 x^2 + \omega_y^2 y^2 + \omega_z^2 z^2)$, we can deduce an expression for the cloud extention along the three cartesian directions. It can be found that:

$$R_i = \sqrt{\frac{2\mu}{m\omega_i^2}} \tag{1.51}$$

with $i = x, y, z$. Besides, the normalization condition on $\Psi(\vec{r})$

$$\int d^3\vec{r}\, n_{T-F} = N \tag{1.52}$$

yelds the following relation between the chemical potential μ and the total number of bosons N

$$\mu = \frac{1}{2}\hbar\omega_{ho}\left(\frac{15Na}{a_{ho}}\right)^{\frac{2}{5}} \tag{1.53}$$

and finally, by combining 1.52 and 1.51, we obtain the spatial extention of the condensate in the Thomas-Fermi regime, expressed in terms of the harmonic trap characteristic length:

$$R_{T-F} = a_{ho}\left(\frac{15Na}{a_{ho}}\right)^{\frac{1}{5}} \tag{1.54}$$

Since $\mu = \frac{\partial E}{\partial N}$ and $\mu \propto N^{\frac{2}{5}}$, the total energy of the condensate in this limit is

$$E = \frac{5}{7}\mu N \tag{1.55}$$

The effect of repulsive interactions between bosons is therefore to expand the size of the condensate, making the anisotropy of the system and time-of flight distributions more anisotropic than in the noninteracting case. In fact, in time-of flight measurements, the repulsive interactions result in higher velocities in directions that were more confined in the trap.

The Thomas-Fermi length 1.54 indicates that the dependency of the condensate extention on the number of atoms N. This is a characteristic feature due to the introduction of interactions.

We are now going to make some observations concerning the attractive case. This situation corresponds to a negative scattering length $a < 0$. The presence of attractive forces between atoms makes the condensate to increase its density, thus reducing the extention, until equilibrium is reached through the balance between the compressing interaction term and the kinetic energy one, which, by contrast, tends to expand the condensate. Anyway, there exists a critical value for the number of atoms in the condensate, N_C, beyond which the kinetic pressure can't contrast the attractive interaction and the condensate collapses. However, in general, a long-lived atomic condensate exists for small negative values of the parameter $\frac{Na}{a_{ho}}$. This implies that the kinetic energy term in the Gross-Pitaevskii equation 1.46 can't be neglected with respect to the interaction term and the Thomas-Fermi approximation is no longer valid. Now, the system can't be treated analitically, but the study of its ground-state and the critical number N_C can be carried out through variational analyses of the Gross-Pitaevskii energy functional 1.44.

Chapter 2

A stable external-cavity diode laser to cool ^{87}Rb atoms

We will present here our laser setup, giving first an introduction about diode lasers and external-cavity diode lasers with an interference filter as wavelength selector. Then, we will report the details for the build up of the external cavity, the interference filter and the electronics and software developement for the feedback system that controls the wavelength stability. Eventually, we will compare the results that we obtained with and without the external cavity, in order to demonstrate the advantages given by this latter configuration.

2.1 Introduction

Dealing with atomic physics experiments, the basic requirement is to have an interaction between atoms and coherent light. Diode lasers were used for the first time in this field of physics in the early 80's and, since that moment, their performances were rapidly improved and there has been a great deal of research about these systems. The main characteristics that have made diode lasers so important are their high reliability and tunability, but also the fact that they are inexpensive sources of light, so that every laboratory can afford them. The first employed diode lasers were simple free running devices, without feedback, mainly used for low resolution spectroscopy. Nevertheless, since the 90's, they have been steadily improved in power as well as in wavelength coverage, while decreasing costs. Feedback systems were also developed, allowing narrower linewidths (of the order of few hundreds kHz) and more stable amplitudes and frequencies.

The wavelength control techniques have made possible advanced applications for standard commercial diode lasers in atomic physics and we are now going to examine the mainly ones. Optical pumping consists of cyclically pump electrons, bound within an atom or molecule, to a defined quantum

state. Considering an alkaline atom, for which only one electron belongs to the outermost shell, a coherent two level optical pumping means that the electron is coherently pumped to a single hyperfine sublevel and the atom is said to be oriented in that particular sublevel. The optical pumping has a cyclic nature, so that the electron experiences repeated transitions between upper and lower state sublevels and the orientation of the atom is determined by the polarization and frequency of the laser light, as well as the linewidth and transition probability of the absorbing transition.

Diode lasers are also employed in applications using fast frequency modulation, because it is particularly easy to modulate their amplitude and frequency very fast (the modulation response for common diode lasers extends out to a few GHz) and through large ranges. This can be achieved modulating the injection current of the diode laser, which produces both amplitude (AM) and frequency (FM) modulation. The injection current modulation spreads out the diode laser's spectrum into many discrete sidebands and this effect increases with the strength of the modulation. The modulation sidebands method finds many applications, as it allows to increase the signal-to-noise ratio and thus to detect atomic or molecular resonances with high sensitivity. For molecular species spectroscopy, also, "two-tone" modulation methods (modulations at two different frequencies) were developed and the modulation into sidebands is generally useful in atomic and molecular physics experiments were numerous frequencies are required. Furthermore, diode lasers have the unique capability to sweep the laser frequency extremely rapidly in a controlled manner, by an high speed switching, or pulse. This jumping of the output frequency permits to reduce the number of lasers needed in optical pumping experiments; indeed, for example, it is possible to optical pump some kind of alkaline atoms into a specific magnetic sublevel using only one single laser [4]. The frequency modulation capability is also succesfully used to slow down and stop atomic beams, as well as to rapidly probe atomic velocity distributions. Their performances are limited by the broadness of the laser linewidth, but they can be seriously improved by an external cavity that stabilizes the laser and narrows its linewidth, with a resulting increase in the number of slowed atoms and a decrease in the spread of the velocity distribution. As mentioned above, feedback-stabilized diode lasers are unique, in that thay provide simple and inexpensive sources of narrowband tunable and stable amplitude light, which involves very good signal-to-noise ratios and make them suitable for high resolution spectroscopy. In fact, with this high precision measurement systems, atomic transition spectra can be detected, with spectral linewidths only limited by the natural linewidth of the transition and not by that of the laser (which can be lower than 100 kHz).

For us, the most important area concerning stabilized diode lasers is laser cooling and trapping of neutral atoms. As a matter of fact these experiments require several lasers working at different frequencies with linewidths of less

than 1 MHz. For these reasons diode lasers provide an important resource in order to limit the cost of setups that would be otherwise really expensive, and external cavity or grating stabilized diode lasers make it possible to have radiation with linewidths under 100 kHz. Once again, considering alkaline atoms, optical molasses have been created containing 10^7-10^8 atoms or more, cooled to temperatures of about 100 μK [4]. Trapping times greater than 100 s have been attained and hence it was possible to study various kinds of interactions between the trapped atoms. A note is needed to point out that only few hundreds mW are usually achieved with diode lasers alone, and this power can decrease to 30 mW or less after feedback reflection and wavelength selection. In general it is possible to overcome this shortcoming by techniques like "self-locking buildup cavities" or injection-locked diode lasers, which make possible to recover more than 50 mW output power[4].

This chapter is aimed to the purpose of describing a detailed treatment concerning the realization of a diode laser with an external cavity that provides feedback reflection and a low loss interference filter used as wavelength selector (a diffraction grating was instead usually used for this two tasks). The scheme assures independent ways for wavelength selection and feedback control, that can be thus optimized separately. This involves a drastically improved stability with respect to environment perturbations, such as mechanical or thermal deformations, as well as an increased laser tunability. Section two will be focused on the basic characteristics and main general aspects of diode lasers, while in section three we will report a detailed description of our system, including the specific optical and mechanical setup of the external cavity, as well as the electronic and software development for the feedback control. Finally, we will report our results and future applications for interference-filter-stabilized external-cavity diode lasers.

2.2   General features concerning interference-filter-stabilized diode lasers

As already mentioned, interference-filter-stabilized external-cavity diode lasers are suitable devices for single mode operations that requires narrow linewidth and good tunability. The external cavity is provided by the high reflectivity coated back facet of the diode and a partially reflecting mirror (out-coupler) with 70% transmission. The mirror provides the feedback reflection, that can be optimized changing its reflectivity, while narrow-band dielectric interference filter, placed between the diode and the out-coupler, acts as an intra-cavity wavelength selector. This system represents an improvement with respect to the previous diffraction grating external-cavity diode lasers. Indeed, separation of the two tasks of wavelength selection and feedback reflection allows them to be optimized independently [6]. Hence, tunability over a broader wavelength range can be demonstrated. Compared to the Littrow configuration, the "cat's eye" scheme that we used, shown in (fig.2.1), reduces the sensitivity of the laser to environmental perturbations and provides much better stability against optical misalignment.
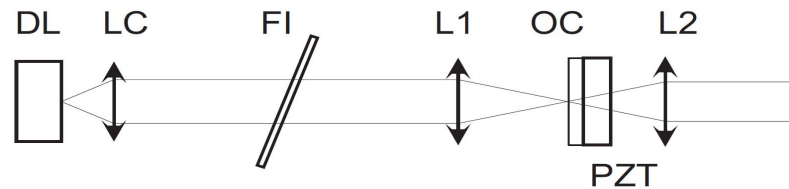
Figure 2.1: The "cat's eye" scheme

For a grating-stabilized diode laser, the linewidth decreases with the square of the external cavity length [5], but a long external resonator, with the grating far from the diode, can cause instabilities and multi-mode operations. Furthermore, for the common Littrow configuration, the direction or position of the output beam depends on the wavelength selection, i.e. on the angle between the beam and the grating. Thus, longer external resonators

cause greater laser beam displacements when the wavelength is changed. A good compromise for the length of the cavity for a grating-stabilized laser leads to a linewidth of typically a few hundred kHz. On the other hand, interference filters provide linewidths less than 100 kHz. Thanks to their narrow bandwidth, outputs filters efficiently suppress chaotic coupling to adjacent diode modes, that may occur because the laser chip itself constitutes a second cavity (due to the fact that some light is reflected on the diode's output facet).

Going into a more detailed description, for a Littrow configuration, the wavelength discrimination is given by the Bragg condition $\lambda = 2dsin\theta$, where d is the grating's line spacing and θ is the angle of incidence. Assuming typical values for d and θ ($d^{-1} = 1200$ lines/mm and $\theta = 30°$), it is possible to evaluate a transverse displacement of the beam, while changing the wavelength, equal to $\frac{dx}{d\lambda} = 18$ μm/nm, at a distance of 15 mm from the grating [6]. The corresponding angular dependence of the wavelength is $\frac{d\lambda}{d\theta} = 1.4$ nm/mrad. Turning now to interference filters, the transmitted wavelength is given by [6]:

$$\lambda = \lambda_\perp \sqrt{1 - \frac{sin^2\theta}{n_{eff}^2}} \qquad (2.1)$$

where $\lambda_\perp$ is the transmitted wavelength at normal incidence and n_{eff} is the effective index of refraction for the filter (a tipical value is $n_{eff} = 2$). Taking $\theta = 6°$ and $\lambda_\perp = 853$ nm, leads to $|\frac{d\lambda}{d\theta}| = 23$ pm/mrad, which is about 60 times smaller than for the Littrow configuration and demonstrates a substantial reduction of the wavelength sensitivity against mechanical instabilities. Finally, it is possible to demonstrate that the transverse displacement of the beam, consequently to the light tuning, is about two times smaller than for the previous configuration.

2.3 Our external cavity setup

2.3.1 Assembly of the mechanical components

Figure2.1 shows a scheme of the external cavity optical configuration: the light emitted from the diode (DL) is collimated by a first lens (LC) with a short focal length of 3.1 mm. Then the collimated beam is focussed onto a partially reflecting mirror (OC) in a "cat's eye" configuration, formed by two lenses L1 and L2, of focal lengths 18.4 mm and 11.0 mm, respectively. The second lens provides a collimated output beam. The mirror is called here out-coupler and, thanks to the 30% reflective coating, provides the feedback into the diode. A piezo-electric transducer (PZT) attached to the mirror, allows to displace it in order to vary the length of the cavity. The optical

element called FI is the narrow-band interference filter mentioned above, that gives the frequency selectivity.
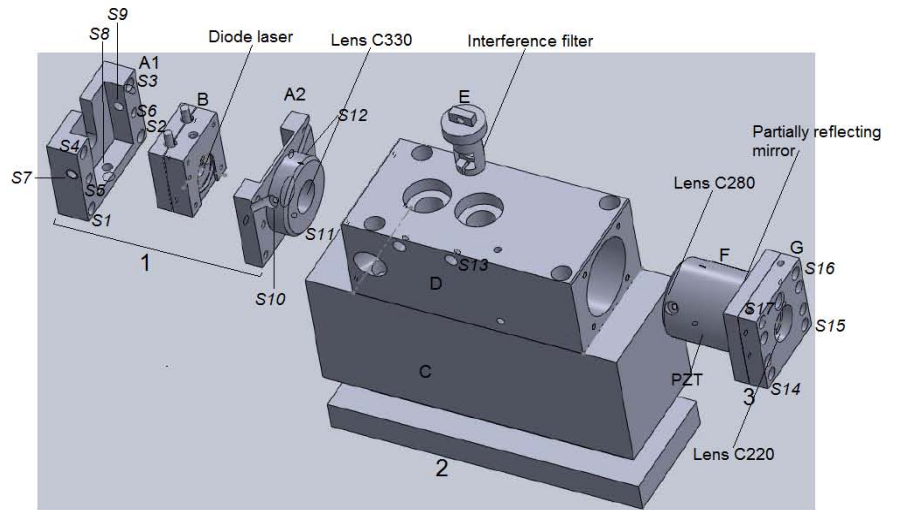

Figure 2.2: External cavity setup

Figure2.2 and 2.3 represent the various mechanical parts that constitute the external cavity setup. They are split up in three main assemblies labelled (1), (2) and (3). Part (1) is made up by two distinct sections, called (*A*) and (*B*) in the drawing. Figure2.3 gives an insight of part (1), and shows the various elements that compose it: our diode laser ($Thorlabs - L785P090$) is set inside the copper disk (*B*4), directly in contact with a Peltier (*B*3) that ensures its termal stability. One first holder, made up by the two parts called
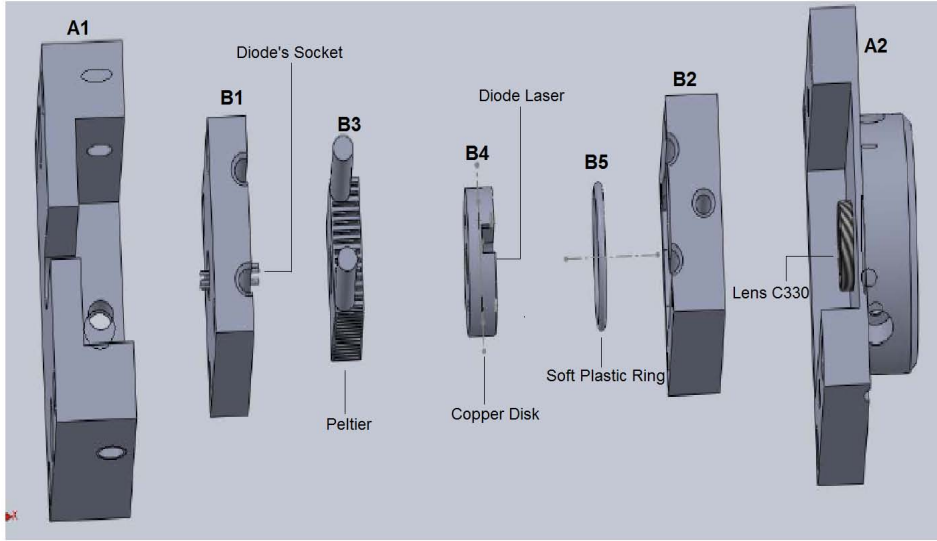
Figure 2.3: Insight of part 1

($B1$) and ($B2$), keeps the diode and the Peltier together and a soft plastic ring ($B5$) ensures a good mechanical contact between the copper disk and ($B2$). Part (B) is locked between ($A1$) and ($A2$), thanks to the two screws ($S5$) and ($S6$) and part (1), as a whole, is fixed to part (2) by means of four screws placed at the edges of holder (A) and labelled ($S1$), ($S2$), ($S3$), ($S4$) in the figure. Finally, lens $C330$, that provides a first collimation for the light emitted from the diode, is placed inside the very right cylindrical edge of part ($A2$) and its position can be fixed by the three screws that we called ($S10$), ($S11$) and ($S12$).

Section (2) consists of three parts: (C) is a solid aluminum base, (D) forms the body of the external cavity, with two holes at its ends in which parts (1) and (3) will be positioned to form the external cavity and (E) is an aluminum holder for the interference filter. Part (E) can be rotated, so that the angle formed with the incident beam can be changed in order to select the right wavelength for the output beam. Its position can be fixed

through screw ($S13$).

Finally, part (3) contains the"cat's eye" scheme. The first lens ($C280$) focusses the beam on the partially reflecting mirror and both are set into part (F), while part (G) holds the second lens $L2$, that provides a collimated output beam. Part (3) can be fixed to part (2) through four screws, labelled ($S14$), ($S15$), ($S16$), and ($S17$). As far as the optical alignment of the system is concerned, the diode's holder (B) was carefully positioned inside part (A) and we tried to make it as stable as possible, because even small perturbations in its position could cause a cutting in the shape of the laser beam, when the three main parts were put together.

2.3.2   The aligning procedure

A first collimation was provided by taking part (1) out from the cavity and choosing the right distance for lens ($C330$). Because the beam shape strongly depends on the position of section (B) inside holder (A), after a first rough choice for the position of (B) (good enough to ensure a non cut shape of the beam), we slightly tightened screws ($S5$), ($S6$) and then we did the last fine adjustment by little displacements of part (B) inside part (A), thanks to the three screws ($S7$), ($S8$) and ($S9$). The next step was to align the "cat's eye" scheme, with part (3) out from the cavity. We took as reference the beam just collimated by lens ($C330$) and, using the scheme shown in fig.2.4, we displaced lens ($C280$) in order to collimate the part of the beam reflected by the out-coupler. Eventually, the whole external cavity was built, and we optimized the collimation of the transmitted part, by means of lens ($C220$).

The beam axis out of the diode is defined by the metallic holder (B). We used screws ($S7$), ($S8$), ($S9$) and ($S10$), ($S11$), ($S12$) (that lock lens ($C330$)) for the vertical and horizontal alignment of the beam out of the diode holder (A). The first was performed measuring the heigth of the beam at different distances and we could obtain a vertical displacement of less than 1 mm over about 45 cm distance. If we consider that the cavity length is about 8 cm, it is possible to see a vertical misalignment lower than 0.2 mm between the two points at which light is emitted from the diode and reflected by the mirror. Assuming a good orientation of the mirror (i.e. such that the beam displacement after reflection is slightly affected by the mirror orientation), this implies a displacement lower than 0.4 mm at the diode position, after reflection, and this is sufficient in order to have a good overlap between the diode output and reflected beams for injecting the diode's active area. For the horizontal alignment we used the filter holder (E) (without the filter in) and we checked that the beam was symmetrically cut at both sides, when part (E) was rotated. As a consequence we could achieve a lower threshold current for the lasing effect to occur, from 31 mA without the cavity to 27 mA, when the external cavity was in.
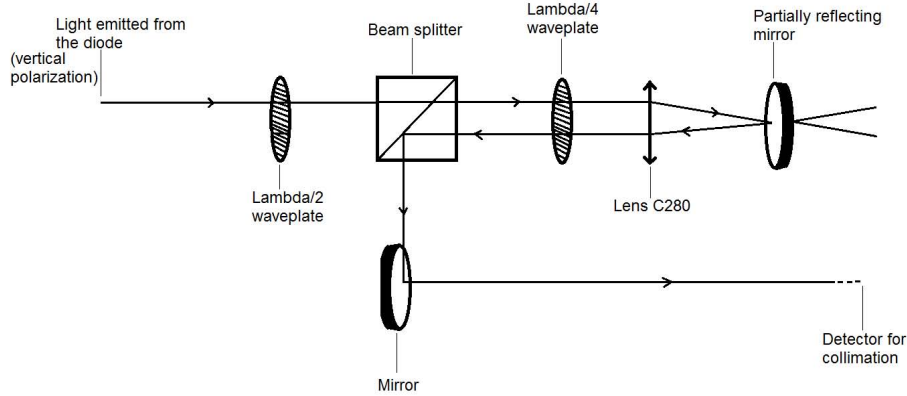
Figure 2.4: Scheme of the design we used to align the "cat's eye".

The interference filter is a bandpass filter, formed by a series of dielectric coatings on an optical substrate with anti-reflection coated back face. In order to reduce the production costs, optical filters are usually fabricated from larger wafers and then cut into pieces. The filter we choose belongs to a sample of 25 filters with different bandpass wavelengths. They are 1 mm thick and have a surface area of 6×6 mm^2. We made use of a filter having 780.3 nm as nominal wavelength at normal incidence with respect to its surface. Figure2.5 shows the filter transmission curve given by the company datasheet, for a filter transmitting at about 780 nm. The curve refers to an incident beam forming an angle of zero degrees with respect to a unitary vector normal to the surface of the filter. The angle of maximum transmission depends on the wavelength and width of the transmission curve (specified at 0° incidence angle). The fullwidth at half maximum (FWHM) of the curve is about 0.12 nm and this is a good compromise in order to provide sufficient discrimination for stable single mode lasing with satisfactory

output power. Indeed, higher finesse can be achieved at the cost of reduced transmission.
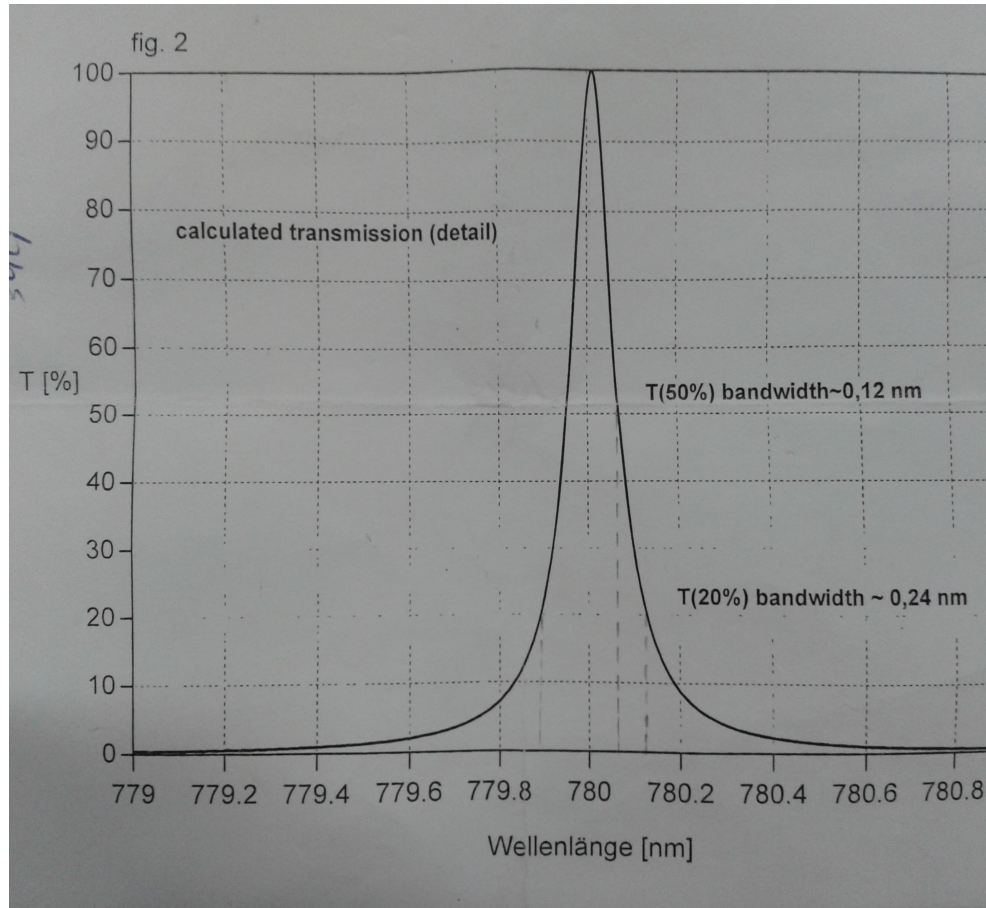

Figure 2.5: Typical transmission curve for a filter transmitting at 780 nm.

Figure 2.6 describes the angular dependence of the spectral shift to shorter wavelengths for a typical interference filter in our sample. We will describe how interference filters act on wavelength stability in section 2.5.
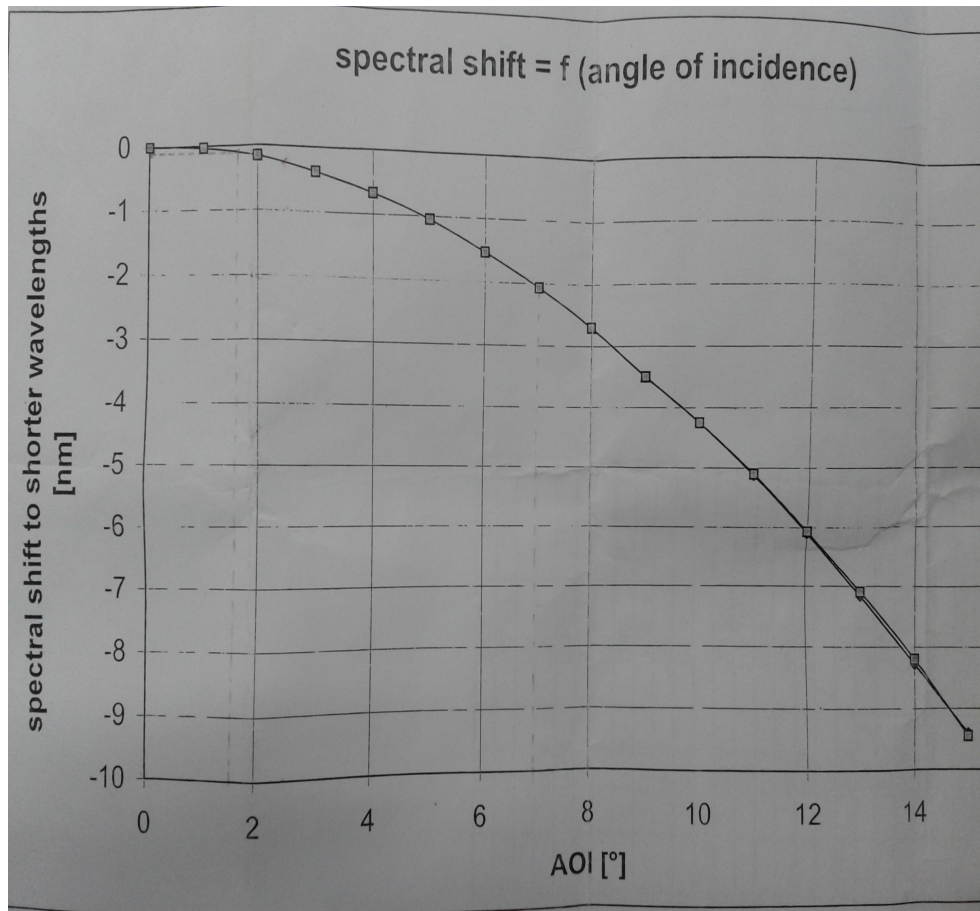
Figure 2.6: Filter spectral shift with respect to the incident angle of the beam.

2.4 The feedback system: temperature and wavelength stability controls

2.4.1 Sensitivity of the optical feedback for an interference-filter-stabilized external-cavity diode laser

With optical feedback is meant the amount of light that can reach the active area of the diode after reflection on the partially reflecting mirror that forms one end of the external cavity. The optical feedback can be affected by a misalignment of the external cavity with respect to the beam direction. If we consider a gaussian beam propagating through the cavity, whose direction is defined by the cartesian axis z, we can define as E_0 and E_{2L} the electric fields at the position of the output facet of the diode after emission ($z = 0$) and after reflection on the out-coupler ($z = 2L$), respectively (where L is

the cavity length). The overlap integral of the emitted and reflected electric fields is a quantity that describes the feedback [6]

$$F = R^{-1} \Big| \int \int E_0^*(z=0)E(z=2L)dxdy \Big|^2 \tag{2.2}$$

where the reflectivity of the out-coupler R is a normalization factor. Therefore, the computation of the variation of F quantifies the mechanical and thermal sensitivity of the laser to a misalignment of the external cavity. The integral can be simplified if we evaluate it at the position of the out-coupler ($z = L$):

$$F = R^{-1} \Big| \int \int E_i^*(z=L)E_r(z=L)dxdy \Big|^2 \tag{2.3}$$

where E_i is the electric field corresponding to the incident beam, while E_r is that of the reflected one. This simplification is possible because it turns out that F is independent on the number of lenses inside the cavity [6]. Moreover, every displacement of optical elements can be transformed into two kinds of misalignment sources: tilt or axial displacement of the out-coupler. It turns out that, in the first case, for a small tilt angle [6]:

$$F = e^{-(\frac{\alpha \pi w_0}{\lambda})^2} \tag{2.4}$$

while, if the reflective element is displaced along the optical axis:

$$F = \Big[1 + \Big(\frac{\delta \lambda}{\pi w_0 2}\Big)^2\Big]^{-1} \tag{2.5}$$

Here α and δ are respectively the angle formed by the incident and reflected beam and the displacement of the mirror along the optical axis. w_0 is the waist of the incident beam at the out-coupler position, assuming normal incidence. If we now approximate the series expansion for the variation of F to the second order term:

$$dF = F\Big|_{\alpha=0} + \alpha\Big(\frac{\partial F}{\partial \alpha}\Big)\Big|_{\alpha=0} + \frac{1}{2}\alpha^2\Big(\frac{\partial^2 F}{\partial \alpha^2}\Big)\Big|_{\alpha=0} + O(\alpha^3) \tag{2.6}$$

and a similar expression for the feedback function with respect to the variable δ, it is possible to observe that the first order terms equal zero, while for the second order ones we have:

$$\Big(\frac{\partial^2 F}{\partial \alpha^2}\Big)\Big|_{\alpha=0} = -\frac{2\pi^2 w_0^2}{\lambda^2} \tag{2.7}$$

$$\Big(\frac{\partial^2 F}{\partial \delta^2}\Big)\Big|_{\delta=0} = -\frac{2\lambda^2}{\pi^2 w_0^4} \tag{2.8}$$

These expressions show that w_0 is the only parameter which determines the sensitivity of the optical feedback to misalignment. Values of a few

μm for the waist are typical for a system in which wavelength selection and optical feedback are independent tasks (like in our system in which the first function is fulfilled by an interfernce filter, while the second by a partially reflecting mirror) and this guarantee that only large deformations in both parameters α and δ (of the order of some mrad and tenths of mm, respectively) can decrease the factor F by 10%. On the other hand, a grating-tuned extended cavity laser (in which the previous two operations are carried out by the same diffraction grating), is characterized by much greater values for w_0, typically of 1 mm magnitude. This makes the system much more sensitive to external perturbations, and even a tilt of the grating of few hundreds μrad is sufficient to reduce F by a 10% factor [6].

The above analysis points out the advantages given by our "cat's eye" scheme, as far as the optical feedback is concerned. We will turn now to the electronic device we used for the temperature stability and wavelength control. The diode's current supply was housed in a metallic box, assembled by Alessio Montori at LENS electronic whorkshop. This electronic system can be divided into three main parts: the diode's current supply, the temperature controller and the driver for the piezo-electric transducer.

2.4.2 Description of the electronic system control

Figure2.7 is a scheme of the connections between the laser system (diode and external cavity), the metallic box containing the electronic components for the power supply and the electronic device that we used for the feedback system, while in fig.2.8 a front view of the metallic box, shows the three main parts mentioned above. On the left side we have the diode's current supply the diode, and the output signal (BNC 1) is controlled by means of a potentiometer (Pot 1). Its value is monitored on the display and ($Switch$ 1) commutes between current or voltage monitoring. The current is shown in mA units (and the corresponding voltage in mV), with a resolution of 1 mA and a maximum value of about 200 mA. The middle part is devoted to the temperature feedback: (BNC 2) and (BNC 3) provide input voltage signals, representing the temperature of the external cavity and the diode, respectively. For each temperature stabilization unit, the temperature is converted into a voltage signal by means of a temperature-dependent resistor (thermistor) in a simple voltage divider formed by the thermistor and a stable $10k\Omega$ resistor. The signal, once processed, is then converted into the output current feeding the Peltier cell. The connectors of output currents are labelled as (TEC1) and (TEC2) in figure2.8. The right part is for the piezo-electric tranducer (PZT) control. The voltage delivered to PZT through (BNC 5) is the sum of three contributions: an offset voltage (controlled by means of (Pot 4)), a triangular, square or sinusoidal ramp, and a third one (correction signal) that can be added to the other two through (BNC 4) and whose function is to give the difference with respect to a reference
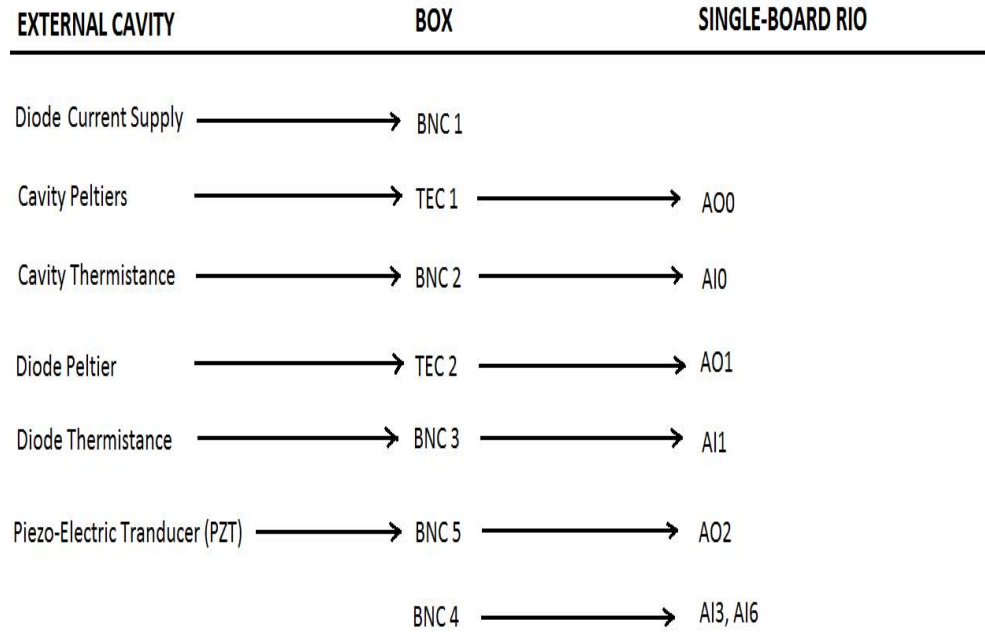
Figure 2.7: Scheme of the connections between the laser system components, the metallic box (whose front face is shown in fig.2.8) and the electronic device we used for the feedback system (fig.2.9). The "Diode Current Supply" is amplified inside the box without being processed by the $sbRIO - 9636$ (refer to fig.2.9), while the box input channel named $BNC4$ is needed for providing a signal to the $sbRIO - 9636$ device for the PZT control and thus it is not connected to the laser system.

value; the electronic system for the PZT feedback will act in a way to make the error signal (i.e. the difference between the actual and reference signals before they are processed by a controller) equal to zero. While the offset is always present, the other two can be switched on or off using ($Switch$ 2) for the ramp and ($Switch$ 3) for the correction signal. Finally, (Pot 2) and (Pot 3) allow to change the ramp frequency and amplitude, respectively.

The electronic device that we used for the feedback was provided by National Instruments company and consists of two boards: a Single Board RIO ($NI\ sbRIO-9636$) and a National Instruments RIO Evaluation device.

The lower board is the sbRIO device, whose components are shown in figure 2.10.

The sbRIO is featured by a 512 MB nonvolatile memory and a 256 MB system memory (RAM). It can be supplied with a maximum DC voltage
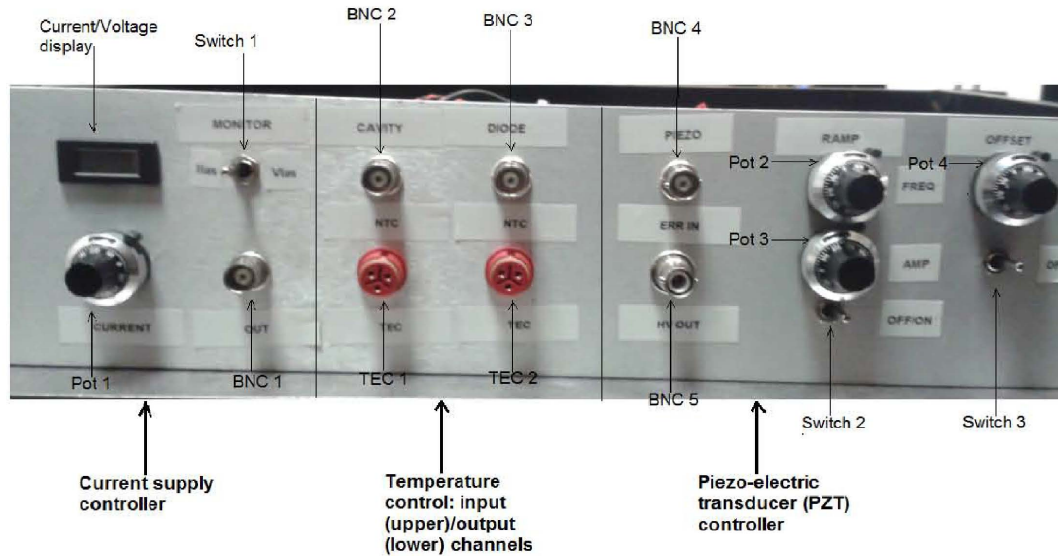
Figure 2.8: Front view of the box containing the electronic circuit we used for the diode current supply, the temperature controller and the PZT driver.

of 30 V through the power connector (4), provides a number of digital and analog inputs/outputs and has an internal function generator, supplied with a battery that gives a maximum signal of 3.7 V. Component (8) is a ethernet port through whitch it is possible to interface the board to a Windows OS processor. The upper board is the NI RIO Evaluation device and it is connected to the $sbRIO - 9636$. The connectors $J502$ and $J503$ (numbers (12) and (13) in figure 2.10), provide the pinout for all digital and analog inputs/outputs (I/O) on the Single-Board RIO and they are reproduced on
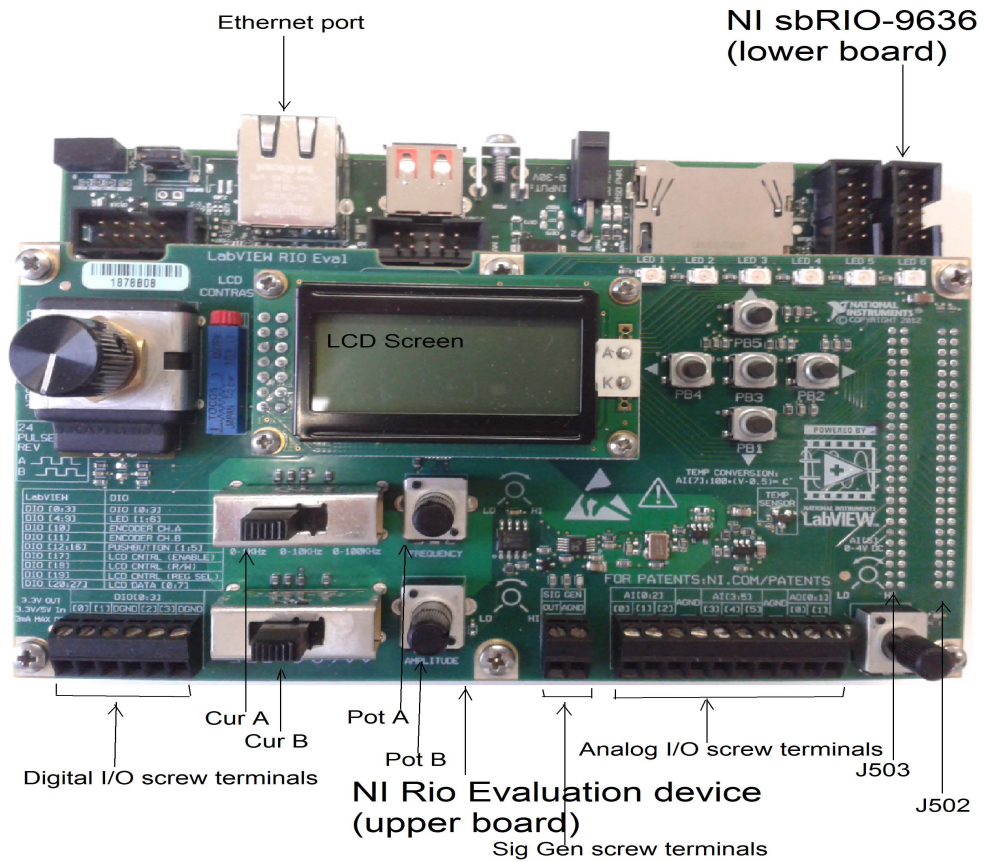
Figure 2.9: Picture of the electronic device for the feedback system: the lower board is the $NI\ sbRIO - 9636$, while the upper board is the NI RIO Evaluation device and is connected to the first one.

the upper board. The device has 16 multiplexed, ± 10 V range, single-ended analog input channels, with 16-bit resolution and four analog output channels with the same characteristics. Connector $J503$ provides analog inputs, outputs and grounds. On the other hand, connector $J502$ provides the 28 digital I/O. Some component offered by the NI RIO Evaluation board are the six screw terminals for digital I/O [0:3] and two corresponding grounds, as well as six analog inputs ([0:5] plus one ground) and two analog outputs ([0:1] plus ground) screw terminals, as indicated in figure 2.9. Furthermore, the two potentiometers referred to as $(Pot\ A)$ and $(Pot\ B)$ in figure 2.9, allow a direct by hand access to the frequency and amplitude of the signal given by the embedded wave function generator. The two cursors $(Cur\ A)$, $(Cur\ B)$ allow to choose between three options for the frequency $(0 - 1$ Hz; $0 - 10$ Hz; $0 - 100$ Hz) and shape (square, sinusoidal or triangular) of the

2.4. *THE FEEDBACK SYSTEM*

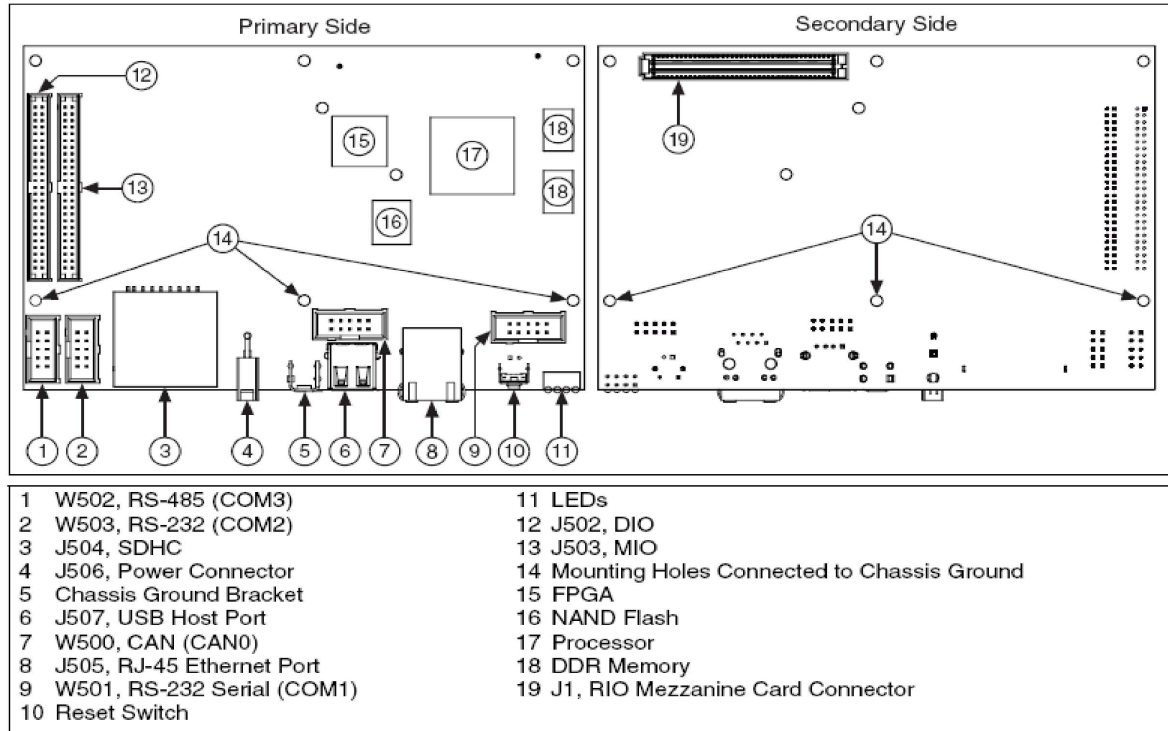

Figure 2.10: All possible components on the NI sbRIO Device.

signal. The last set of screw terminals (*Sig Gen screw terminals*) is for the output of the incorporated signal generator.

The two most important components of $NIsbRIO - 9636$ are the FPGA target (Spartan-6 LX25 type, distributed by Xilinx company) and the 400 MHz processor, labelled (15) and (17) in figure 2.10, respectively. A FPGA (Field Programmable Gate Array) is a chip with software programmable functionalities. It is made up by configurable logic blocks (CLB), that realize logic functions thanks to programmable interconnections between them, and input/output blocks (IOB) for data communication. With the Lab-

VIEW programmable FPGA target it is for example possible to realize logic functions for analog and digital I/O configurations, as well as realize operations concerning the LEDs and push buttons annexed to the NI RIO Evaluation device. On the other hand, the processor implements real-time operations and, establishing a communication channel with the FPGA, it is for instance possible to configure the LCD screen of the NI RIO Evaluation device for real-time monitoring applications. In the following we will describe how, exploiting the FPGA, I have implemented the real-time tasks required for the diode's temperature stability and piezo-electric transducer control.

2.4.3   The temperature control system: the Peltier

The physical components used for keeping the temperature stability of the external cavity and the diode are two Peltier elements with 6.0 A as maximum supply current. One is set between elements (C) and (D) of part (2) in fig.2.2, while the other is located inside the holder (B) of part (1) (it is called $(B3)$ in fig.2.3).

In order to present a short description of the Peltier effect we can consider an apparatus at constant uniform temperature, composed by two different metallic wires A and B that meet at two A/B junctions to form a closed circuit, and a battery that drives current around it. We can threat the system using a linear irreversible thermodynamic approximation, in terms of conjugate forces and fluxes and the related coefficients. According to the constraints imposed on the system, only heat and electrical charge currents will be present, and to first order approximation:

$$J_Q = \frac{\partial J_Q}{\partial F_Q} F_Q + \frac{\partial J_Q}{\partial F_q} F_q \qquad (2.9)$$

$$J_q = \frac{\partial J_q}{\partial F_Q} F_Q + \frac{\partial J_q}{\partial F_q} F_q \qquad (2.10)$$

Here J_Q and J_q are the heat and charge current fluxes, while the corresponding driving forces are:

$$F_Q = -\frac{1}{T}\frac{dT}{dx} \qquad (2.11)$$

and

$$F_q = -\frac{d\phi}{dx} \qquad (2.12)$$

where ϕ is the electrical potential and x measures the distance along the wires. In these relations the vector symbol for the physical quantities involved has been omitted, as we are considering all forces and fluxes to be parallel to each other. If we now define the direct and coupling coefficients

$L_{QQ} \equiv \frac{\partial J_Q}{\partial F_Q}$, $L_{qq} \equiv \frac{\partial J_q}{\partial F_q}$ and $L_{Qq} \equiv \frac{\partial J_Q}{\partial F_q}$, $L_{qQ} \equiv \frac{\partial J_q}{\partial F_Q}$, and take into account the boundary condition that the system is at constant temperature (which implies $\frac{dT}{dx} = 0$), we find a relation between the heat and charge currents, which is proportional to the ratio of the coupling (L_{Qq}) and direct (L_{qq}) coefficients:

$$J_Q = \frac{L_{Qq}}{L_{qq}} J_q \qquad (2.13)$$

As these coefficients will have different values for the two metals A and B, therefore heat will accumulate and be emitted at one junction, while it will be absorbed at the other[8]. Thus, exploiting the Peltier effect, it is possible to build up a feedback system for temperature stability.

2.4.4 Temperature control system: the LabVIEW project

We briefly introduced the basic principle behind the implementation of logic functions on a FPGA chip. Here we are going to describe the details for the developement of the FPGA and Real-Time applications for our temperature stabilizing system. $NIsbRIO - 9636$ is a LabVIEW software programmable device, and we used LabVIEW 2012 version to develop our program. Figure 2.11 shows a sequence of three sketches of the LabVIEW Project Explorer Window, in which different targets are progressively expanded.

Let us look for the moment to the first sketch, placed to the left: we can observe a three level hierarchy, in which each level is indicated by a vertical line connecting two or more targets. The highest level refers to the Windows OS processor and to the Single-Board RIO device, which are connected through the ethernet port communication channel. The second level of the hierarchy corresponds to the target named "$Chassis(sbRIO-9636)$". It represents the Real-Time microprocessor (Component (17) in fig.2.10) and every real-time application will run under this target. The third and last level represents the FPGA and under the target "$FPGATarget(RIO0, sbRIO - 9636)$" it is possible to find all physical components belonging to the single-board RIO device and connected to the FPGA chip (component (15) in fig.2.10). Finally, the targets we named as "$Real\_Time\_Microprocessor\_20131125.vi$" and "$Display\_temp\_setpoint\_plus\_buttons\_20131125.vi$", placed under the Real-Time and FPGA targets, respectively, are the two virtual instruments that we programmed on LabVIEW from the Windows OS interface. A virtual instruments represents an application capable to implement logic functionalities on the Single-Board RIO electronic device, as we could see later.

The purpose of our LabVIEW project is to develop a FPGA application for the configuration of analog inputs and outputs, in order to built a feedback system capable to stabilize the external cavity and diode temperatures: we used two 10 $k\Omega$ thermistors that, depending on the cavity and
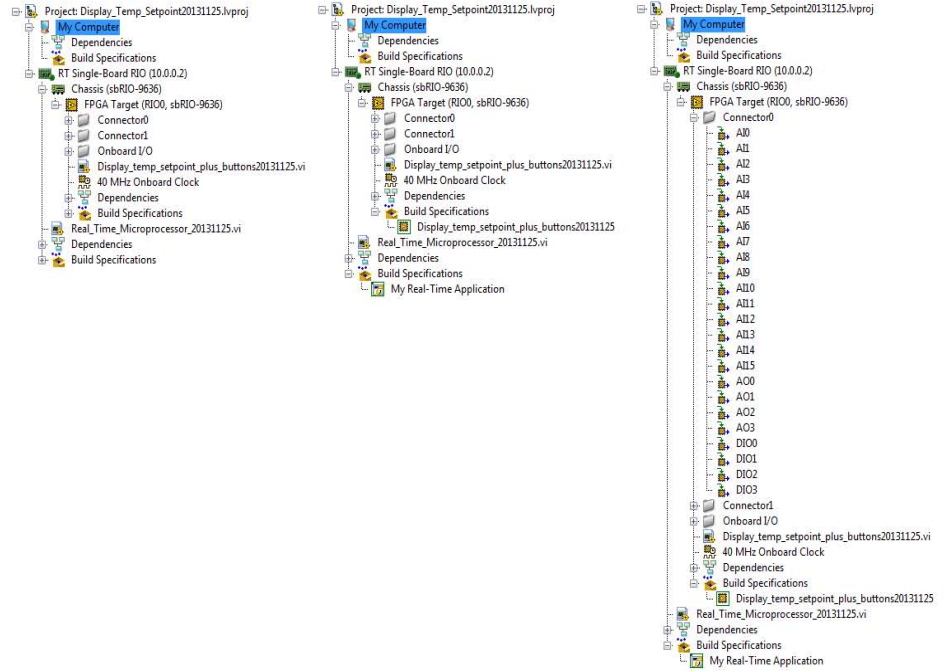
Figure 2.11: LabVIEW Project Explorer Window: three sketches of the same project are displayed, in which different targets are progressively expanded.

diode temperatures, provide an input voltage signal to the Single-Board RIO. The device then acts to make this signal equal to a certain setpoint value, that fixes the final temperature for the system. The second task of the project is to implement a Real-Time application, to display the current setpoint values for both cavity and diode temperatures, as well as to moni-

tor their real time temperatures. Finally, for making this tasks independent from the Windows OS interface, we built a FPGA and a Real-Time standalone applications, that allow the FPGA and Real-Time virtual instruments to run automatically on the Single-Board RIO device.

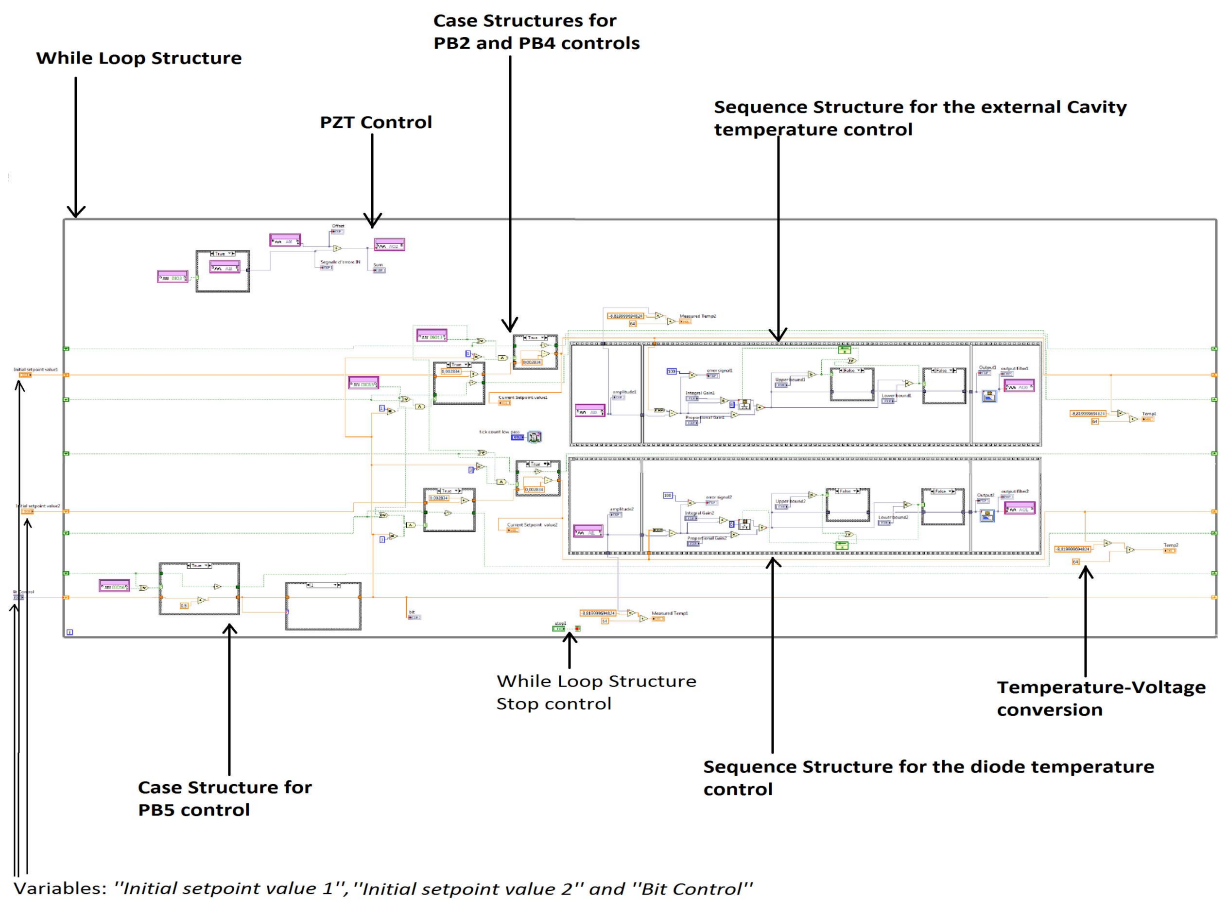*The FPGA Virtual Instrument*

Figure 2.12: FPGA VI Block Diagram.

We will now examine the LabVIEW program concerning the FPGA Virtual Instrument (FPGA VI). Thanks to the Windows OS interface, a virtual instrument can be viewed into two different ways: through the VI Block Diagram, that shows the LabVIEW functions that realize the logic blocks, or through the VI Front Panel, that provides a direct view of the values of the variables that belong to the VI Block Biagram.
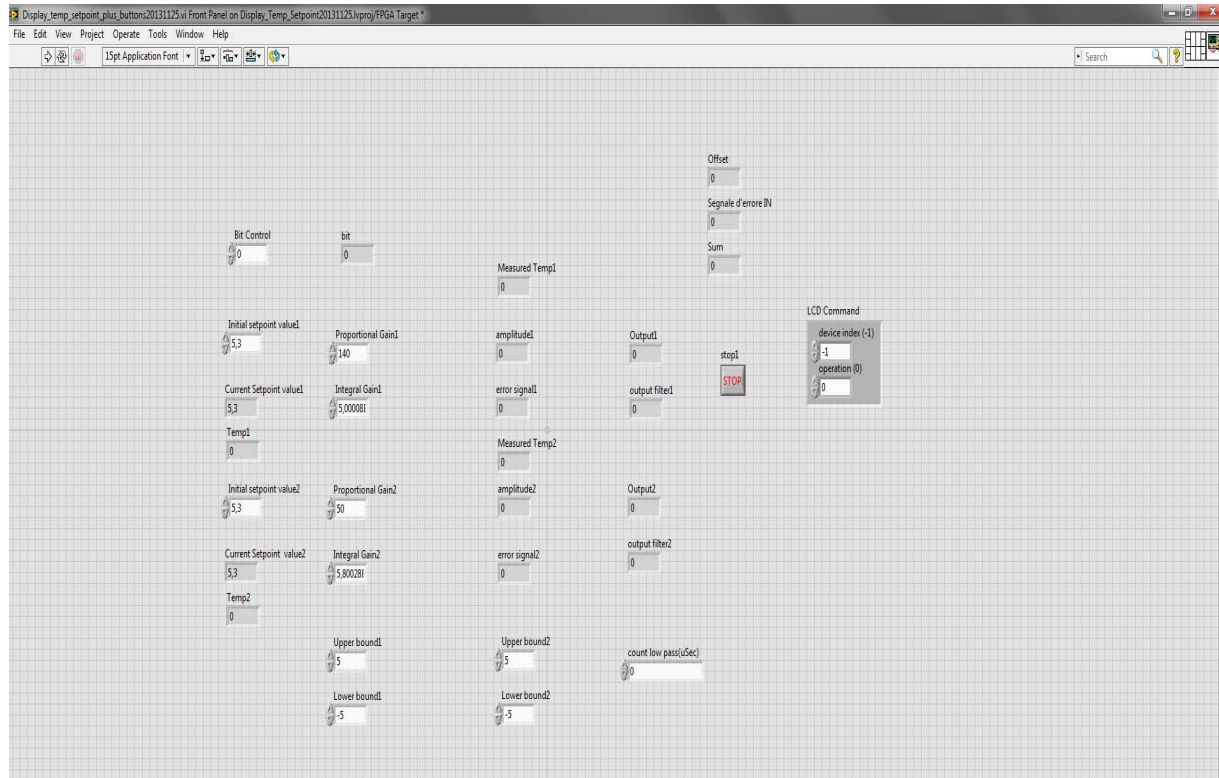

Figure 2.13: FPGA VI Front Panel.

Figure2.12 shows the Block Diagram of our FPGA VI. In the follow-

ing we will give a detailed description of the different blocks placed inside this diagram. First, just to give an overview, it is possible to identify in the figure various kinds of structures, that develop different tasks. The outermost is labelled "While Loop Structure" and it allows to implement the logic functions represented by the blocks inside its borders. The block indicated as "PZT control" establishes the connections between the Single-Board RIO and the electronic box, as sketched in fig.2.7. There are then structures that determine the action of NI RIO Evaluation device buttons (labelled "Case Structure" in fig.2.12). Finally, the two "Sequence Structures" placed to the right of the Block Diagram, realize the actual control that allows to stabilize the external cavity and diode temperatures, through a $Proportional - Integral$ action.

The outermost structure, that includes all the other diagram elements, is called "While Loop Structure": this kind of structure implements the logic functions realized by the elements placed inside its borders. It features two variables, called $"stop"$ and $"i"$, but is often useful to introduce a third variable, that we named $"tick\ count\ low\ pass"$, that fixes the iteration frequency of the loop (we chose a loop time constant equal to 1 μs). $"stop"$ is a boolean variable: when it is TRUE, the "While Loop Structure" execution is interrupted. Its value can be controlled through the VI Front Panel button called $"STOP"$ if the $NIsbRIO - 9636$ board is interfaced with a Windows OS processor, but when the FPGA VI runs automatically on the device because of the creation of a Stand-Alone Application, the process is only interrupted by the device power (we will discuss Stand-Alone Applications in appendix A). $"i"$ is a simple integer counting variable that is increased by 1 at each loop iteration.

Taking into account fig.2.12, we will describe the VI Block Diagram from left to right. The two variables $"Initial\ setpoint\ value\ 1"$ and $"Initial\ setpoint\ value\ 2"$, placed outside from the "While Loop Structure" left border, have assigned a fixed value that represents reference temperatures for the external cavity and for the diode, respectively (actually their values represent a voltage, that is then changed into into a temperature by a proper conversion, as will be discussed later). The third variable placed outside the "While Loop Structure" and called $"Bit\ Control"$ is an integer variable that can assume values from 0 to 6 and is used both as a push buttons command and an option menu for the LCD Screen located on the NI RIO Evaluation board (its use for this latter purpose is described in the following section that concerns the Real-Time Virtual Instrument). The three controls $"Initial\ setpoint\ value\ 1", "Initial\ setpoint\ value\ 2"$ and $"Bit\ Control"$ are connected to the "While Loop Structure" and their values are transferred through the loop by means of an element called "Shift Register"(it links the wires annexed to the variables to the "While Loop Structure" border and is depicted as an arrow inside a rectangular box). The variables "*Current Setpoint value* 1", "*Current Setpoint value* 2" and "*Bit*", placed inside the

"While Loop Structure", are indicators bonded to the three previous control variables, that allow to show their current values. $''Initial\ setpoint\ value\ 1''$ and $''Initial\ setpoint\ value\ 2''$ are controlled by buttons "PB 2" and "PB 4" on the NI RIO Evaluation device, represented in the block diagram by the FPGA targets called "$DIO13$" and "$DIO15$" (as a general rule, a FPGA target can be added to the VI Block Diagram from the Project Explorer Window, just expanding the folder in which it is located and dragging it to the desired position).
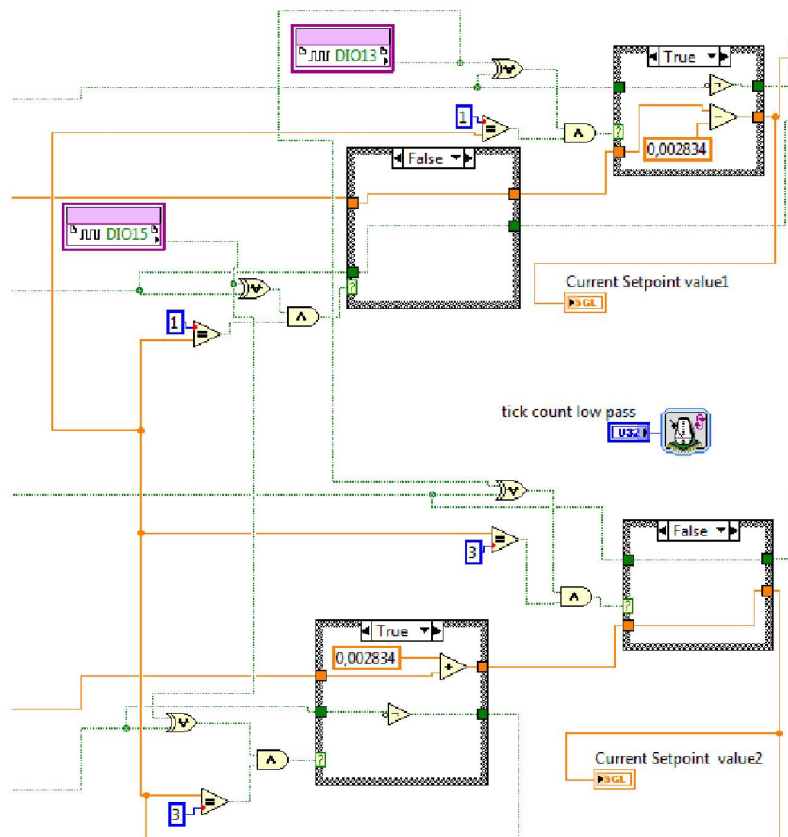

Figure 2.14: Insight of the FPGA VI Block Diagram, that shows the "Case Structures" controlled by push buttons2 ($DIO13$) and 4 ($DIO15$).

Fig.2.14 shows the next function we encounter moving slightly to the right inside the VI Block Diagram, named "Case Structure". It receives as an input the boolean or integer values assumed by the question mark $''?''$, fixed at the structure left border. Depending on the input value, the "Case Structure" performs different functions (the number of possible functions is the same as the number of the question mark $''?''$ possible values). We

want to refer now to the "Case Structures" represented in Fig.2.14, that correspond to the control variables $''Initial\ setpoint\ value\ 1''$ and $''Initial\ setpoint\ value\ 2''$. They are characterized by a boolean question mark input $''?''$, whose value is determined by the sequence of a logic XOR (exclusive or) function and an AND function: the first acts between the boolean values assumed by the push buttons during the n-th and $(n-1)$-th iterations of the "While Loop Structure", while the AND function is between the XOR result and the boolean outcome of the equality comparison between the actual integer value of the variable $''Bit\ Control''$ and a fixed integer constant (we point out that the FPGA digital I/Os corresponding to a push button assumes the boolean status TRUE whenever the button is pressed, while FALSE if not). Depending on the result of the equality comparison, if the "Case Structure" input $''?''$ is TRUE, button2 ($DIO13$) decreases the value of the two variables $''Initial\ setpoint\ value\ 1''$ or $''Initial\ setpoint\ value\ 2''$ by a certain amount (if $''Bit\ Control'' = 1$ then $PB2$ acts on $''Initial\ setpoint\ value\ 1''$, while if $''Bit\ Control'' = 3$, $PB2$ acts on $''Initial\ setpoint\ value\ 2''$). The same holds for button4 ($DIO15$), with the only difference that in this case the variables $''Initial\ setpoint\ value\ 1''$ and $''Initial\ setpoint\ value\ 2''$ are increased by the same amount as before. On the other hand, if $''?''$ is FALSE, the variable values are unchanged by the "Case Structure" and they will be the same during the following "While Loop Structure" iteration.

Fig.2.15 reports the truth table for the "Case Structure" input variable $''?''$.

From the table it is possible to notice that the "Case Structure" input variable $''?''$ is TRUE during both moments in which the button is pressed and released. For better understanding this feature, let us explain how the boolean values of the push button variables $DIO13$ and $DIO15$ are processed by the "Case Structure". They are transferred through the "While Loop Structure" by the same "Shift Registers" mechanism described before for the variables $''Initial\ setpoint\ value\ 1''$ and $''Initial\ setpoint\ value\ 2''$. If we define $t = 0$ to be the time at which a button is pushed during the n-th "While Loop Structure" cycle then, during the previous $(n-1)$ loop iteration, its boolean value was FALSE and thus the outcome of the XOR function is TRUE. If the result of the equality comparison is FALSE, the outcome of the logic AND between these two variables is FALSE and both the numerical and boolean values of the variables "*Initial setpoint value*" and "DIO" cross the "Case Structure" unchanged. On the other hand, if the equality comparison result is TRUE, the "Case Structure" input variable $''?''$ is TRUE and "*Initial setpoint value*" is then increased or decreased while crossing the "Case Structure". In this situation, the boolean values of the variables DIO are reversed by the logic NOT placed inside the "Case Structure". If it were not, the FALSE corresponding to the status of the button during the $(n-1)$ cycle, would be transmitted through the

Push Button (PB)		"PB actual value" XOR "PB previous value"	"Equality" = TRUE	XOR outcome AND "Equality"
Actual value	Previous value			
T	T	F		F
T	F	T	T	T
F	T	T		T
F	F	F		F
			"Equality" = FALSE	
T	T	F		F
T	F	T		F
F	T	T	F	F
F	F	F		F

Figure 2.15: Truth table that describes the control on the "Case Structure" input variable "?". We observe that the AND acts as a filter for the XOR outcome: if the equality (third column) is satisfied, then the AND leaves the XOR unchanged while, if the equality is not fulfilled, the AND result is necessarily FALSE. If we consider that the boolean value TRUE corresponds to a pressure on the button, while FALSE corresponds to the situation in which the button is not pressed, it is clear that the "Case Structure" input variable "?" is TRUE during both moments in which the button is pressed and released.

"While Loop Structure" during the following loop iterations and the "Case Structure" input variable "?" would result TRUE until the button is pressed. Hence, the variable "*Initial setpoint value*" would be raised or decreased (by

the fixed amount written inside the "Case Structure") for a number of times equal to the integer part of the fraction $t_{push}/t_{"WhileLoop"}$, where we defined t_{push} to be the average time during which a button is pressed by a user and $t_{"WhileLoop"}$ is the time constant of the "While Loop Structure". This would cause an extremely rapid and uncontrollable growth or decrement of the variable $"Initial\ setpoint\ value"$ (in fact the "While Loop Structure" time constant is much smaller than the typical last of time during which a user can press a button, i.e. $t_{"WhileLoop"} = 1\mu s$). The other situation in which the "Case Structure" input variable $"?"$ is TRUE corresponds to the instant at which the button is released: the push button boolean status becomes FALSE, while the one corresponding the previous loop iteration was TRUE (of corse, whatever is the outcome of the XOR, the equality condition must be fulfilled, in order for $"?"$ to be TRUE).
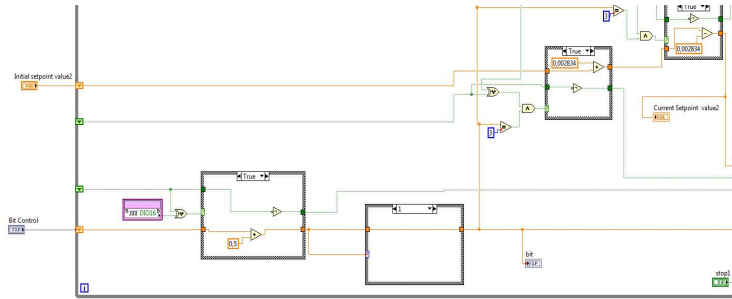

Figure 2.16: FPGA VI Block Diagram: insight of the lower left part of fig.2.12. The sequence of the two "Case Structures" that process the variable named $"Bit\ Control"$ is shown.

We can now focus on the FPGA VI Block Diagram part that concerns the process of the variable named $"Bit\ Control"$ (whose sketch is shown in fig.2.16). This variable, that is placed outside from the "While Loop Structure", initializes the indicator $"Bit"$ with the integer 0, as shown in the

FPGA front panel (fig.2.13). It is then processed by a sequence of two "Case Structures": the first is characterized by a boolean input question mark $''?''$, controlled by the push button $PB5$ on the NI RIO Evaluation device (this button corresponds to the digital I/O $DIO16$ on the Single-Board RIO), while the second has an integer "Case Structure" input $''?''$, whose value fixes that of the variable $''Bit\ Control''$. As before, $''Bit\ Control''$ is transferred through the "While Loop Structure" by the "Shift Registers" and the same holds for the FPGA digital I/O $DIO16$. The input $''?''$ of the first "Case Structure" is controlled by a logic XOR and thus the same considerations we did for the third column of fig.2.15 are valid. So, it is possible to deduce that at the time $t' = t + t_{push}$ (with t corresponding to the moment in which the button number 5 is pushed during the n-th "While Loop" iteration), $''Bit\ Control''$ is increased by one, with respect to the value it had during the $(n-1)$-th cycle. In the opposite situation in which $DIO16$ is FALSE, $''Bit\ Control''$ and $DIO16$ are unchanged by the action of the "Case Structure".
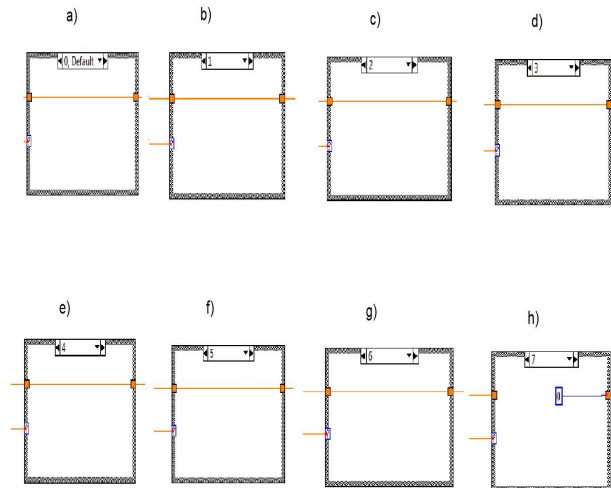

Figure 2.17: FPGA VI Block Diagram: insight of the second "Case Structure" for the $''Bit\ Control''$ variable: sequence of the eight possible values for the integer "Case" input $''?''$.

Figure 2.17 reports the sequence of the eight possible values for the integer input $''?''$ of the second "Case Structure" of fig.2.16. It receives the

value of the variable $''Bit\ Control''$, after it is processed by the push button $PB5$, and it basically acts as a value selector for this control variable: $''Bit\ Control''$ is left unchanged until $''?''$ ranges from zero to 6, while the "Case Structure" returns zero when $''?'' = 7$. The presence of this "Case Structure" will be clarified later, when we will discuss its usefulness as an option menu variable for the LCD display.

Thus, at this point, we can summerize the left part of the FPGA VI Block Diagram just explained with the following sketch for the hierarchy of the controls on the three digital I/O variables: $DIO13$ ($PB2$), $DIO15$ ($PB4$), $DIO16$ ($PB5$) and on the three numeric variables: $''Initial\ setpoint\ value\ 1''$, $''Initial\ setpoint\ value\ 2''$, $''Bit\ Contol''$.

DIO16 (Push button 5)

↓

Bit

↓

DIO13 (Push button 2), **DIO15** (Push button 4)

↓

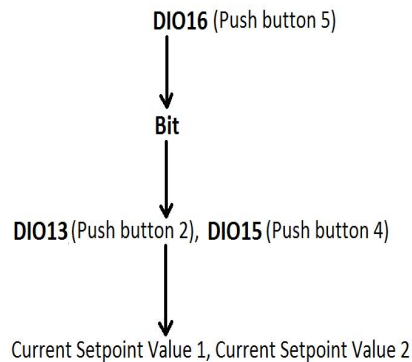Current Setpoint Value 1, Current Setpoint Value 2

Figure 2.18: Scheme of the controls hierarchy for the digital I/O $DIO13$ ($PB2$), $DIO15$ ($PB4$), $DIO16$ ($PB5$) and for the three numerical variables $''Initial\ setpoint\ value\ 1''$, $''Initial\ setpoint\ value\ 2''$, $''Bit\ Control''$. Indeed, the $DIO16$ boolean status determines the integer value assigned to $''Bit\ Control''$ and on it depends the action of buttons 2 and 4 on the variables $''Initial\ setpoint\ value\ 1''$ or $''Initial\ setpoint\ value\ 2''$.

Until now we only examined the "Case Structures" controlled by the values 1 and 3 of the integer variable $''Bit\ Control''$. As we will see when the Real-Time VI will be described, the action of this variable corresponds to display, on the NI RIO Evaluation device LCD Screen, the actual reference temperatures of the cavity and the diode, respectively. The other integer values that it can assume (i.e. 0, 2, 4, 5 and 6) are not used to control any other part of the FPGA VI Block Diagram and simply correspond to different options that allow to display, on the LCD Screen, the values assumed by different variables in the FPGA VI Block Diagram.

The right part of the FPGA VI Block Diagram of fig2.12 involves two identical "Sequence Structures": the upper one is referred to the analog input and output $AI0$ and $AO0$ of the Single-Board RIO, that are connected

to the external cavity thermistance and Peltier, respectively. The same holds for the lower "Sequence Structure", with the difference that it refers to the diode and thus $AI1$ and $AO1$ are involved (as shown in fig.2.7). A sequence structure is a function that consists of a various blocks (three in our case), temporally processed from left to right. We will refer to figure2.19 for its description. As the two "Sequence Structures" pictured in the FPGA VI Block Diagram are identical in all features, it makes no difference if we refer to the first or to the second one.
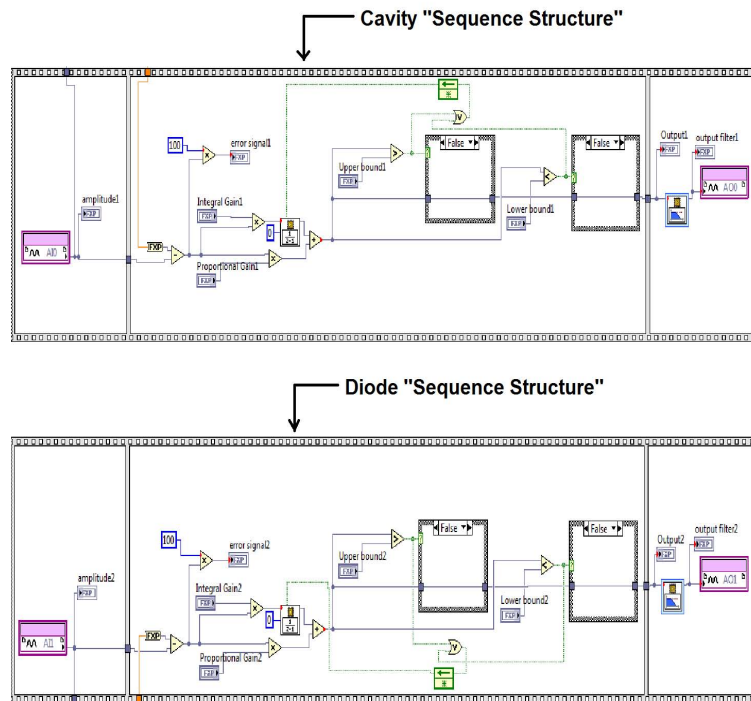

Figure 2.19: "Sequence structures" of the FPGA virtual instrument: the upper one refers to the external cavity temperature stability control, while the lower one to the diode temperature stability control. They both consist of three identical blocks and, accordingly to the peculiar feature of a "sequence structure" function, they are processed from left to right.

The first block of the sequence represents the analog input channel of the $NIsbRIO-9636$ device, through which a voltage signal from the diode or cavity thermistances is acquired. As shown in fig.2.20 (that represents the "Sequence Structure" of the external cavity), this input signal is transferred to the two variables named $"Amplitude1"$ and $"Measured"$ $"Temp2"$: the first one simply represents the input voltage just as it is, while this signal is then converted into the corresponding temperature and then transferred to

the second variable (you can refer to the description concerning the voltage-temperature conversion given at the end of the present treatment about the FPGA VI). When the device is interfaced with a Windows OS processor, it is possible to monitor the values of these two variables (as those of all the others) from the FPGA VI Front Panel. In the central block of the "Sequence Structure", the difference between the analog input voltage and a reference value (indicated by the variable $Current\ Setpoint\ value$) is processed by a $Proportional-Integral$ (PI) controller (whose details are given in the description at the end of this section). The variable that we called "$error\ signal$" ("$error\ signal$" $=$ "$amplitude$" - "$Current\ Setpoint\ value$") is used as an indicator, in order to monitor the difference between the actual temperatures of the cavity and the diode with respect to their reference values. Then, the funcion of the two "Case Structures" is to provide an upper limit to the absolute value of the $Proportional-Integral$ controller output: the variables "$Upper\ bound$" and "$Lower\ bound$" have assigned values $\pm 5V$ and, if the PI output absolute value exeeds this limit, the signal transferred to the third block of the "Sequence Structure" is fixed at $+5V$ or $-5V$ by the "Case Structures", respectively. Fig.2.21 shows an insight of the second block of the diode "Sequence Structure".
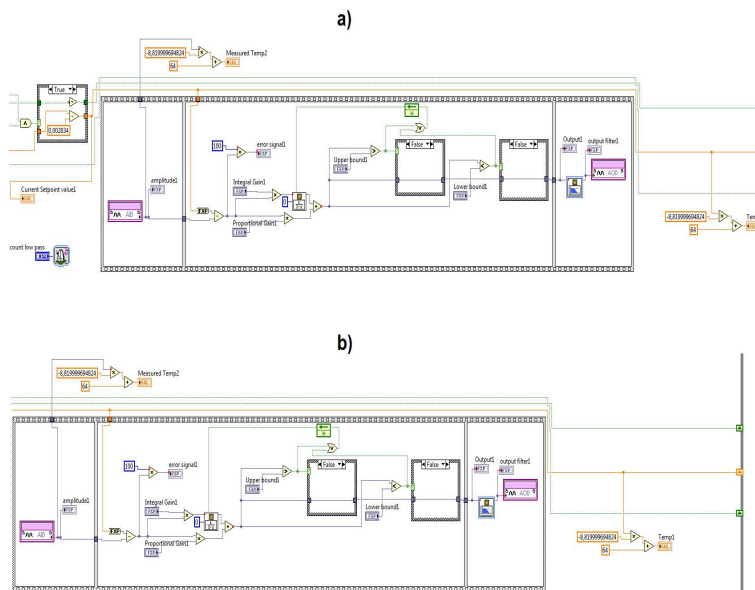

Figure 2.20: Cavity "sequence structure" in the FPGA Virtual Instrument Block Diagram.

In the third block, the signal is processed by a "Butterworth Filter" and then sent to the corresponding $NIsbRIO - 9636$ analog output. A "Butterworth Filter" is a Virtual Instrument provided by LabVIEW (these kind of Virtual Instruments are technically called "Express VIs"), whose function is to filter one or more input signals using a lowpass filter. When the Single-Board RIO device is connected to a Windows OS processor, thanks to the two variables named $"Output"$ and $"output\ filter"$, it is possible to display on the FPGA Virtual Instrument Front Panel the values of the variable $"error\ signal"$ (after it is worked out by the $Proportional - Integral$ controller), before and afterwords the "Butterworth Filter" action.

Eventually, the last operation that appears inside the "While Loop Structure" is the conversion of variables $"Current\ Setpoint\ value$ 1" and $"Current\ Setpoint\ value$ 2" (whose values represent a voltage) into the two corresponding variables $"Temp1"$ and $"Temp2"$, that represents the reference temperatures for the external cavity and for the diode, respectively.
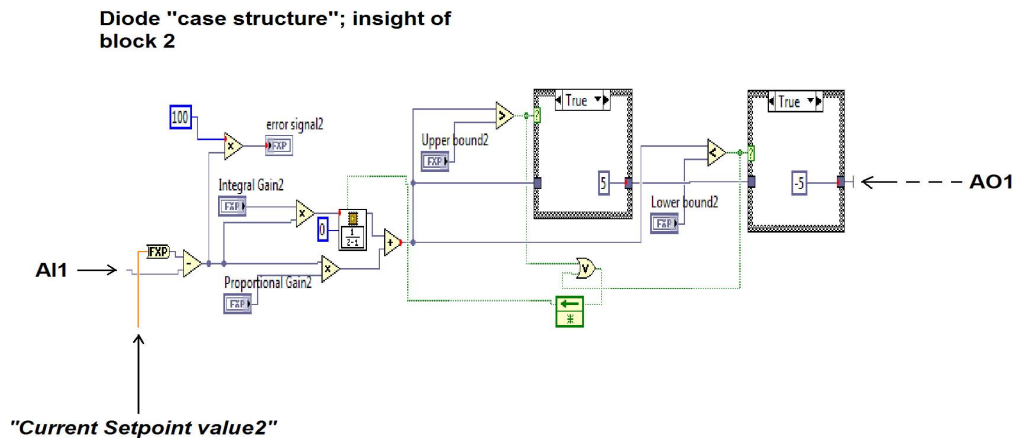

Figure 2.21: Insight of the central block of the diode "Sequence Structure", in the FPGA Virtual Instrument Block Diagram. The error signal ($error\ signal2 = amplitude2$ - $Current\ Setpoint\ value2$) is processed by a $Proportional - Integral$ (PI) version of a more common $Proportional - Integral - Derivative$ (PID) controller.

The values of the numerical variables $"Initial\ setpoint\ value$ 1", $"Initial\ setpoint\ value$ 2" and $"Bit\ Control"$, as well as those of the boolean Push

Buttons variables $DIO13$, $DIO15$ and $DIO16$, are then processed by the
"Shift Register" functions placed at the "While Loop Structure" right border
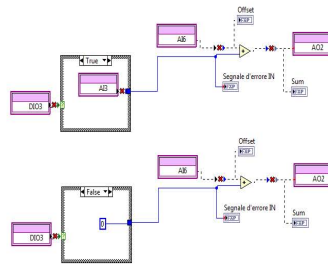and transferred to the next "While Loop" iteration.

Figure 2.22: FPGA VI Block Diagram: piezo-electric transducer (PZT)
connections.

One last observation about the FPGA VI Block Diagram concerns the
block of connections placed to the top left side of fig.2.12, whose enlargement
is shown in fig.2.22. The scheme simply shows the connections between the
analog inputs and outputs for the voltage signal sent to the piezo-electric
transducer through the output of the box called $BNC5$ (refer to the scheme
of fig.2.7).

The PID controller :

Now, we want to discuss the specific controller we realized in order to ensure
the diode and external cavity temperature stabilizations. In the FPGA VI
Block Diagram, this task is carried out inside the second block of the "Se-
quence Structures" pictured in fig.2.21 and a magnification is represented in

fig.2.23.

We used a *Proportional − Integral* (*PI*) version of the commonly used *Proportional − Integral − Derivative* (*PID*) controller. A (*PID*) is a negative-feedback system largely used in control systems. Its fundamental principle is based on the comparison of an input value from the process to be stabilized, with a reference value and their difference (called the "error signal") is processed in order to determine the value of the controller output variable.
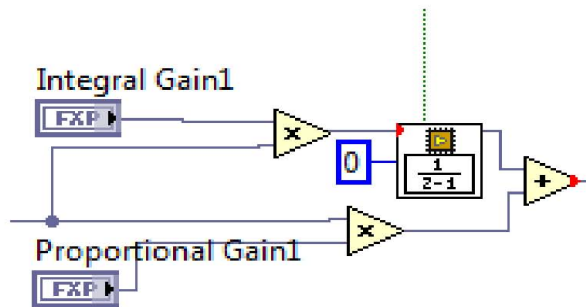

Figure 2.23: The FPGA VI *Proportional − Integral* (*PI*) controller.

The PID action opposes to the error signal and, whatever it is positive or negative, the controller makes the error signal to tend to zero. The PID response to the error signal is based on three main features: the actual error signal value (proportional), the set of the error signal values during the previous iterations (integral) and the rate of variation of the error signal (derivative). If we now refer to the different correction signals, proportionality constants (called "gain constants") and error signals with letters u, K and e, respectively, we have:

$$u_P(t) = K_P e(t) \tag{2.14}$$

$$u_I(t) = K_I \int e(t)dt \qquad (2.15)$$

$$u_D(t) = K_D \frac{de(t)}{dt} \qquad (2.16)$$

These correction signals are generated independently and the overall outcome is just the sum of the three:

$$u = u_P + u_I + u_D \qquad (2.17)$$

The proportional action is simply obtained by multipying the error signal by a proper proportional gain constant. In spite of the fact that it is possible to stabilize a process only with a proportional action, it does not ensure the convergence of the input signal to the reference value, as the proportional control is only possible if there is an error signal different from zero. On the other hand, this is allowed by the integral action; in fact, being proportional to the error signal time integral, it takes into account the values it had during previous iterations and thus the integral action is not necessarily null when the error signal is zero. Finally, the derivative action is proportional to the the time derivative of the error signal through the gain derivative constant K_P and turns out to be necessary if rapid compensations to the error signal variations are needed. In our case the average time scale on which temperature stabilization has to be achieved, is of the order of tens of seconds (from 10 s to about 30 s, depending on different factors that include for example the initial error signal absolute value and the temperature of the surrounding environment). Indeed, our controller consists only of propotional and integral actions: from figure 2.23 it is possible to notice that the error signal (represented by the difference between the variables $''amplitude''$ and $''Current\ Setpoint\ value''$) is processed both by a proportional action, given by the proportional gain constant $''Proportional\ Gain''$, and by an integral action, with an integral gain constant given by the variable $''Integral\ Gain''$ (the two variables $''amplitude''$ 1 and 2 are simply indicators, used to display the actual $AI0$ and $AI1$ voltages). The integral action is performed by an "Express VI" called "Discrete Normalized Integrator" and represented by a rectangular box in the figure. It integrates a discrete input signal, assuming the integration interval (dt) normalized to 1. The $input$ data channel of the "Discrete Normalized Integrator" receives the value: $(errorsignal) \times {''Integral\ Gain''}$ and returns the $output$ integration result: $output[n] = input[n-1] + output[n-1]$, where $output[n]$ is the value of $output$ on the n-th call to the Virtual Instrument and $output[0]$ in figure2.23 equals the $initial\ condition$ value. The channel placed to the left side of the VI and connected to the value 0 is called $initial\ condition$ and is the value the VI returns when it is called for the first time. The boolean channel called $reset$ initializes the "Discrete Normalized Integrator" to the $initial$

condition value when it is TRUE: in our specific case, the Virtual Instrument is initialized to zero when the *output* value exeeds $\pm 5\ V$, thanks to the logic OR function between the comparisons of the $Proportional - Integral$ result with the variables $''Upper\ bound'' = +5V$ and $''Lower\ bound'' = -5V$ (look at figure2.21). The reason why we temporarily reset the integral action when the PI output is saturated, is because we observed that, in this situation, the time required for the error signal to go to zero was much smaller when there was only a proportional action, if compared to the situation in which both integral and proportional are present for every value of the error signal. We chose the gain parameters to be $K_P = 50$, $K_I = 5.8 \times 10^{-5}$ for the PI controller corresponding to $AI1$ and $AO1$ (diode temperature control) and $K_P = 140$, $K_I = 5 \times 10^{-5}$ for $AI0$, $AO0$ (external cavity temperature control). The way in which we could optimize these proportionality constants was to observe with an oscilloscope (connected in parallel with the external cavity and diode thermistors through $BNC2$ and $BNC3$ of fig.2.8), when the critical regime was achieved. The critical gain K_u is defined as that gain value for which the variable under control presents significant oscillations, that do not go to zero after a transient. According to the Ziegler-Nichols method, we determined K_u using only a proportional action that was gradually increased until the critical regime was settled. A integral action was then added and the proportional and integral gain constants were chosen in order to ensure the oscillations amplitude to go to zero in the least possible time, while the signals to be processed were stabilizing on their reference values (defined by the variables $''Initial\ setpoint\ value\ 1''$ and $''Initial\ setpoint\ value\ 2''$). Figure2.24 shows the set of measurements we did to characterize the diode temperature stabilization as a function of time.

We usually set the diode and external cavity temperatures to the same value because, monitoring the variables $''Current\ Setpoint\ value\ 1''$ and $''Current\ Setpoint\ value\ 2''$ from the FPGA VI Front Panel, we could notice the appearance of an offset between the temperatures of the external cavity and the diode, when $''Initial\ setpoint\ value\ 1''$ and $''Initial\ setpoint\ value\ 2''$ were assigned different values (the entity of the offset increased when the difference between the two reference temperatures was raised). The reason of this behaviour is explained if we take into account the fact that the thermal capacitance of the cavity is much greater than that of the metallic part in which the diode is held (part 1 of fig.2.2). Thus, the diode can't reach its reference temperature due to the dominant thermal effect of the external cavity.

The last feature that we want to point out, as far as the PI of fig.2.23 is concerned, is to explain the reason why we built a $Proportional - Integral$ controller dividing the two tasks, instead of using the Expressed VI called PID that is provided by LabVIEW. Actually, the first version of our FPGA VI consisted of two PID Express VIs that replaced the PI but, when we tried to optimize the proportional and integral gain parameters, we no-
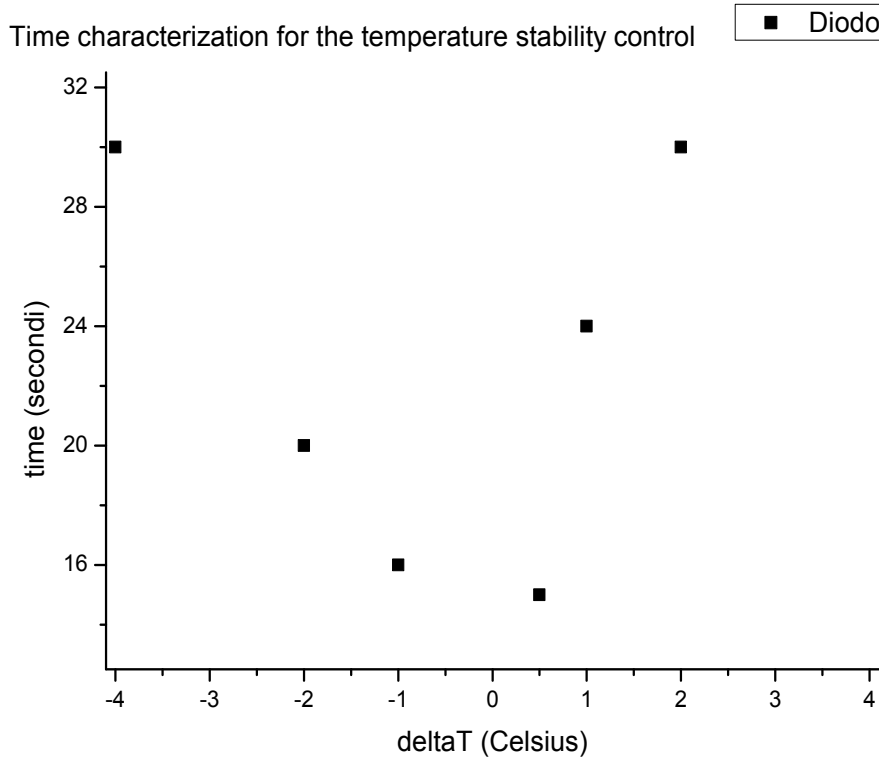
Figure 2.24: Time versus temperature characterization for the diode temperature feedback system: the measurement was performed by a direct reading, on the FPGA VI Front Panel, of the values of the variable $"Current$ $Setpoint\ value\ 2"$, that represents the actual voltage corresponding to the diode temperature. This voltage signal was then converted into the corresponding temperature (using the thermistance voltage-temperature conversion discussed in the next section), as reported on the horizontal axis.

ticed that there was a lower limit to the allowed value of the integral gain: $K_I = 1.95318 \times 10^{-3}$. With this value the system was in the oscillating regime and temperature stabilization could not be achieved.

The thermistor voltage − temperature calibration :

The experimental procedure we used to find the conversion between the voltage signals, coming to the Single-Board RIO through $AI0$ and $AI1$ from the 10 kΩ thermistor in thermal contact with the cavity and the diode, respectively, was to measure the external cavity temperature with a thermocouple, while the corresponding voltage was red from the FPGA VI Front Panel,

after thermal equilibrium was reached (the external cavity and the diode can attain the same temperature because they are in thermal contact and they have identical thermistor, as well as identical reference temperatures). The dataset we took ranges from 4.6 V to 5.35 V and the corresponding temperatures are reported in fig.2.25. The linear fit represented in the figure provides the following conversion from voltage to temperature:

$$T(^\circ C) = (-8.82 \pm 0.08) \times V(Volt) + (64.0 \pm 0.4)^\circ C \qquad (2.18)$$

Fig.2.26 shows the part of the FPGA VI Block diagram that provides this conversion.

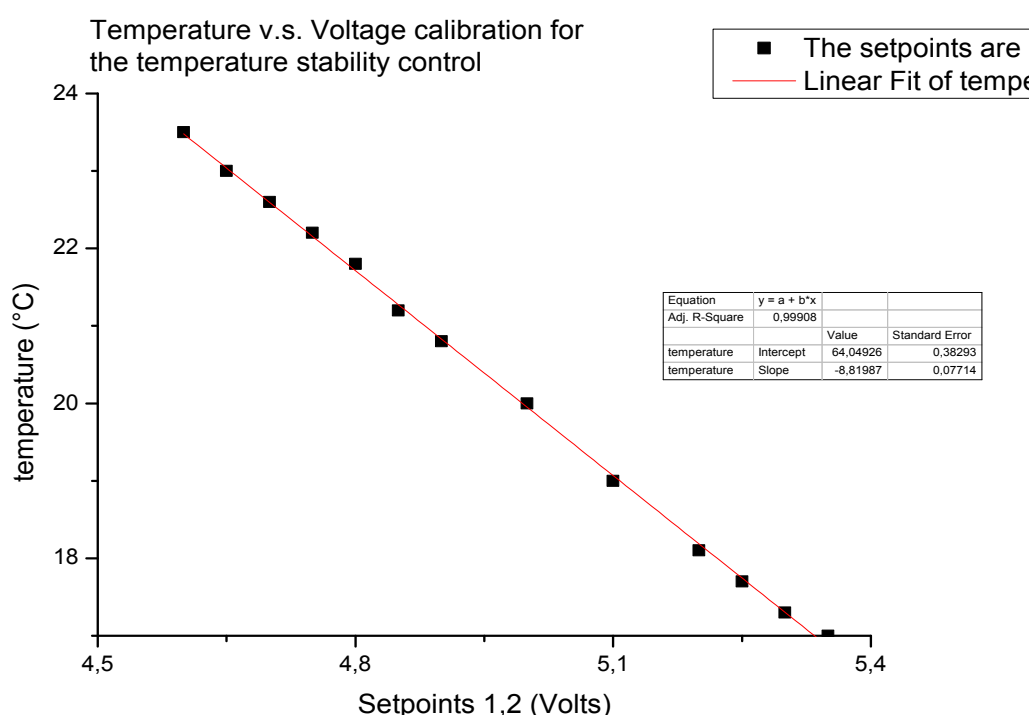| Equation	y = a + b*x		
Adj. R-Square	0,99908		
		Value	Standard Error
temperature	Intercept	64,04926	0,38293
temperature	Slope	-8,81987	0,07714

Figure 2.25: Thermistance voltage-temperature calibration curve.

Finally, from fig.2.14 we can deduce that the increase (or decrease) by the fixed amount of $\Delta V = 0.002834$ V shown in the figure, corresponds to the step $\Delta T = 0.025$ °C (remember that, as the "Case Structures" input variable $''?''$ is TRUE during both moments in which a button is pushed and then released, the actual voltage and temperature increments, or decrements, are $2 \times \Delta V = 0.005668$ and $2 \times \Delta T = 0.05$ °C). This means that, if $''Bit\ Control'' = 1$, buttons 2 and 4 decrease and raise, respectively, the cavity setpoint temperature each time they are pressed while, if $''Bit\ Control'' = 3$, they act in the same way for the diode setpoint temperature.
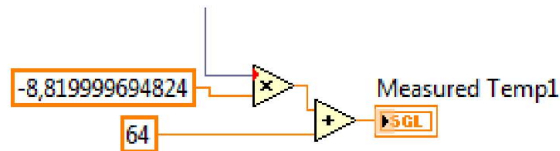
Figure 2.26: FPGA VI Block Diagram: voltage-temperature conversion.

The Real − Time Virtual Instrument

To describe the Real-Time VI we start from the part of the FPGA VI Block Diagram shown in fig.2.27.

This part of the FPGA VI was taken from the NI RIO Evaluation tutorial and the "While Loop Structure" shown in the figure allow to create a communication channel between the LCD Screen of the NI RIO Evaluation board (that is controlled by the Real-Time processor) and the FPGA chip on the NI Single-Board RIO.

The actual Real-Time VI Block Diagram is displayed in fig.2.28. As we did for the FPGA VI description, we can proceed with the description of the Block Diagram of this Virtual Instrument starting from left to right. The Real-Time VI initialization is due to the function called "Open FPGA VI Reference": it is initialized with the FPGA VI described in the previous section (dragging the corresponding FPGA VI Target from the Project Explorer Window to the "Open FPGA VI Reference" function) and is needed because it allow to execute this Virtual Instrument on the FPGA chip. The Real-Time VI is mainly featured by the presence of two "While Loop Structures": the upper one has the task of communicating the output values of the FPGA VI variables to the Real-Time processor, while the lower structure provides the control on the LCD Screen.

This lower "While Loop Structure" is characterized by the presence of
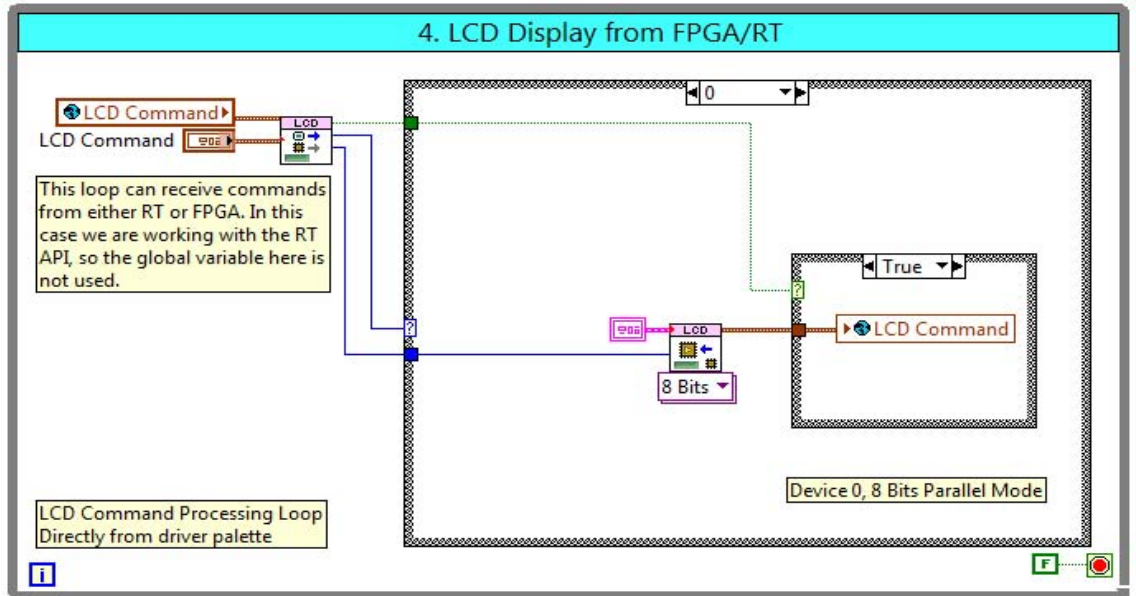
Figure 2.27: FPGA VI Block Diagram: communication channel between the FPGA chip and the Real-Time microprocessor.
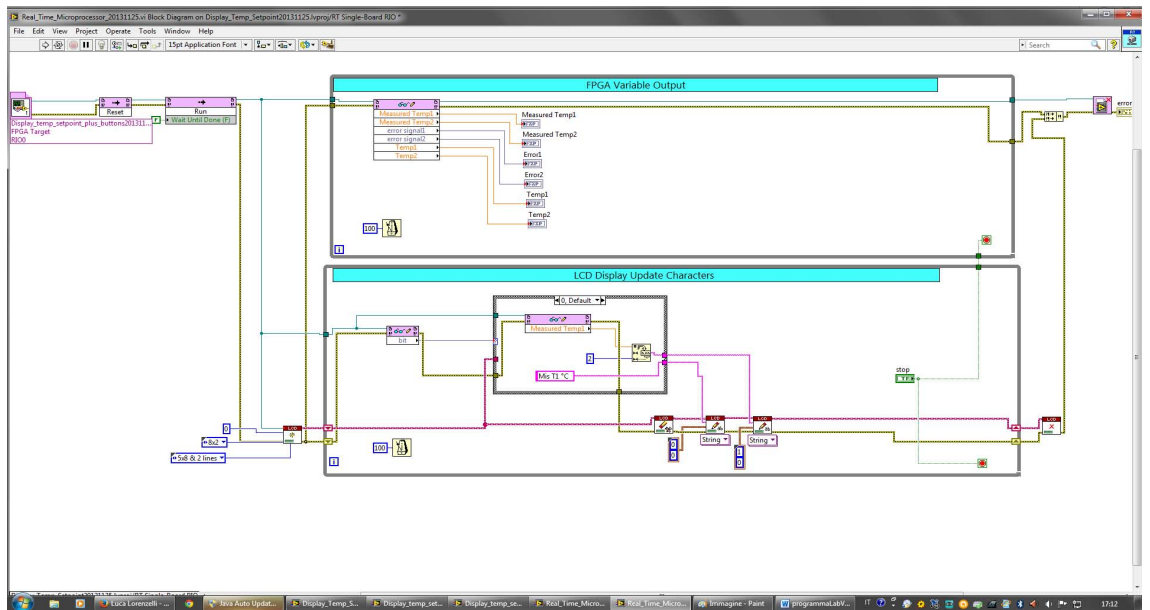

Figure 2.28: Real-Time VI Block Diagram. The first element placed in the upper part to the left is the "Open FPGA VI Reference" function, that is initialized with the FPGA VI just described in the previous section.

LCD commands and a "Case Structure". The LCD commands are located in the lower part of the diagram and are used to perform specific operations on the screen: the first one (placed out from the "While Loop Structure" left border), opens a communication with the LCD screen and initializes the writing position, as well as the LCD Screen dimensions (i.e. the number of characters for each row and column). The other two LCD commands we encounter inside the loop are needed in order to clear the screen and for writing new string values on it, respectively. The last command, placed outside from the "While Loop Structure" right border, is then used to close the communication with the LCD Screen.

The "Case Structure" receives an integer input value, provided by the FPGA VI variable called $"Bit"$. Correspondingly, it consists of a total of seven options, as displayed in fig.2.29. Depending on the value of $"Bit"$, a different FPGA VI variable value appears on the LCD Screen: when $"Bit = 0$ or $"Bit = 3$, the actual and reference temperatures of the diode are displayed while, when $"Bit = 1$ or $"Bit = 2$ the same temperatures are displayed for the external cavity. Furthermore, if $"Bit = 5$ or $"Bit = 4$, the current error signal values (equal to the difference between the actual and reference temperatures), for the diode and for the cavity, respectively, are shown, while the last option (corresponding to $"Bit" = 7$) simply makes the word "OFF" appear on the screen. A note is needed because the screen command that writes on the LCD Screen can receive only a string as input. This is the reason of the presence of the Express VI placed inside the "Case Structure", that receives the input numerical values of the FPGA variables and then provides the right conversion for the LCD Screen command to which it is wired.

The function placed to the top rigth side of the Real-Time VI Block Diagram is called "Close FPGA VI Reference" and it develops the opposite task of the corresponding function "Open FPGA VI Reference", placed at the opposite side of the diagram: it closes the data communication between the FPGA VI target and the Real-Time processor.
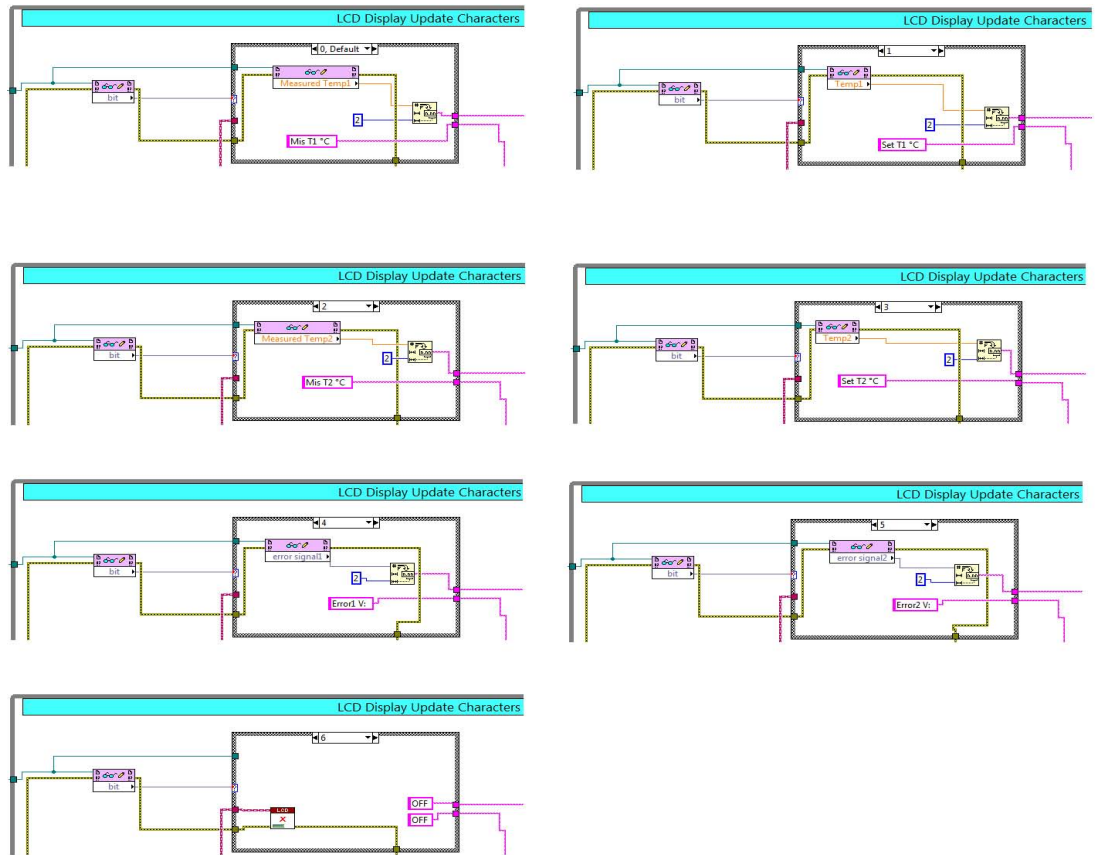
Figure 2.29: Real-Time VI Block Diagram: the "Case Structure".

2.5   Characterization of the laser system: measurements and results

The present section is devoted to describe the measurements and the analysis of the results we obtained during the characterization of the laser system treated in this chapter. As starting point we assume that all the procedures described in the previous sections and subsections have already been performed. With this we mean that the following conditions are fulfilled:

i) the mechanical setup of the external cavity (described in section 2.4), provides the best shape for the output laser beam, that is not cut by any mechanical component when it crosses the cavity and thus it has the maximum possible power after the "cat's eye" scheme. Also, the beam is horizontally and vertically aligned, in order to ensure a good optical feedback.

ii) The position of the optical elements has been chosen so that the beam collimations after the first lens $C330$ and after the cat's eye scheme are achieved.

iii) The diode position inside the copper disk (part ($B4$) in fig.2.3) is such that the polarization of the emitted light is vertical.

iv) The temperature feedback system described in subsection 2.4.4 has been developed and a Stand-Alone Application allow the FPGA and Real-Time VIs to run automatically on the $NIsbRIO - 9636$ device every time it is power supplied.

Subsection 2.5.1 will report the characterization of the laser diode when only the first collimating lens ($C330$) is present and part (1) is outside from the external cavity (see fig.2.2). Then, in subsection 2.5.2 we will compare the results of the previous subsection with those obtained with the diode laser inside the external cavity, with particular attention to the effect of the optical feedback on the threshold current region and to the power fraction transmitted by the partially reflecting mirror (the out-coupler). In subsection 2.5.3 we will discuss the effects produced by the dielectric interference filter used as wavelength selector: we will mainly focus on the performances achieved with the interference filter as far as the wavelength stability of our laser system is concerned and we could analyse its behaviour with respect to the external cavity and to the diode cavity jump modes. (Finally, in subsection 2.5.1, we will give an overview of the results obtained with the diode currently mounted, compared to those we got using different diode lasers.)

2.5.1 Laser beam characterization: the diode laser output power

The diode laser currently mounted on our system is the model $L785P090$, sold by THORLABS. This is a cathode ground diode laser that emits light at a typical wavelength of 785 nm. It can operate at a maximum supply current of 160 mA (even though the typical operating current is specified to be at 120 mA), with a maximum output power of 100 mW, as reported by the datasheet specifications. It features a typical threshold current of 35 mA and other manufacturer specifications will be given later, when needed (you can also refer to appendix B). The diode output power was measured first without the external cavity and then with, in order to compare the actual fraction of the power transmitted by the out-coupler with the nominal 70% value given by the manufacturer. The results obtained for the power versus current $P(I)$ curve are plotted in figure2.30. A common feature of the two curves is that they present a region that is clearly linear, while another in which the power suddenly increases from zero to finite values.

This latter region is characterized by a specific value of the current, called threshold current, that corresponds to the situation in which the lasing effect starts occurring. We can first focus on the linear part of the curves, whose equations, given by a linear fit, are:

$$P(mW) = (1.163 \pm 0.003) \times I(mA) - (35.4 \pm 0.3) \qquad (2.19)$$

$$P(mW) = (0.6118 \pm 0.002) \times I(mA) - (16.29 \pm 0.14) \qquad (2.20)$$

for the diode laser without the cavity and with the external cavity, respectively. If we divide the angular coefficients of the second equation by that of the first one, we get $Slope_{cavity}/Slope_{NoCavity} = 0.6118/1.163 \simeq 0.53$, that is considerably lower than the 70% given in the specifications of the partially reflecting mirror.

As far as the threshold current region is concerned, we could notice a rapid growth of the power (from 0.47 mW to 1.48 mW) between 31 mA and 32 mA, without the cavity. On the other hand, the effect produced by the external cavity was to lower the threshold current from 32 to 29 mA (in fact we observed a current increase from 0.43 mW to 1.62 mW between 28 and 29 mA), thanks to the optical feedback provided by the out-coupler. From the linear fits, we can verify if the threshold current lowering due to the external cavity is the same if we assume two different values of the diode's output power just before the threshold. We can for example consider the intersection of the linear parts of the curves in fig.2.30 with the horizontal axis at $P = 0$ mW and the arbitrary value $P = 1.5$ mW. The results are $\Delta I_0 = (3.8 \pm 0.5)$ mA and $\Delta I_{1.5} = (2.7 \pm 0.5)$ mA. The fact that these results are not compatible, but slightly outside the experimental errors, may depend on the fact that the diode's output power is not exactly zero when the current is below the threshold and the actual power at the threshold current could be lower than 1.5 mW (while we assumed this arbitrary value as the power emitted by the laser at the threshold). The threshold current errors were evaluated by the expression $\delta I_{TH} = \{[(\partial I_{TH}/\partial P_{TH}) \times \delta P_{TH}]^2 + [(\partial I_{TH}/\partial P_0) \times \delta P_0]^2 + [(\partial I_{TH}/\partial m) \times \delta m]^2\}^{\frac{1}{2}}$, where P_{TH} is the threshold current and we denoted with P_0 and m the intercept and slope of the linear fit curves, respectively.

Another observation is needed to compare the laser powers at the working current: at 120 mA the diode emitted power was 104.3 mW, while we obtained 57.7 mW of transmitted power by the partially reflecting mirror. Their ratio then corresponds to about 55% transmittance of the out-coupler, that is slightly higher with respect the average 53% evaluated before. Furthermore, this diode shows a better value for the emitted power with respect to the 90 mW reported in the datasheet specifications as the typical output power at 120 mA.
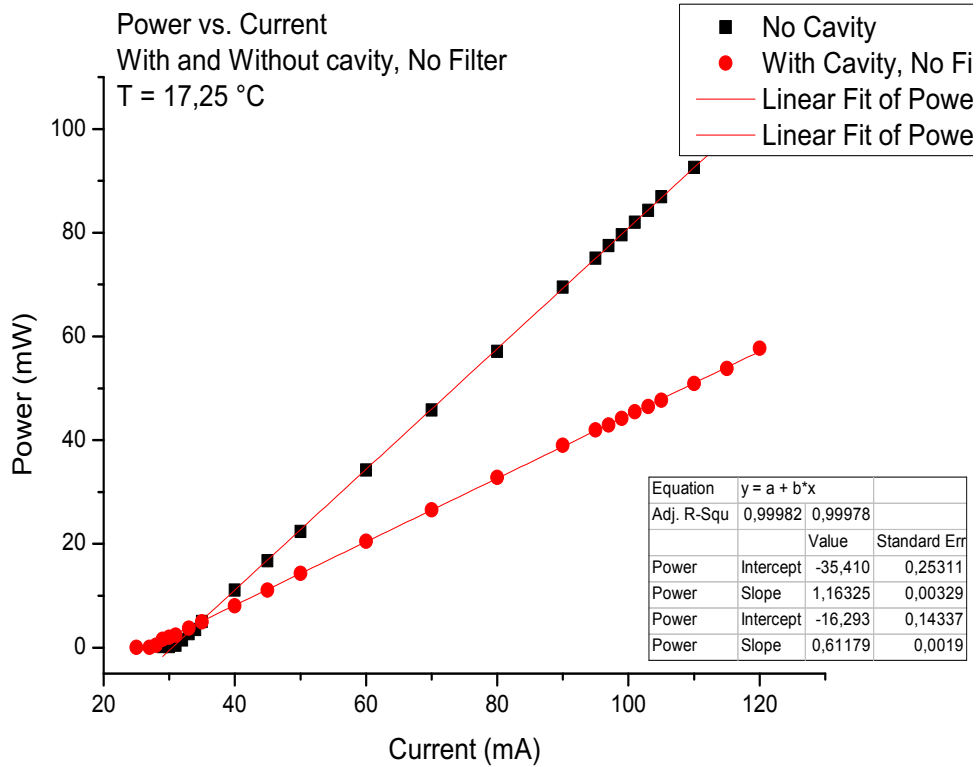
Figure 2.30: THORLABS $L785P090$ diode laser characterization: power versus current with the external cavity and without it. All measurements were performed keeping the temperatures of the external cavity and the diode fixed at 17.25 $°C$.

2.5.2 Laser beam characterization: wavelength versus current behaviour

The laser wavelength, before it was selected with the interference filter, was characterized with a diode laser of the same model of the one that is currently used (that was then replaced because it was broken by a sharp peak in the current supply). The results we obtained for the wavelength variation, while changing the diode supply current, are reported in figure 2.31.

From the wavelength versus current curve, it is possible to observe that there is not any significant hysteresis effect between the two point datasets.

A linear fit of the the two ramps gives:

$$\lambda(nm) = (3.29 \pm 0.07) \times 10^{-3} I(mA) + (781.880 \pm 0.007) \qquad (2.21)$$
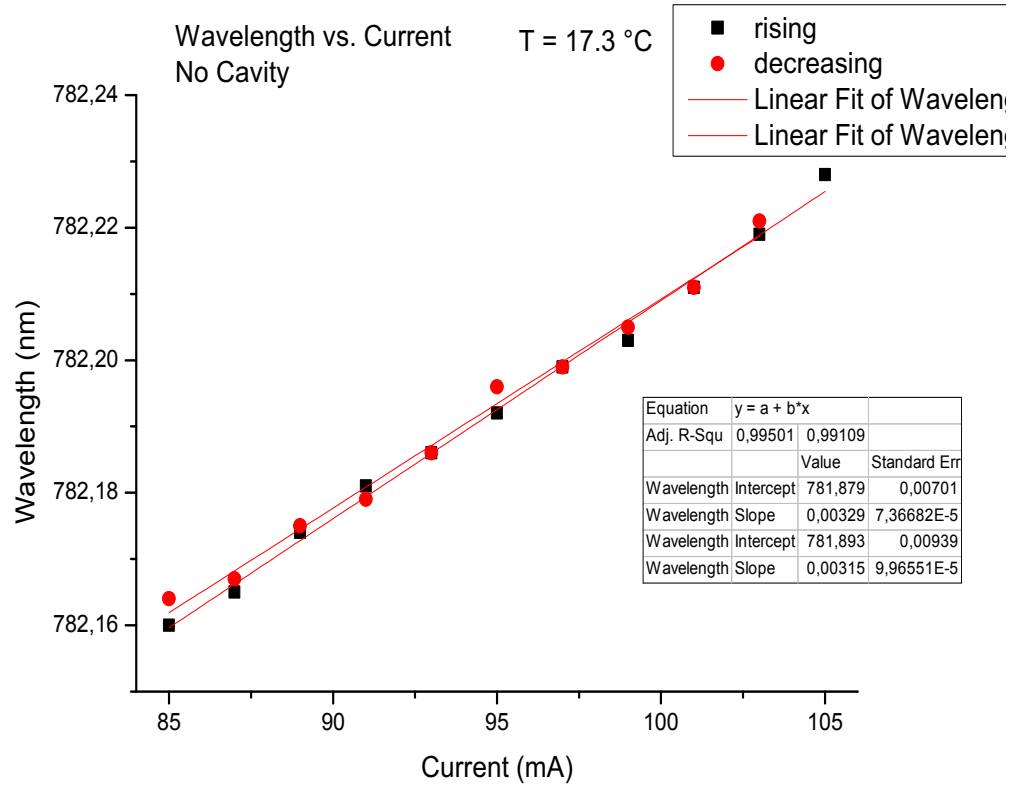
and

Figure 2.31: THORLABS $L785P090$ diode laser characterization: wavelength versus current curves in the operating current region. The measurements were performed at fixed temperature ($T = 17.3$ °C), with both increasing and decreasing current datasets, in order to point out the presence of any hysteresis effect.

$$\lambda(nm) = (3.2 \pm 0.1) \times 10^{-3} I(mA) + (781.894 \pm 0.009) \qquad (2.22)$$

The first relation refers to the set of measurements corresponding to increasing currents, while the second to the decreasing ramp. Equations 2.21 and 2.22 show an average wavelength increment, while increasing current, equal to:

$$\frac{d\lambda}{dI} \simeq 3\frac{pm}{mA} \qquad (2.23)$$

2.5.3 Laser beam characterization: wavelength versus temperature behaviour

Differently from the wavelength versus current curve, fig.2.32 shows a clear hysteresis effect: the increasing ramp shows a jump mode between 18.5 and 19.0 °C, while it is not possible to see the same effect in the temperature decreasing ramp (it would have probably been occurred at lower temperatures, but we did not decrease the diode temperature below 16 °C in order to avoid condensation of water vapours on it).
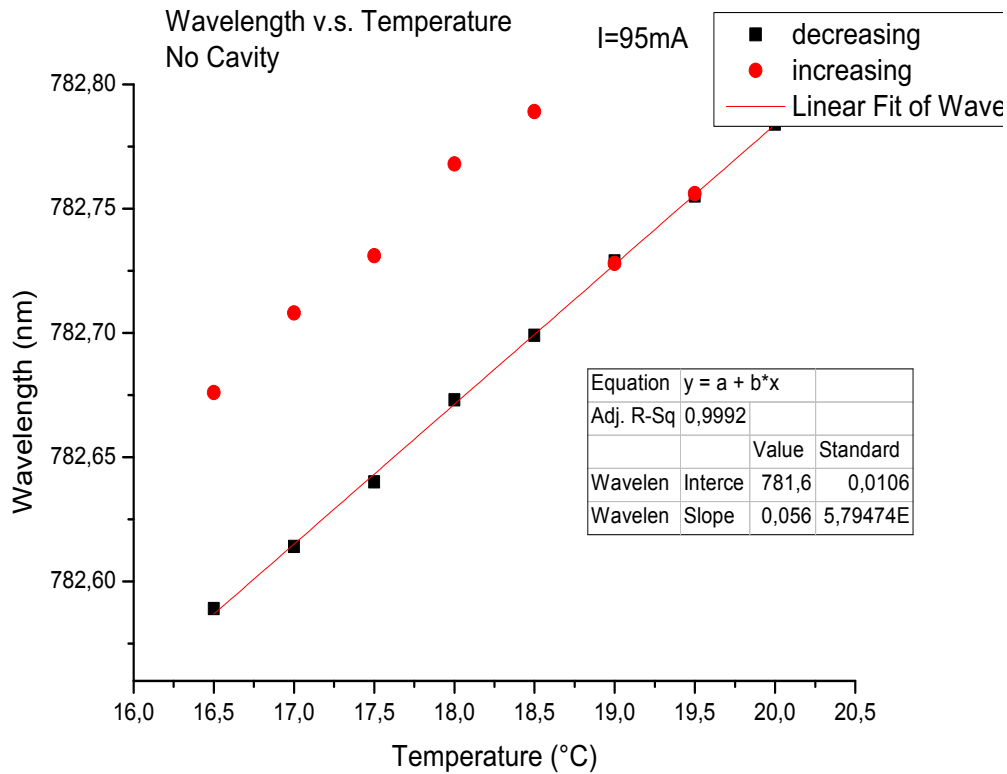

Figure 2.32: THORLABS $L785P090$ diode laser characterization: wavelength versus temperature curves. During the measurements the diode supply current was fixed at 95 mA. The presence of an hysteresis effect between the increasing and decreasing temperature ramps is evident.

If we use the average value of 91 pm for the difference between the wavelengths measured during the increasing and decreasing temperature ramps (fig.2.32), in the range from 16.5 and 18.5 °C, it is possible to give a rough estimation of the length of the corresponding cavity (we point out that the jump mode we observed does not necessarily represent a single jump of the cavity; it can also be an integer multiple of it and thus the cavity

length we evaluated could corresponding to an an integer submultiple of the actual one). Defining $\bar{\lambda} = 782$ nm to be the average value for the measured wavelength, $\Delta\lambda = 91$ pm the observed wavelength jump and n the index of refraction of the diode active medium, it is possible to evaluate the length of the corresponding cavity as:

$$L_{cavity} = \frac{1}{n}\frac{\bar{\lambda}^2}{2(\Delta\lambda)} \qquad (2.24)$$

Where the values used for $\bar{\lambda}$ and $\Delta\lambda$ refer to the laser wavelength in air. The demonstration of this equation is straightforward if the cavity lengh L_{cavity} is expressed as a function of two adjacent modes (i.e. $nL_{cavity} = N(\lambda_N/2) = (N+1)(\lambda_N - \Delta\lambda)/2$). Equation (2.21) gives:

$$L_{cavity} \simeq (1/n)(3.36 \pm 0.04)mm \qquad (2.25)$$

that is in perfect agreement with the actual dimensions of the internal cavity of the diode (refer to appendix B for the diode dimension specifications), if we take into account that a typical value for the diode active medium is $n \simeq 3$. The error has been calculated using the expression :

$$|\delta L_{cavity}| = \frac{\partial L_{cavity}}{\partial \Delta\lambda} \times \delta(\Delta\lambda) = \frac{\bar{\lambda}^2}{2(\Delta\lambda)^2} \times \delta(\Delta\lambda) = \frac{L_{cavity}}{\Delta\lambda} \times \delta(\Delta\lambda) \quad (2.26)$$

We can thus summarize these results saying that fig. 2.32 shows a typical jump mode of the diode laser chip, equal to about 90 pm. The same measurement with the external cavity pointed out a very unstable behaviour of the wavelength that, without the action of the interference filter, seemed to jump randomly among the allowed modes of the internal cavity of the diode.

From the linear fit of the decreasing temperature ramp (shown in fig.2.32), we have that the wavelength versus temperature variation is described by the expression:

$$\lambda(nm) = (56.3 \pm 0.6) \times 10^{-3}T(^\circ C) + (781.659 \pm 0.011) \qquad (2.27)$$

That gives:

$$\frac{d\lambda}{dT} \simeq 56\frac{pm}{^\circ C} \qquad (2.28)$$

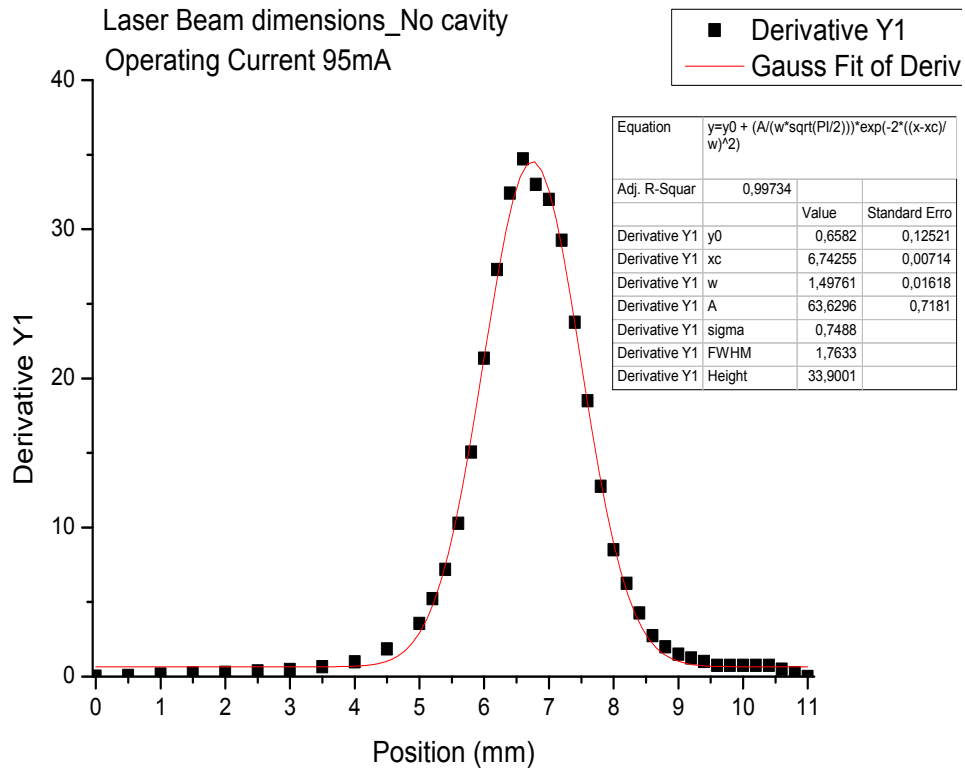as the average variation of the laser wavelength while changing the diode temperature.

Equation	y=y0 + (A/(w*sqrt(PI/2)))*exp(-2*((x-xc)/w)^2)	
Adj. R-Squar	0,99734	
	Value	Standard Erro
Derivative Y1 y0	0,6582	0,12521
Derivative Y1 xc	6,74255	0,00714
Derivative Y1 w	1,49761	0,01618
Derivative Y1 A	63,6296	0,7181
Derivative Y1 sigma	0,7488	
Derivative Y1 FWHM	1,7633	
Derivative Y1 Height	33,9001	

Figure 2.33: THORLABS $L785P090$ diode laser beam dimensions without the external cavity: derivative of the measured transmitted power with respect to the blade position as a function of the latter.

2.5.4 Characterization of the laser beam dimensions

The shape and dimensions of the laser beam were characterized by measuring its emitted power as a function of the position of a metallic blade that partially blocked the laser beam. This measurement was done only for the horizontal direction, i.e. that perpendicular to the laser polarization (along this direction the beam should show the greatest divergence. The typical beam divergence angles given in the diode's datasheet for the directions parallel and perpendicular to the laser polarization are: $\theta_{//} = 9°$ and $\theta_{\perp} = 16°$). We will refer to the position of the blade along this direction with the spatial coordinate x. The derivative of the measured power with respect to x is represented in figures 2.33 and 2.34, for the diode laser itself and for the laser inside the external cavity, respectively. Fitting the experimental points with the Gaussian function:
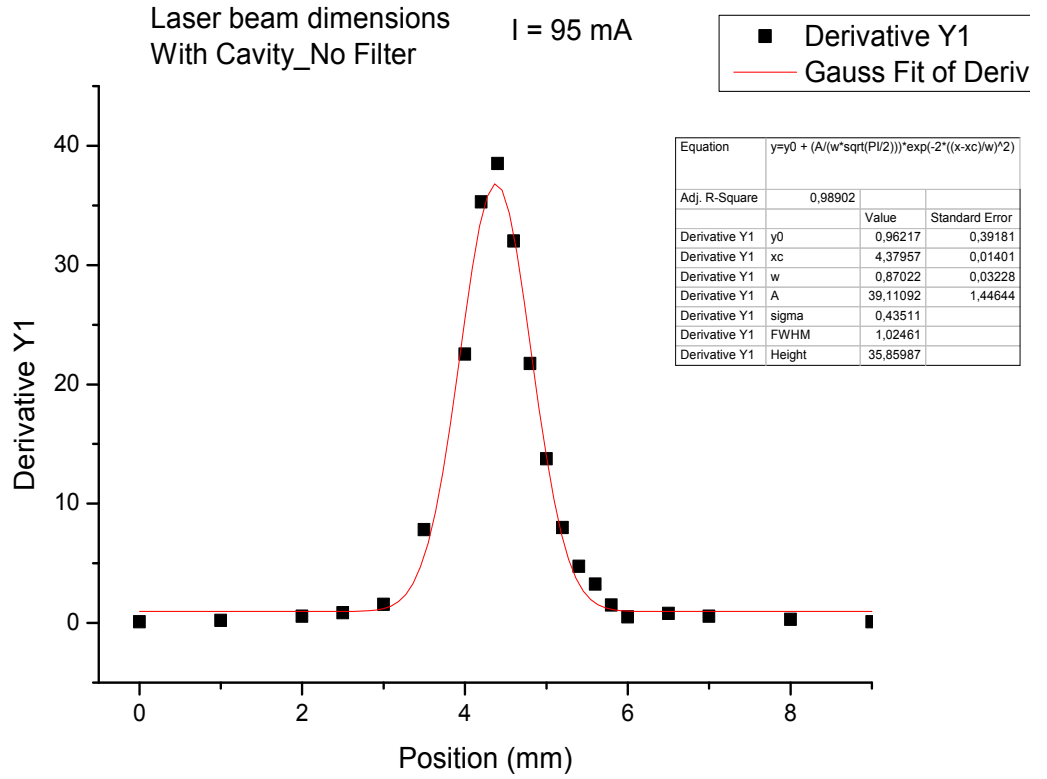
Figure 2.34: THORLABS $L785P090$ diode laser beam dimensions with the external cavity: derivative of the measured transmitted power with respect to the blade position as a function of the latter.

$$Y = Y_0 + \frac{A}{w\sqrt{\frac{\pi}{2}}}e^{-2\frac{(x-x_0)^2}{w^2}} \qquad (2.29)$$

it was possible to obtain for the beam waists:

$$w_{NoCavity} = (1,498 \pm 0,016)mm \qquad (2.30)$$

$$w_{Cavity} = (0,87 \pm 0,03)mm \qquad (2.31)$$

This result can be compared with the one given if we consider the magnification factor of the "cat's eye" scheme: it is the ratio of the focal lengths of the two lenses $L2$ and $L1$ of fig. 2.1:

$$M = \frac{f_{C280}}{f_{C220}} = \frac{11mm}{18,4mm} \simeq 0,6 \qquad (2.32)$$

Then, multipying the beam waist without the cavity by the magnification factor, it is straightforward to see that the result is compatible with the waist of the laser beam with the external cavity (w_{cavity}), given by the gaussian fit:

$$w = w_{NoCavity} M \simeq 0,9 mm \simeq w_{cavity} \tag{2.33}$$

2.5.5 Measurement of the laser beam linewidth without the interference filter

With the scheme shown in fig.2.35 we measured the linewidth of the laser beam after the first collimating lens $C330$. Figures 2.36 and 2.37 shows one of the four measured datasets.
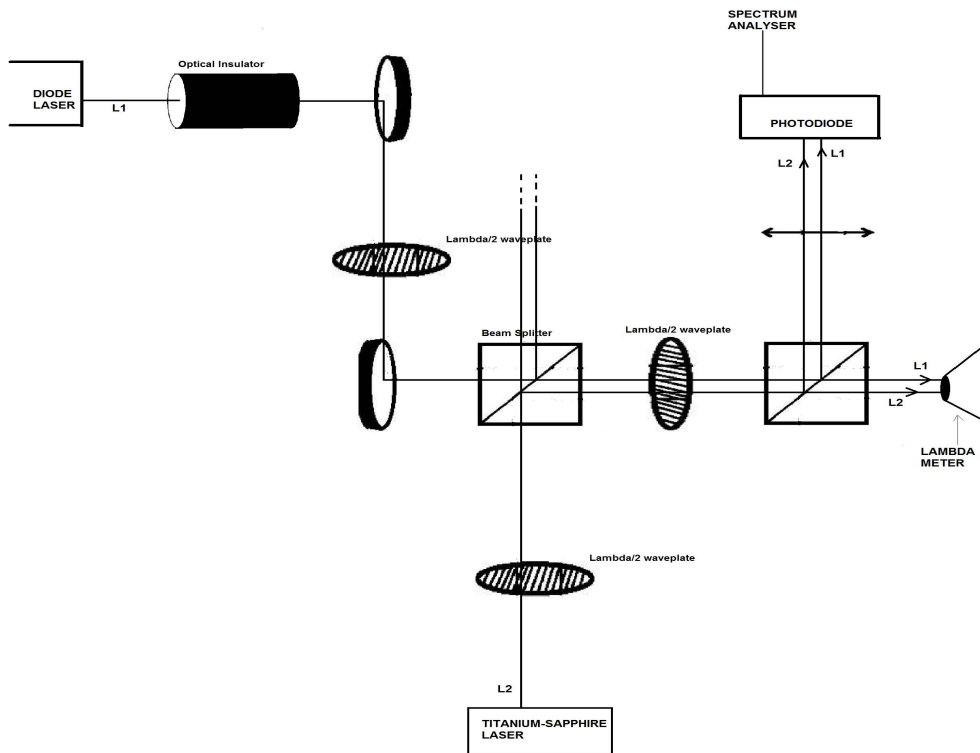

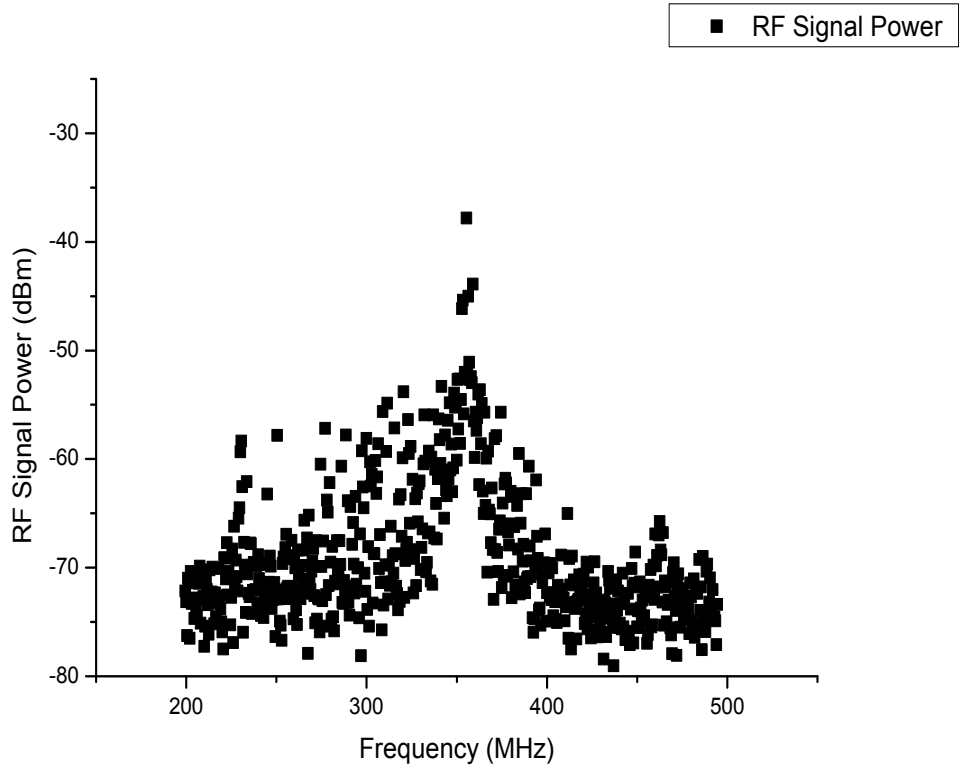Figure 2.35: Optical scheme for the laser linewidth measurement.

Figure 2.36: THORLABS $L785P090$ diode laser characterization: linewith of the output laser beam without the cavity, where the power of the RF signal is expressed in dBm (P[dBm]$= 10 \times Log_{10}(P$[mW]$)$).

We evaluated the laser linewidth with the Lorentzian fitting function:

$$Y - Y_0 = \Big(\frac{2A}{\pi}\Big)\Big[\frac{w}{4(x - x_0) + w^2}\Big] \tag{2.34}$$

and the full width at half maximum (FWHM), given by the four measurement datasets, provided the average linewidth value:

$$Linewidth_{NoFilter} \simeq 10MHz \tag{2.35}$$

Fig. 2.36 plots the power of the RF signal (i.e. the power of the signal at frequencies near 300 MHZ) in dBm units (P[dBm]$= 10 \times Log_{10}(P$[mW]$)$). The linewidth was calculated from equation 2.34 by the evaluation of $2(x_{HM} - x_0)$, where x_0 is the frequency corresponding to the maximum (Y_0) of the Lorentzian function and x_{HM} is the frequency that corresponds to the signal power at half maximum of the curve ($Y_{HM} = Y_0 - 3$dB). On the other hand,
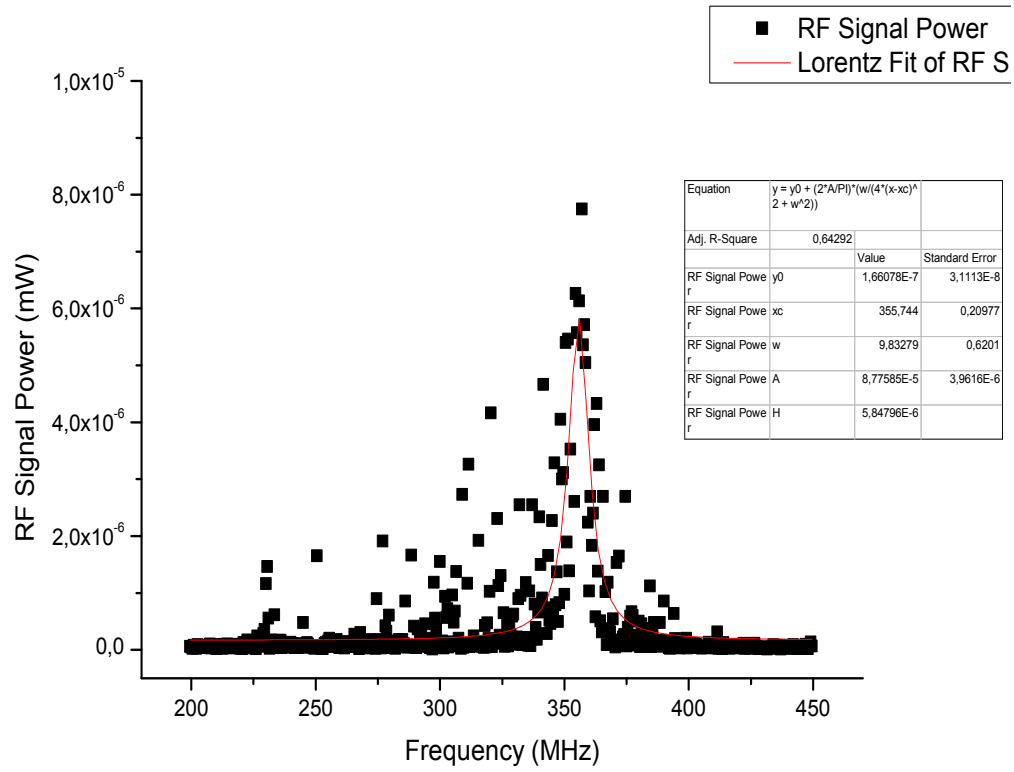
Figure 2.37: THORLABS $L785P090$ diode laser characterization: linewith of the output laser beam without the cavity. The vertical axis shows the power of the RF signal (P) in mW, where $P[\text{mW}]=< V(t)^2 > /(50\Omega)= \sum P(f)Df$. Here f is the RF frequency on the horizontal axis of the spectrum analyzer, Df is the Resolution Bandwidth, $V(t)$ is proportional to the product of the electric fields (E_1, E_2) of the two lasers that realize the beat note and thus P is proportional to $|E_1E_2|^2$.

the vertical axis of fig.2.37 shows the power of the RF signal in mW, and its fit with equation 2.34 gives for the linewidth: $w = (9.8 \pm 0.6)$ MHz.

2.5.6   Laser beam characterization with the interference filter as wavelength selector

We are now going to compare the the results of the previous section with those obtained when the laser wavelength was selected with the interference filter. It was fixed inside part E of fig.2.2 with a small quantity of a two-component adhesive, called $Aremco - Bond631$. Then, by very small displacements of its angular position, we could select the desired transmitted wavelength; in the operating conditions: $I = 105$ mA, $T = 17.25$ °C and $V_{PZT} \simeq 14$ V, we could achieve a wavelength of $\lambda \simeq 780.032$ nm and an output power of about 34 mW. Figures2.38, 2.39 and 2.40, refer to the wavelength characterization for the diode laser that is currently in use.
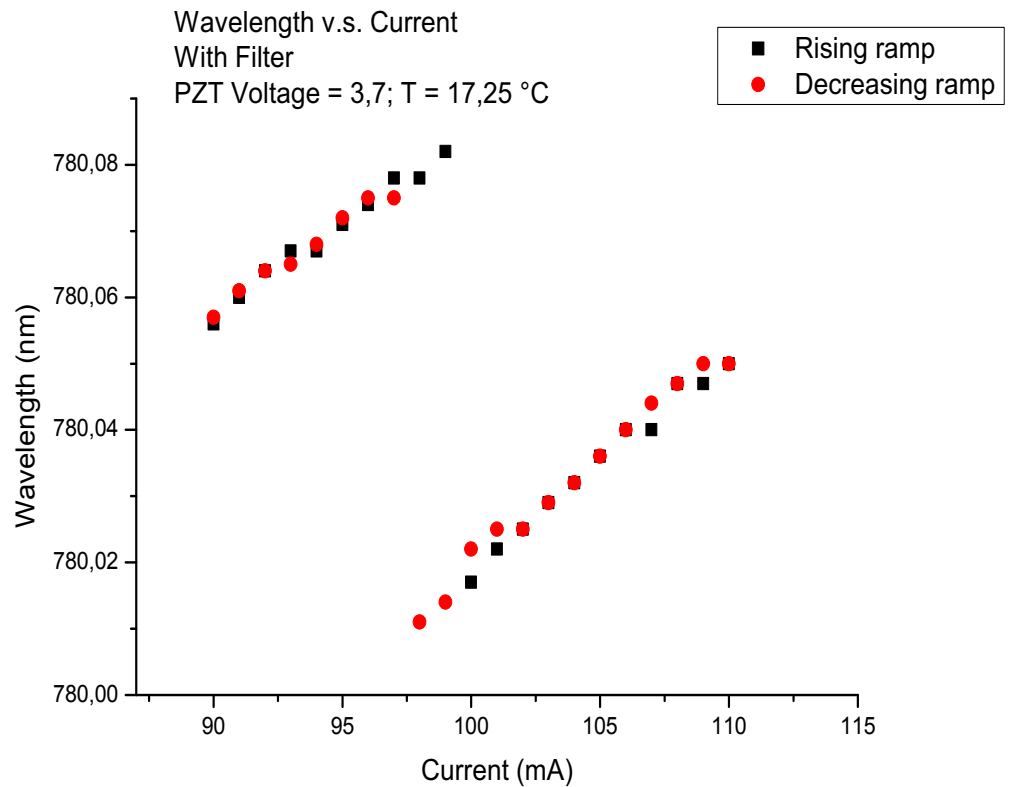

Figure 2.38:   THORLABS $L785P090$ diode laser characterization: interference- filter selected wavelength versus current around the operating current supply region (105 mA). As pointed out in the legend, the black square point dataset represents an increasing current ramp, while the red circular points correspond to the decreasing current ramp. A small hysteresis effect is evident aruond 100 mA and a typical jump mode of the diode cavity is also present around this value.

From Fig2.38, that shows the wavelength behaviour with increasing and decreasing currents, we can appreciate that the operating current supply value (equal to 105 mA) seems to be quite far apart from a typical jump mode of the diode cavity. In fact, taking into account the analysis of the previous section, it is possible to prove that the wavelength jump of 68 pm at $I = 99$ mA is of the typical magnitude of a diode's jump mode.

Variations of the diode temperature and of the tension on the PZT provide a fine scan of the laser wavelength.
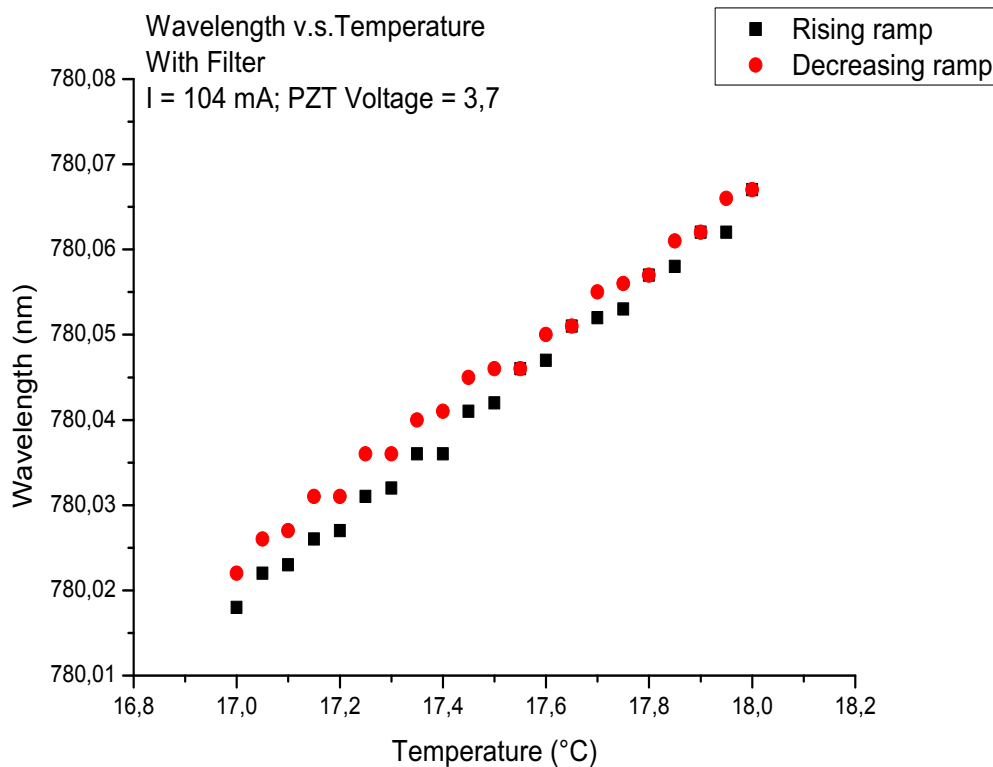

Figure 2.39: THORLABS $L785P090$ diode laser characterization: interference- filter selected wavelength versus temperature, over a restricted temperatures range between 17 and 18 °C. As pointed out in the legend, the black square point dataset represents an increasing temperature ramp, while the red circular points correspond to the decreasing ramp. These measurements were performed with small steps in the diode temperature variations of 0.05 °C and typical wavelength jumps of about 4 pm between the allowed external cavity modes are observable.

The analysis of the wavelength versus temperature and wavelength versus PZT voltage, show that there are jumps of typical megnitude between

the two sets of measurements we did increasing or decreasing the independent variables T and PZT voltage. In fact, from fig.2.39 and 2.40, it is possible to observe jumps in the wavelength between 2 and 6 pm. Proceeding in the same way shown in section 2.5.3, if we take $\bar{\lambda} \simeq 780$ nm and a typical jump mode of $\Delta\lambda = 4$ pm, the length of the corresponding resonant cavity is:

$$L_{Cavity} \simeq (7.6 \pm 2)cm \qquad (2.36)$$

that is compatible with our laser external cavity length of about 8 cm.
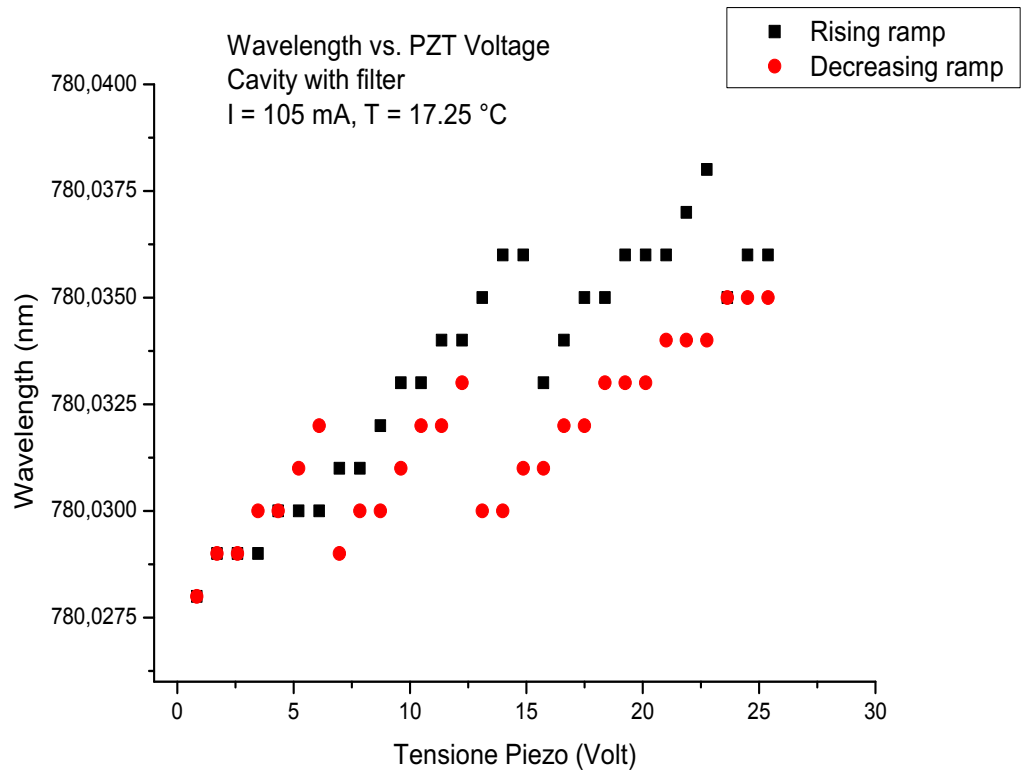

Figure 2.40:   THORLABS $L785P090$ diode laser characterization: interference- filter selected wavelength versus piezo-electric transducer voltage. The legend we used is the same as for the previous graphics and the wavelength is plotted versus the offset voltage on the PZT. A linear fit of the measured offset voltage versus the potentiometer index leads to the index-voltage conversion: $V(Volt) = (4.385 \pm 0.005) \times (Potentiometer_{Index}) + (0.8334 \pm 0.015)$. As in fig.2.39, jumps of the wavelength between the external cavity allowed modes are observable.

We can thus summerize these results saying that, from the curves of

figures 2.32 and 2.38, that report the wavelength behaviour over a large range of temperatures and the wavelength versus current behaviour in the operating region, respectively, it is possible to observe typical wavelength jumps between the diode laser chip modes, equal to many tens of pm. On the other hand, fig.2.39 and 2.40, that represent the fine wavelength behaviour over a restricted temperature range and the curve wavelength versus PZT voltage, shows typical external cavity jump modes (or some integer multiple of them) of about 4 pm.

2.6   Conclusions

Here we summarize the results obtained with the external-cavity diode laser just described in this chapter and we also present some future applications and improvements for the system. First of all, the design of the external cavity described in section 2.3 makes the system particularly good as far as its mechanical stability is concerned. Moreover, the "cat's eye" scheme provides a good optical stability against environmental factors, with respect to the previously used Littrow configuration. Another peculiar difference with respect to grating-stabilized diode lasers is the possibility to optimize the optical feedback and the wavelength selection independently, thanks to the use of a partially reflecting mirror (the out-coupler) and an interference filter that, thanks to its dielectric coatings, acts as a stable wavelength selector, depending on the angle that it forms with respect to the incident laser beam. In fact, with the filter, we could achieve the desired wavelength of 780.032 nm (at the operating conditions: $I = 105$ mA, $T = 17.25$ °C and $V_{PZT} \simeq 14$ V), with a corresponding output power of about 34 mW. The experimental results shown in section 2.5 are a clear evidence of the particular reliability of our laser system, as far as its wavelength stability and tunability are concerned. Indeed, the laser wavelength can be finely controlled by the temperature feedback system (described in section 2.4) and by the voltage on the piezo-electric tranducer (that allows slight variations of the external cavity length and thus to change its typical resonant modes).

To conclude we also notice that, until now, the voltage on the piezo-electric transducer was controlled by hand, changing its offset voltage. A future improvement of the system (that will make this laser suitable for the ultracold atomic physics experiment for which it was developed, in order to cool ^{87}Rb atoms), will involve the development of a feedback system for the PZT, that will simply require small modifications to the present FPGA VI. As we did for the PI temperature controller, another identical $Proportional - Integral$ controller will process the error signal provided by a saturated absorbtion spectroscopy and this will improve the system giving a better wavelength stability.

Chapter 3

Introduction to an UHV system for ultracold atoms experiments

After the treatment concerning the importance of lasers in atomic physics experiments, in this chapter we will present the techniques required to develop ultra-high-vacuum (UHV) systems, that constitute another fundamental feature involved in ultracold atoms experiments. In fact, in order to attain Bose-Einstein condensation, it is not only sufficient to keep the low atomic gas density needed to prevent the atoms from reaching their solid state phase at equilibrium. The other necessary condition is to avoid the thermalization between the atoms and the walls of the trapping chamber. When an atomic gas is trapped inside the chamber, thermalization with the surrounding walls can only be achieved through collisions between the atoms and the particles of the residual gas. For this reason, if the residual gas pressure is extremely low (UHV refers to pressures of the order of $10^{-9} - 10^{-10}$ Pa, corresponding to $10^{-11} - 10^{-12}$ millibar), the number of collisions is considered negligible and atoms condensation can be attained.

In the following we will report the results of the tests we did on a two-dimensional magneto-optical trap ($2D - MOT$), that will be used in the future vacuum apparatus of an ultracold atoms experiment involving the two bosonic species ^{41}K and ^{87}Rb. The experimental techniques required to achieve ultra-high-vacuum will also be described, with particular attention to the choice of the materials used to build up the system, such as the vacuum chamber skeleton, or the adhesive used to to fix the windows. Eventually, from the analysis of our results, we will submit suggestions in order to improve the described experimental vacuum techniques.

3.1   Some basic concept concerning vacuum technology

The first try of a conceptual understanding of vacuum is due to Torricelli, in 1643. Vacuum can be defined as a space region in which gases have been removed, even though not completely. The amount of residual gas determines the vacuum range of the region under consideration. If we assume for the moment that this particular region is a chamber with ideal walls ("ideal" in this case means that the amount of gas trapped or released on the walls is negligible) than, at atmospheric pressure ($P_{atm} = 1$ atm $= 1,01323 \times 10^5$ Pa) and room temperature ($T \simeq 22\ °C$), the air gas particles possess a high thermal energy and they feature a random motion with an average velocity of about $4 - 5 \times 10^2$ m/s. In these conditions the particles continuosly collide together and their paths can be modelled as a series of discrete jumps, where the length of each jump (mean free path) is much smaller than the distance between the particles position and the walls of the chamber. When the pressure inside the chamber is reduced below atmospheric pressure, the characteristics of particles motion are completely different and, at a suitable low pressure value, a molecular regime in which the particles mean free path is greater than the distance between the chamber walls is reached. The following table lists the various regions in which the subatmospheric pressure range is divided.

Degree of vacuum	Pressure Range (Pa)
Low	$10^5 > P > 3,3 \times 10^3$
Medium	$3,3 \times 10^3 > P > 10^{-1}$
High	$10^{-1} > P > 10^{-4}$
Very high	$10^{-4} > P > 10^{-7}$
Ultrahigh	$10^{-7} > P > 10^{-10}$
Extreme ultrahigh	$10^{-10} > P$

Of course, the required vacuum level depends on the specific applications. For example, pressures in the high vacuum range are needed to manufacture low- and high-tech devices or for metal vapors deposition. Applications such as electron microscopy, mass spectroscopy, crystal growth or x-ray and electron beam lithography need operating pressures in the range of very high vacuum. The domain of more interest for us, i.e. ultrahigh vacuum, involves atomic physics experiments, as well as surface analysis and accelerator technology. In these last applications, ultraclean vacuum systems are required and hence UHV is needed to minimize gaseous impurity contamination.

A vacuum system is a combination of pumps, valves and pipes, which creates a region of low pressure. Different kinds of pumps are usually involved and some of them can operate only if a pre-vacuum has already been created. This condition can be fulfilled using rotary vane or piston pumps, that allow to achieve pressures in the range $10^{-1} - 10^{-3}$ Pa. Then, displacement and capture pumps can remove air at these low pressures. Displacement pumps are for example diffusion pumps and turbomolecular pumps, that consist of a system of high-speed rotating blades. On the other hand, also capture pumps can efficiently work at subatmospheric pressure: cryogenic pumps remove gas from a chamber by freezing particles on its walls, getter pumps chemically react with the molecules and ion pumps accelerate the ionized gas particles, that are adsorbed by the metal walls of the pump.

A final observation is needed about the nature of the gases that usually have to be removed. In fact, air is present in every vacuum system and an important quantity that allow to understand how the various constituents are removed by the different kinds of pumps is their partial pressure. In particular, even though the concentration of water vapor is not fixed, but depends on the environmental conditions, at 20 °C a relative humidity of 50% corresponds to a partial pressure of about 1165 Pa [9] and this makes water vapor of great importance when exposure to air is considered. Furthermore, when pressure is lowered below 10 Pa, a significant contribution comes from the amount of gas released by the chamber surfaces. For this reason, other critically important factors (other than the choice of the pumps) when an ultrahigh vacuum system is realized, are the building materials, the surface cleaning techniques and the experimental details of the procedure.

3.2 The vacuum system

This section deals with the $2D - MOT$ chamber we developed and gives both a description of the mechanical parts that constitute it, as well as its characterization, as far as vacuum is concerned.

3.2.1 Description of the 2D-MOT

The $2D - MOT$ chamber is a unique block of titanium (Ti), shaped as a parallelepiped of 185×35 mm^2 each face and a cube, whose sides measure 70 mm. Five faces of the cube are featured by a circular hole of 35 mm diameter: the four lateral sides will be closed with four $CF35$ flanges (thanks to six screws $M3$), while the bottom hole will be connected to a pump, that allow to keep vacuum inside the chamber. The flanges allow a hermetic closure of the holes, that prevents the gas at atmospheric pressure to reach the interior part of the chamber, thanks to a soft copper (Cu) disk that adapts its shape to the flanges, when the screws are tightened. The parallelepiped Ti part is instead characterized by four rectangular holes (having 120×25

mm^2 surface), that will be closed with four glass $BK7$ windows of base area 30×130 mm^2, treated with an antireflection coating. Figure3.1 shows a two-dimensional drawing with the detailed dimensions of the various parts that constitute the chamber and also a three-dimensional drawing of its titanium skeleton. A circular hole, whose diameter measures 16 mm, is present at the edge of the parallelepiped part; before starting the vacuum process it will be closed with a $CF16$ flange.

3.2.2   Behaviour of solids in vacuum

As mentioned before, apart from the choice of the pumps for the specific vacuum system, also that of the materials is of crucial importance in UHV applications. Here we are going to discuss the main causes that affect vacuum due to the materials used in the UHV system, with particular attention to the different characteristics that make Ti more suitable than the more common stainless steel. One other part of the discussion will be dedicated to the two-component epoxy adhesive we used for gluing the windows to the Ti skeleton.

In practice, it is never possible to pump all the gas present inside a chamber, because a certain amount is always dissolved and adsorbed on solids. It is then slowly released and adds to the volume gas that has to be removed by the pumps. We define outgassing the collective gas release from materials and it is actually a result of several processes. Indeed, gas and vapors released from a surface can be due to vaporization, thermal desorption, diffusion, permeation and stimulated desorption, but also depend on the presence of leaks or backstreaming inside the pump (this last two factors are not of the same nature of the previous four, but clearly depend on the reliability of the vacuum setup). Gas release from a surface has the dimensions of energy flow and outgassing is then measured in units of (Pa $\times$ m^3) / s (or equivalently (mbar $\times$ L) / s). Vaporization concerns the incoming of molecules from the solid or liquid state into the vapor phase, due to thermal effects. The vapor pressure of the solid (or liquid) is defined as the pressure of the vapor over the surface, provided that the solid and vapor are in thermal equilibrium. This condition implies a dynamic equilibrium, in which molecules leave the surface at the same rate at which they arrive at it. The contribution of diffusion to the total otgassing comes from the gas transport through the chamber walls to the interior of the vacuum system, followed by desorption into the chamber. The driving force of this process is the gas concentration gradient (due to the gas pressure inside the solid), that drives atoms or molecules to the surface. The general law governing diffusion is called Fick's Law and states that the flux of a material that diffuse into another one is proportional to its concentration gradient [8]:

$$\vec{J} = D\vec{\nabla}c \qquad\qquad (3.1)$$
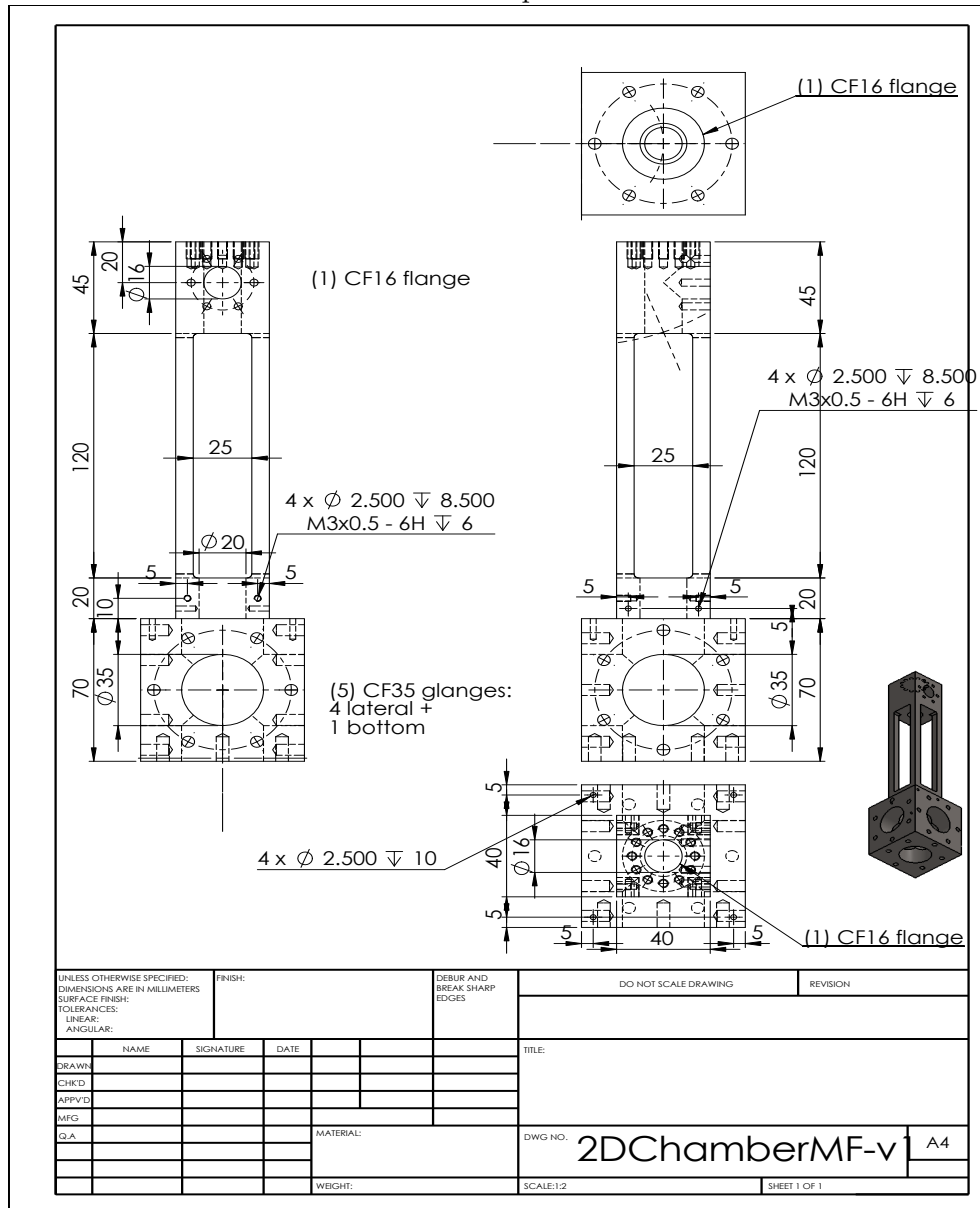
- Sheet1.pdf

Figure 3.1: Drawing of the Ti $2D - MOT$ chamber: the two-dimensional drawing reports the dimensions of the various parts that constitute the chamber, while a three-dimensional model is represented at the right bottom side of the figure.

Where c is the local concentration of molecules or atoms that diffuse, $\vec{J}$ represents the flux of the gas particles through the walls of the chamber and the proportionality constant D is called diffusivity or diffusion coefficient

(they are measured in m^{-3}, m^{-2}s^{-1} and m^{2}s^{-1}, respectively). As diffusion is often much slower than the desorption process, the rate at which gas is added to a vacuum system is usually governed by the rate of diffusive transport from the bulk to the surface. Actually, we observe that, in order to describe desorption from real surfaces, it is necessary to consider higher order effects. In fact, when a particle leaves a surface, it is not immediately removed by the pump in a single bounce, but, in the molecular flow regime, it makes a lot of collisions with other surfaces before encountering the pump entrance. Most of these collisions correspond to a simple scattering, but during some of them the particle can be re-adsorbed by the surface and the rate of desorption is thus lower than its zero-order approximation.

An important tool to reduce outdiffusion and outgassing is to "bake" the vacuum system. Baking is essentially based on thermal desorption, i.e. heat-stimulated release of gases or vapors previously adsorbed on the interior walls of the system. Indeed, the rate of desorption is a function of the molecular binding energy, the temperature of the surface and its extension. When a vacuum system is baked, the most important thing is that all the surfaces are uniformly warmed up, as any small surface not baked will contribute an exceedingly large gas flux, relative to the baked area. As far as outdiffusion is concerned, let us examine the behaviour of the diffusion constant as a function of temperature. It is a function of the thermal activation energy (E_D) of the diffusing gas in the solid:

$$D = D_0 e^{-\frac{E_D}{k_B T}} \tag{3.2}$$

Because outdiffusion depends on the diffusivity D, this exponential dependence implies that a rather small increase in temperature causes a sharp increase of the initial outdiffusion rate [9]. As the gas release from a surface can be modeled as the sum of diffusive release contributions, we find that the net effects of baking are the same as for outdiffusion: a decreased outgassing rate and the reduction of the time required to remove the initial concentration of gas dissolved in the solid. A method used to measure the outgassing is the "throughput method", where the gas is pumped through a known conductance. Experimental results show that the outgassing rate is inversely proportional to a power of time [9]:

$$q_n = \frac{q}{t^{\alpha_n}} \tag{3.3}$$

In equation 3.3, q is the initial outgassing rate, q_n is the outgassing rate after n hours from the beginning of the baking and α_n is an exponent, having 1 as most common value, even though it can range from 0.7 to 2. It is important to point out that the outgassing rate q_n is a function of pumping time after baking. In particular, equation 3.3 is reliable at least within the first 10 hours of pumping from the beginning of the baking.

To conclude we observe that thermal desorption is not the only way that makes gas release from solid surfaces possible. Another class of techniques, collectively called "stimulated desorption" techniques, enable solid surfaces to release adsorbed gases and generate vapors, in order to limit the ultimate pressure in a vacuum chamber. Many of these applications include collisions between energetic particles with the surface and include for instance: electron-stimulated desorption, ion-stimulated desorption, electron- or ion-induced chemical reactions and photodesorption.

3.2.3 Structural materials for the 2D-MOT chamber

When building an UHV system, the relations between a number of factors have to be taken into account. In fact, cleaning, joining parts, construction and applications of the system imply to choose the building materials not only on the base of their individual properties, but also on their compatibility with the rest of the components. For example, baking is necessary to reduce the outgassing rate and reach the lowest possible pressure in UHV systems, but on the other hand, it increases the strain or deformation of stressed parts, due to thermal expansion; besides, thermal decomposition limits the temperature at which some materials can be baked. So, apart from the low outgassing rate and vapor pressure of individual materials, it is also important that their thermal expansion coefficients are as similar as possible, to minimize the stresses.

Metals are used to build vacuum chambers and austenitic steels are the dominant materials of construction, because their high yield strength and easy fabrication. Aluminum was also largely used, but it has been bypassed, expecially because it is difficult to join to other metals.

The following table compares typical values of the outgassing rates of unbaked stainless steel, titanium and pyrex glass [9]. Both values within the first hour (q_1) and within the first 10 hours (q_{10}) of pumping are given. Also the thermal expansion coefficients α are reported for these materials.

Material	Outgassing	(Unbaked Materials)	α
	q_1 (10^{-7} Pa-m/s)	q_{10} (10^{-7} Pa-m/s)	($10^{-6}m/°C$)
Stainless Steel	1200	267	$\simeq 17$
Ti	150	24.5	8.6
Glass (Pyrex)	98.0	7.3	4.0

As it is possible to notice from the table, one of the reasons why we chose Ti for the $2D - MOT$ chamber is because its thermal expansion coefficient is more similar to that of glass than the stainless steel α coefficient. An-

other reason is because, during its fabrication, stainless steel traps hydrogen molecules, that need high baking temperatures (over 300 °C) to be released. On the other hand, gas release from Ti surfaces requires lower baking temperatures (near 150 °C) and this allow to reduce mechanical stresses due to the thermal deformations and the risk of thermal decomposition of some component of the system (such as the adhesive used to fix the windows to the chamber).

The adhesive we used to glue the windows to the Ti $2D - MOT$ chamber is $Aremco - Bond$ 631. It is a two-component epoxy, used in UHV applications and is the base resin used for many other adhesives delivered by the same company. The most important specifications reported in the product datasheet are the extremely low outgassing rate, given as the percentage of its mass vaporization, technically called total mass loss (TML) and the maximum fraction of the volatile material that can condensate on a surface, called collected volatile condensable materials ($CVCM$). During a curing time of 7 days at 25 °C, $Aremco - Bond$ 631 presents a TML equal to 0.75% and a $CVCM$ of 0.35%. These are satisfying values, if considered that, generally, a TML of 1.0% or less and a $CMCV$ of 0.10% or less are desired for spacecrafts. Another important feature of this epoxy is that its liquid and solid specific volumes are very similar, thus reducing mechanical stresses while curing the adhesive (look to subsection 3.2.4 for the curing process description).

3.2.4   Measurements and results

Before assembling the vacuum system, we accurately cleaned all the windows and the internal surfaces of the metallic chamber with acetone. Then, with the chamber horizontally placed on the working desk, in order to fix the windows to the Ti skeleton, a thin continuous line of liquid $Aremco - Bond$ 631 adhesive was laid within a distance of 2.5 mm from the interior borders of the window holes in the metallic chamber (from fig.3.1 it is possible to observe that this is the linear extension of the contact between the windows and the Ti chamber along the long sides of each hole, while this distance is 5.0 mm along the short sides). The rectangular windows were then put on it and the curing process for the glue solidification was performed: $18-24$ hours at room temperature followed by $24 - 48$ hours at 60 °C. It is important to observe that, during the gluing of the windows, to prevent the liquid adhesive from reaching the internal surfaces of the vacuum chamber, we did not exert any pressure on them (the only pressure present was due to their weight) and this is also the reason why the thinnes of the glue strip and the horizontal position of the chamber were important. Indeed, in spite of the fact that $Aremco - Bond$ 631 adhesive has a low outgassing rate, we wanted to limit the sources of gas release inside the vacuum system. We also point out that the windows could not been fixed at the same time, because a curing

process for each of them was required. After the chamber assembling, each entrance was closed with the suitable flange and a vacuum pump *AGILENT TPS BENCH* was screwed to the bottom round entrance of fig.3.1, to test the vacuum performance of our system. *AGILENT TPS BENCH* consists of a turbomolecular pump, having a nominal rotational speed of 1700 rpm, attached to a rotary vane pump that creates a pre-vacuum state, suitable for the turbomolecular pump working conditions. A test of the base pressure achieved with this pump (the base pressure is defined as the pressure achieved after 48 hours pumping, with the turbopump fitted with a flange), gave the result: $P_{Base} \simeq 10^{-8}$ mbar, and we will take this as a reference value in the next treatment. In the following we will present the results obtained with the tests on the $2D - MOT$ vacuum chamber, at first without bake the system and then during and after baking.
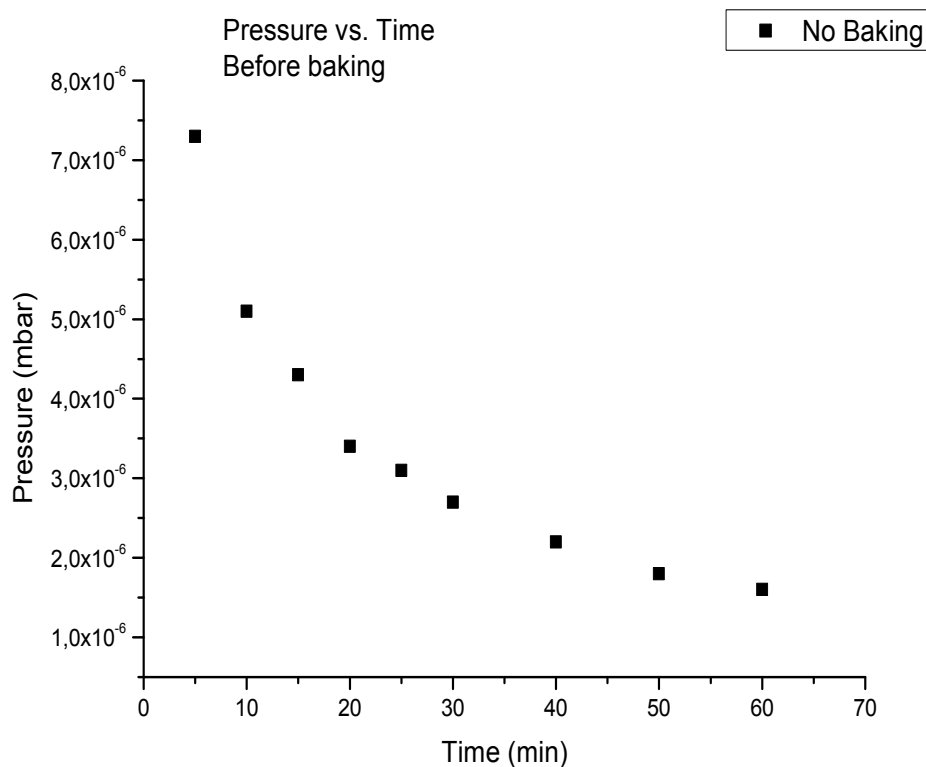

Figure 3.2: $2D - MOT$ vacuum chamber characterization: pressure versus time curve before baking.

Figure3.2 shows the pressure as a function of time before the system was baked. Not displayed in the graphic, after 16 hours of pumping we reached a pressure of 1.6×10^{-7} mbar and, at this point, we started the

baking of the vacuum system. It was performed wrapping the chamber with two aluminum sheet layers, with a heating strip in between. The strip was winded to the $2D - MOT$ as homogeneously as possible because, as maintained in the previous section, even small non baked surfaces can cause the baking process to be completely useless. Then, thanks to a thermocouple placed in thermal contact with a window, we increased the temperature at the constant slow rate of $1 - 2$ °C/min (in order to minimize the stress due to thermal strain), to about 90 °C. Figures3.3 and 3.4 report the curves of temperature and pressure versus curves, during baking.
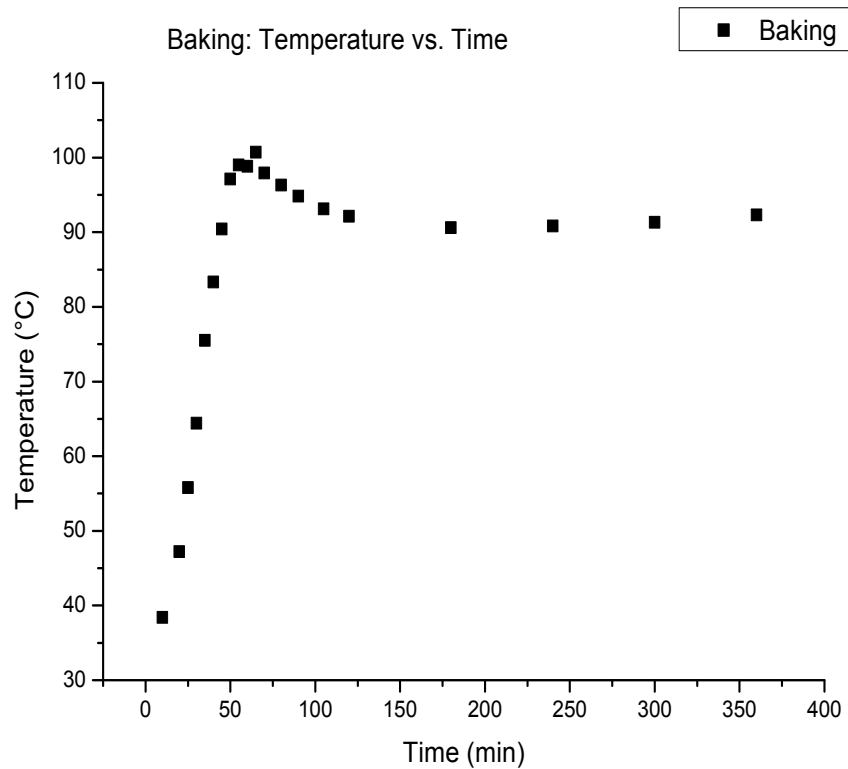
Figure 3.3: $2D - MOT$ vacuum chamber characterization: temperature versus time curve for the baking process.

As expected, there is an initial growth in the pressure, when baking is started, as most of the gas trapped on the inner surfaces of the chamber is released during the first part of the process. Acoordingly to fig.3.4 there is then a second phase in which the pressure reaches a maximum and then decreases. A third part of a baking process, that involves longer time scales with respect to the previous two, should show a point at which pressure, from a constant value, starts to diminish and should furter decrease (below
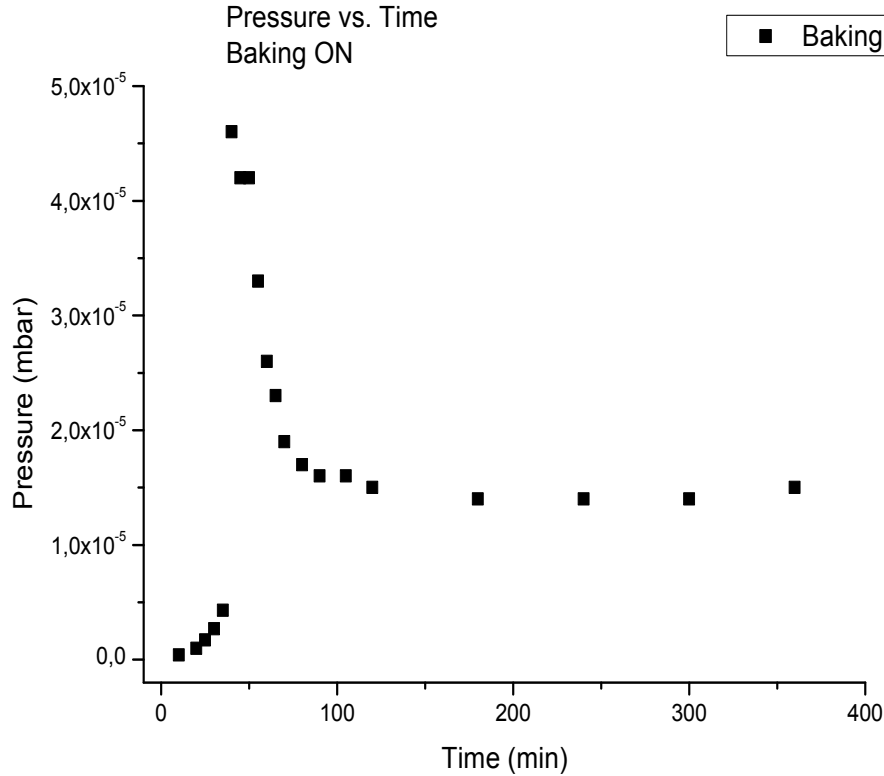
Figure 3.4: $2D - MOT$ vacuum chamber characterization: pressure versus time curve during the baking process.

the value it had before baking) when the baking is turned off. To the contrary, we did not observe the pressure to reduce below 1.4×10^{-5} mbar and, after two days at about 94 °C, the pressure inside the chamber was still fixed at 1.6×10^{-5} mbar. Finally, the presence of gas flowing inside the vacuum chamber was confirmed by the fact that the pressure was increased to 1.9×10^{-5} mbar after two days the baking was turned off.

Two possible causes were: gas released due to vaporization of the adhesive at high temperature (in fact the vapor pressure of a substance increases exponentially with temperature) and the presence of leaks in the adhesive layer. The first option was finally excluded when the pressure inside the chamber dropped abrouptly to 1.6×10^{-7} mbar (and then to 9.2×10^{-8} mbar after 20 minutes) when acetone was spilled along the perimeter of each windows, temporarily closing the leaks.

We decided to use the specific adhesive Torr-Seal to close leaks and finally it was possible to obtain the expected results. Torr-Seal is a thick, non-flow paste that requires a curing time of 24 hours at 25 °C or 2 hours at 60

°C. We put Torr-Seal along the whole perimeter of each window, obtaining, without baking, a pressure of 7.6×10^{-8} mbar after one day of pumping. These result are plotted in fig.3.5.
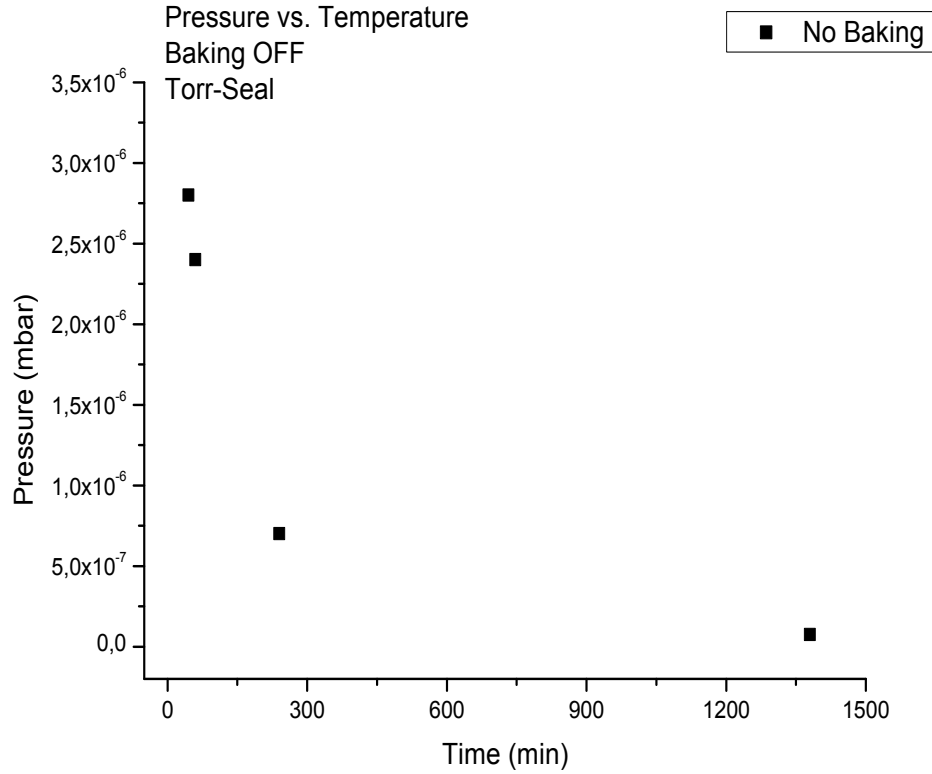

Figure 3.5: $2D - MOT$ vacuum chamber characterization: pressure versus time curve with Torr-Seal, before baking.

Following the same procedure as before, we baked the vacuum chamber and now it was possible to observe the typical pressure versus time behaviour expected for baking: the pressure initially increased until it reached a maximum value of 2.4×10^{-6} mbar at the maximum temperature of 97.3 °C, after 6 hours baking. It was then followed by a decreasing trend, until the value of 1.7×10^{-7} mbar was reached after 4 days of baking at a constant temperature of about 94 °C (this last value is not reported in fig.3.6).

Finally, baking was turned off (it is described by the regular decreasing temperature ramp shown in fig.3.7) and the data obtained within the first eight hours are plotted in fig.3.8. The final lowest pressure was achieved after 23 hours (from the moment corresponding to the beginning of the bake off), with the system at room temperature. The result is:
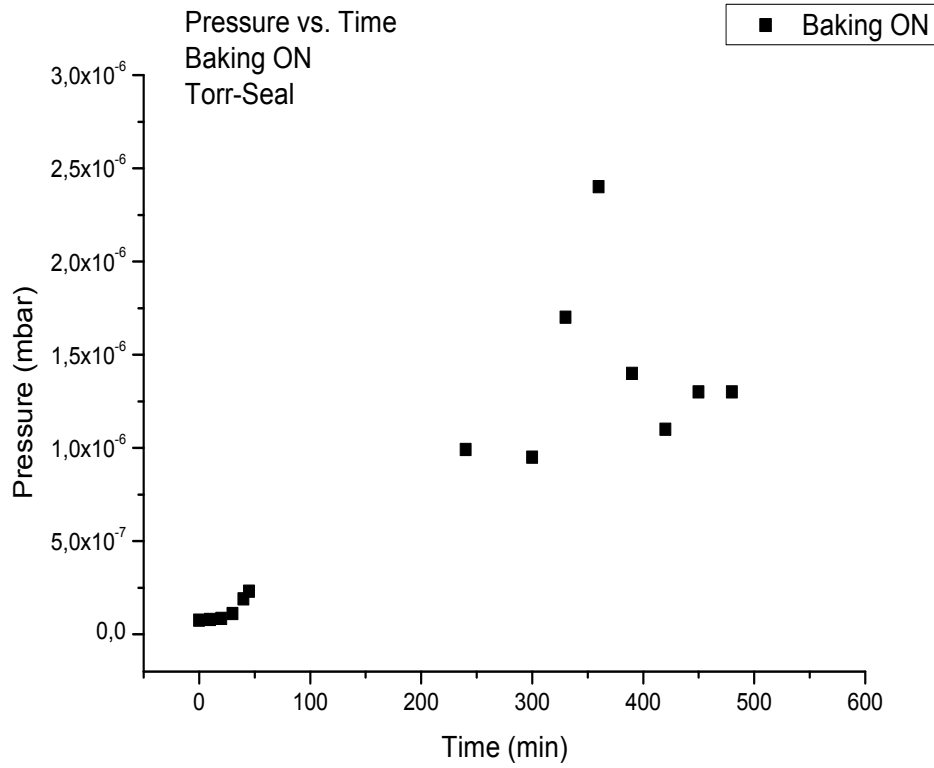
Figure 3.6: $2D - MOT$ vacuum chamber characterization: pressure versus time curve during the baking process, after Torr-Seal was put to close leaks.

$$P_{Lowest} = 2.5 \times 10^{-8} mbar \tag{3.4}$$

However Torr-Seal can't be considered the definitive solution, due to the fact that it has a low decomposition temperature (about 100 °C).
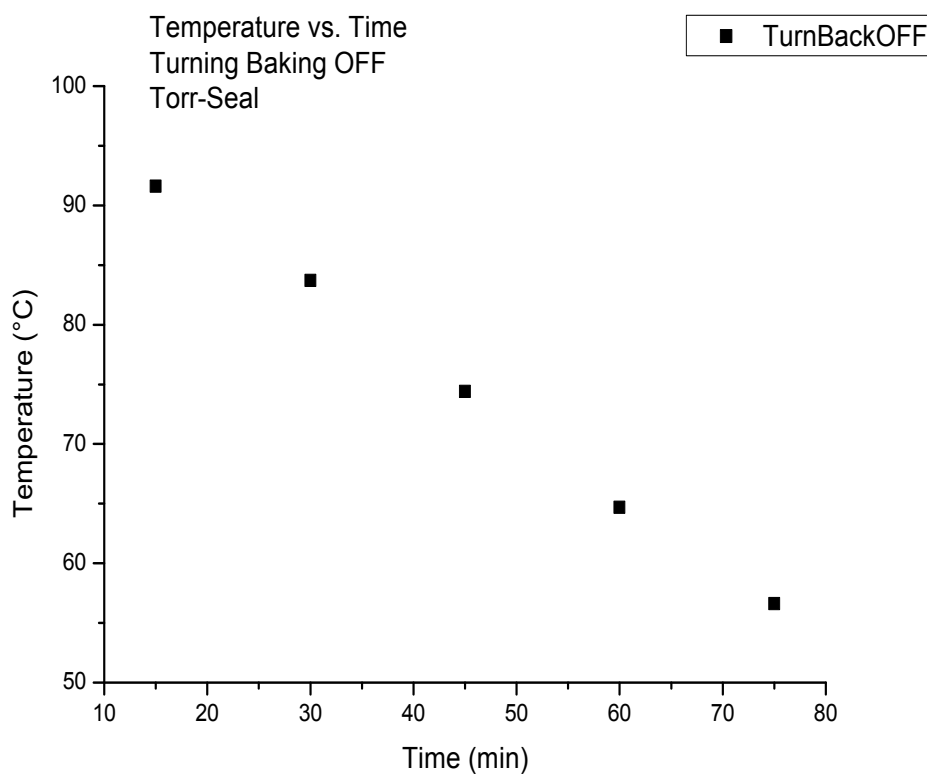
Figure 3.7: $2D - MOT$ vacuum chamber characterization: temperature versus time curve while the baking was turned off.

3.3   Conclusions

From the results presented in subsection 3.2.4 we can conclude that it was not initially possible to achieve the desired pressure near 10^{-8} mbar because there were leaks in the layer of adhesive between the titanium support and the windows. The most probable reason was a failure in the procedure used for gluing them. In fact, in order to limit the spread of the adhesive to the inner surfaces of the vacuum chamber, no pressure was made on the windows when they were put on the glue layer. This prevented an intimate contact with the metallic chamber, causing the appearance of a great number of leaks after few days.

It is therefore a necessary condition for future applications to press each window on the metallic support during the fixing process. On the other hand, as a consequence, a greater amount of adhesive could be spread inside the chamber. Despite the extremely low outgassing rate of $Aremco - Bond$ 631, the effect of gas release inside the vacuum chamber can be further
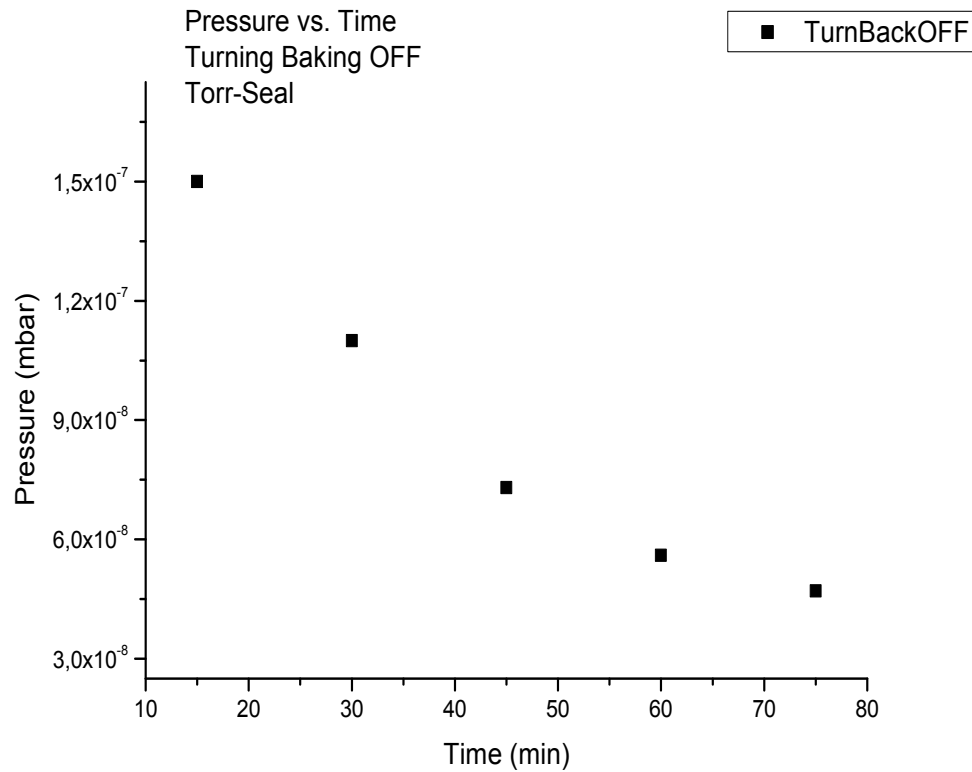
Pressure vs. Time
Turning Baking OFF
Torr-Seal

Figure 3.8: $2D - MOT$ vacuum chamber characterization: pressure versus time curve with Torr-Seal, after baking.

limited if other glues, such as $Master\ Bond\ EP30LTE - LO$ or $Master\ Bond\ Supreme\ 10AOHT$, are used. Even though high performances are ensured by $Aremco - Bond\ 631$ for UHV applications, these two adhesives present exeptionally low thermal expansion coefficients ($4 < \alpha < 5 \times 10^{-8}$ m/°C), very low shrinkage upon cure and outgassing rates even lower than that of $Aremco - Bond\ 631$.

Conclusions

The work presented in this thesis demonstrated the development of an external-cavity diode laser, that uses an interference-filter as wavelength selector and an upgraded vacuum system for an experiment with ultracold atoms. Despite the fact that vacuum and laser techniques are very basic aspects in ultracold atoms experiments, they have at the same time a crucial role.

In the last chapter we introduced to the techniques for the realization of an ultra-high-vacuum system, with a particular focus on the peculiar characteristics that make a certain material suitable for this kind of applications. We also pointed out the details of the experimental procedure involved, because, as pointed out by our results, the UHV technology involved in ultracold atoms experiments requires a continuous improvement, in order to ensure long time reliability.

In the second chapter we showed that a laser system featured by an external cavity ensures a particularly good mechanical stability. Moreover, the "cat's eye" scheme we employed, provides a better stability against optical misalignment, with respect to the common Littrow configuration previously used in grating-stabilized diode lasers. The peculiar feature of our system is also to exploit an interference filter as wavelength selector and a partially reflecting mirror in a "cat's eye" configuration, thanks to which it is possible to optimize the wavelength selection and optical feedback independently. We also treated the development of a feedback system for the diode and external cavity temperature stability and could demonstrate the high reliability of our system, expecially as far as its wavelength tunability and stability are concerned. Indeed high controlled wavelength selection and stabilization, within a resolution of the order of 1 pm, can be achieved and the future development of a feedback system for the external cavity length control through a piezo electric transducer (PZT), can further improve these performances. We can thus conclude that our laser can be considered a suitable system for applications in ^{87}Rb laser cooling and, in general, the laser design presented in this work is a good candidate for future laser cooling techniques.

Appendix A

LabVIEW implementation of FPGA and Real-Time Stand-Alone applications

In this section we describe the realization of LabVIEW FPGA and Real-Time Stand-Alone applications on a Single-Board RIO device. The purpose of a Stand-Alone application is to allow a Virtual Instrument placed in the LabVIEW Project to run automatically on your National Instrument device, without being controlled through a Windows OS interface.

A.1   FPGA Stand-Alone Applications

The implementation of Stand-Alone applications is performed from a Windows OS interface, with the Single-Board RIO device connected to the Windows OS processor. Our starting point is represented in fig.A.1: we assume that the FPGA Virtual Instrument has already been compiled from the VI Front Panel; after compilation, a target of an executable file named as the FPGA VI appears in the Project Explorer Window, as indicated in the figure. The following procedure will be schematically divided into steps.

Step (1): right-click the FPGA target and select the option "RIO Device Setup". In the menu that appears walk to the "Device Setting" tab and put a checkmark on the option "Autoload VI on device reboot" (refer to fig.A.2).

Step (2): right-click the target of the executable file corresponding to the FPGA VI and select "Properties". In the menu that appears mark the option "Run when loaded to FPGA" (see fig.A.3).

Step (3): compile the FPGA VI from the Virtual Instrument Front Panel, to take steps (1) and (2) into account.

Step (4): right click the target of the FPGA Virtual Instrument and select the option "Download VI to Flash Memory".
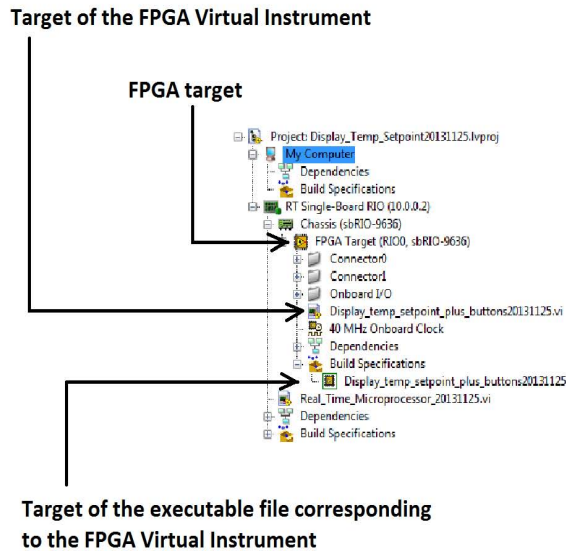
Target of the FPGA Virtual Instrument

FPGA target

```
Project: Display_Temp_Setpoint20131125.lvproj
  My Computer
    Dependencies
    Build Specifications
  RT Single-Board RIO (10.0.0.2)
    Chassis (sbRIO-9636)
      FPGA Target (RIO0, sbRIO-9636)
        Connector0
        Connector1
        Onboard I/O
        Display_temp_setpoint_plus_buttons20131125.vi
        40 MHz Onboard Clock
        Dependencies
        Build Specifications
          Display_temp_setpoint_plus_buttons20131125
    Real_Time_Microprocessor_20131125.vi
    Dependencies
    Build Specifications
```

Target of the executable file corresponding
to the FPGA Virtual Instrument

Figure A.1: Project Explorer Window: this window represents the structure of the LabVIEW project. In the figure, the FPGA target represents the FPGA chip on the Single-Board RIO device. The FPGA Virtual Instrument target is the FPGA VI itself and once it is compiled from the Virtual Instrument Front Panel, a target of an executable file named as the FPGA VI appears in the Project Explorer Window, as indicated.

At this point, when the device is not connected to a Windows OS processor, the FPGA Virtual Instrument will run automatically on the Single-Board RIO each time the device is powered.

A.2   Real-Time Stand-Alone Applications

A Real-Time Stand-Alone application has the same meaning of that described in section A.1 for the FPGA processor. The only conceptual difference is that the first one is implemented by the Real-Time microprocessor on the Single-Board RIO device. As in the previous section, the procedure
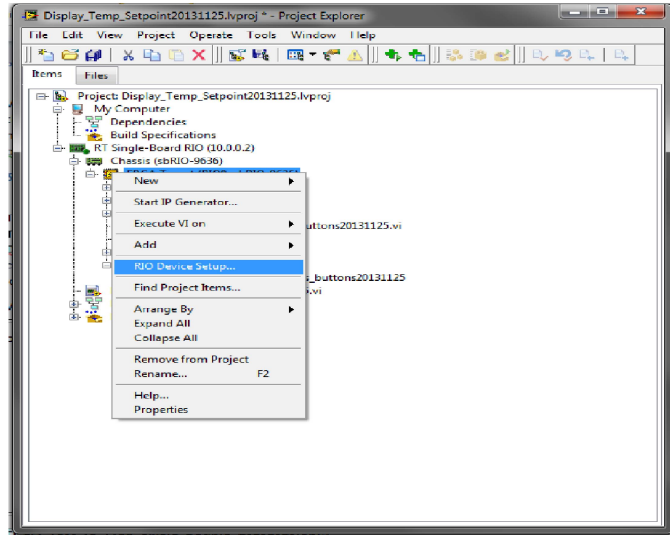
Figure A.2: FPGA Stand-Alone application: step (1).

will be schematically described in different steps.

We start from figure A.5 and proceed in the following way:

Step (1): first of all you have to create an executable of your Real-Time Virtual Instrument. In the Project Explorer Window right-click on the target labelled Build Specifications in fig.A.5 (notice that this target is placed under the Real-Time microprocessor, in the hierarchy of the project). Select "New" >> "Real-Time Application" (fig.A.6). In the menu that appears go to "Category" and choose "Source Files". Now it is possible to add the Real-Time VI of which you want to create an executable to the window named "Startup VIs", as shown in fig.A.7.

Step (2): save the project: "File" >> "Save All".

Step (3): in the Project Explorer Window right-click on the target Build Specifications and select "Build All" (refer to fig.A.8).

Step (4): right-click on the target of the executable file corresponding to the Real-Time VI and choose "Run as startup" (fig.A.9).

Now, as for the FPGA Stand-Alone application, the Real-Time Virtual Instrument will run automatically on the Single-Board RIO each time the device is powered, independently from a Windows OS interface.
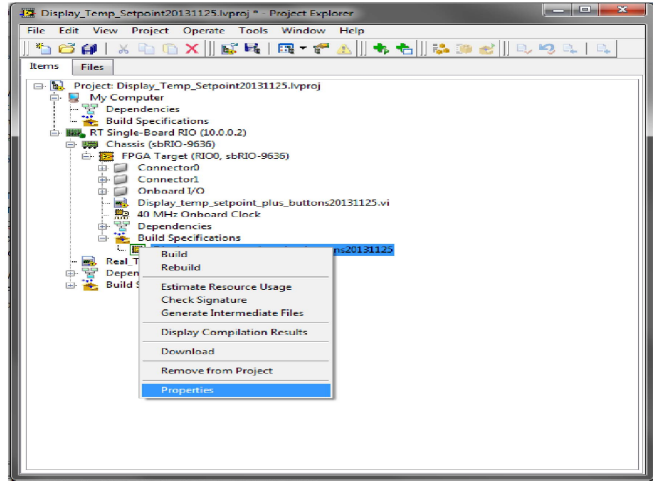
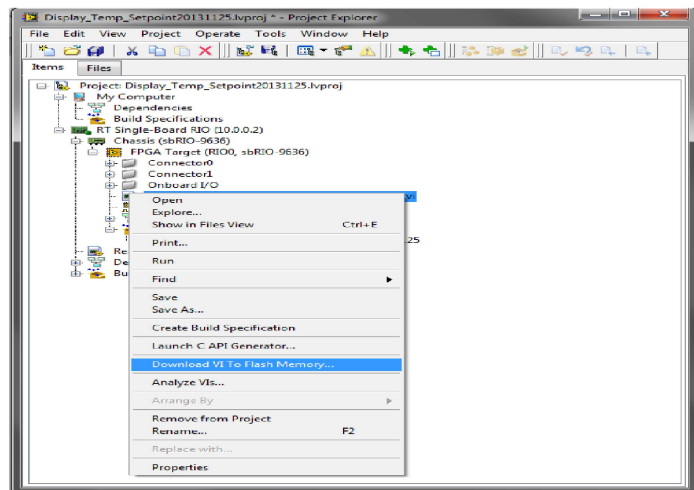Figure A.3: FPGA Stand-Alone application: step (2).

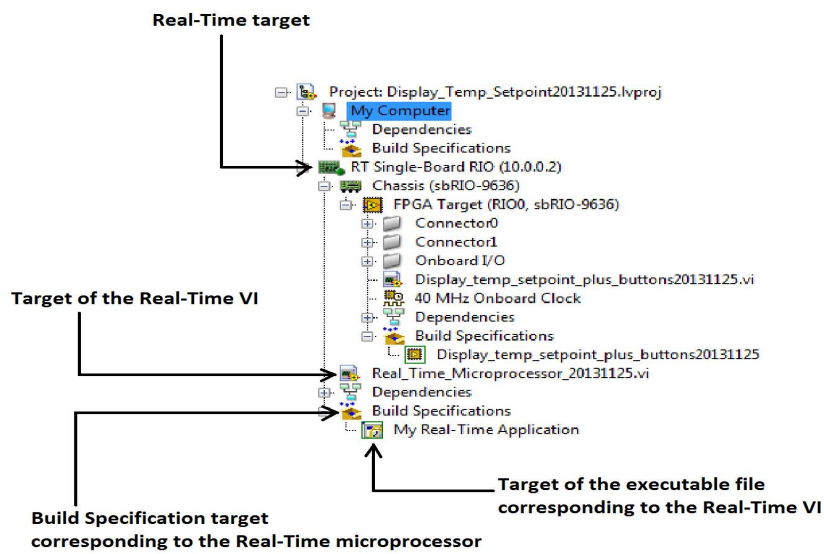Figure A.4: FPGA Stand-Alone application: step (3).

Real-Time target

Target of the Real-Time VI

Project: Display_Temp_Setpoint20131125.lvproj
My Computer
Dependencies
Build Specifications
RT Single-Board RIO (10.0.0.2)
Chassis (sbRIO-9636)
FPGA Target (RIO0, sbRIO-9636)
Connector0
Connector1
Onboard I/O
Display_temp_setpoint_plus_buttons20131125.vi
40 MHz Onboard Clock
Dependencies
Build Specifications
Display_temp_setpoint_plus_buttons20131125
Real_Time_Microprocessor_20131125.vi
Dependencies
Build Specifications
My Real-Time Application

Target of the executable file corresponding to the Real-Time VI

Build Specification target corresponding to the Real-Time microprocessor

Figure A.5: Project Explorer Window: the Real-Time target represents the Single-Board RIO Real-Time microprocessor. The Real-Time VI target is the Virtual Instrument that implements Real-Time operations. Finally, the target placed to the bottom of the figure represents an executable file, thanks to which it is possible to realize the desired Real-Time Stand-Alone application.
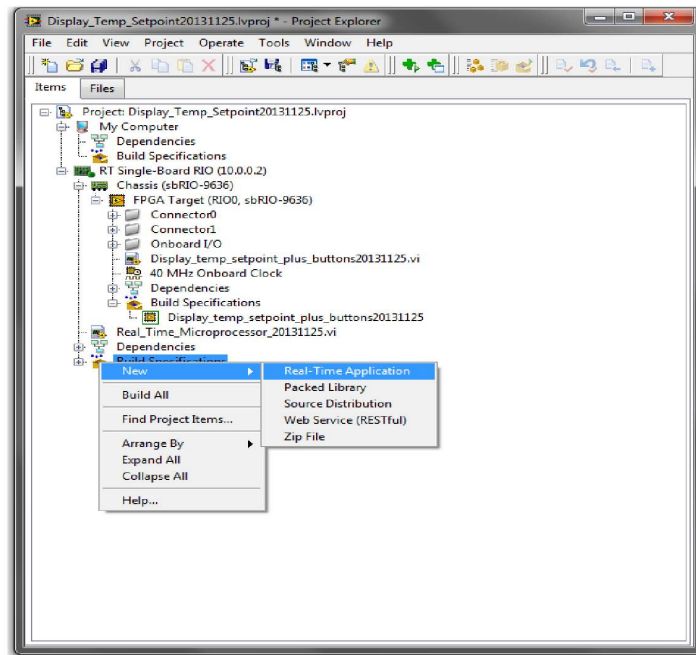
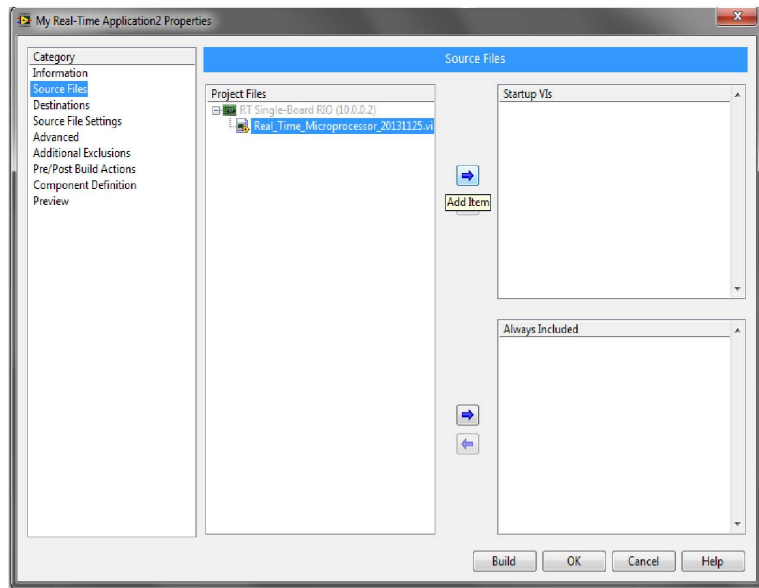Figure A.6: Real-Time Stand-Alone application: step (1).

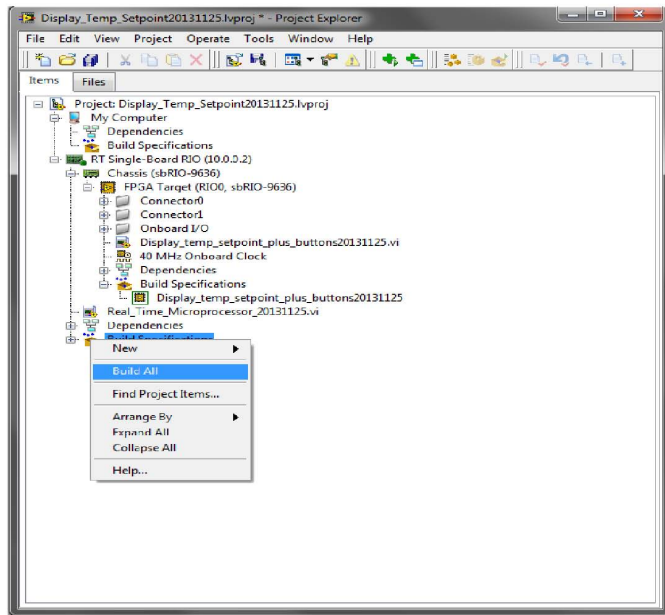Figure A.7: Real-Time Stand-Alone application: step (1).

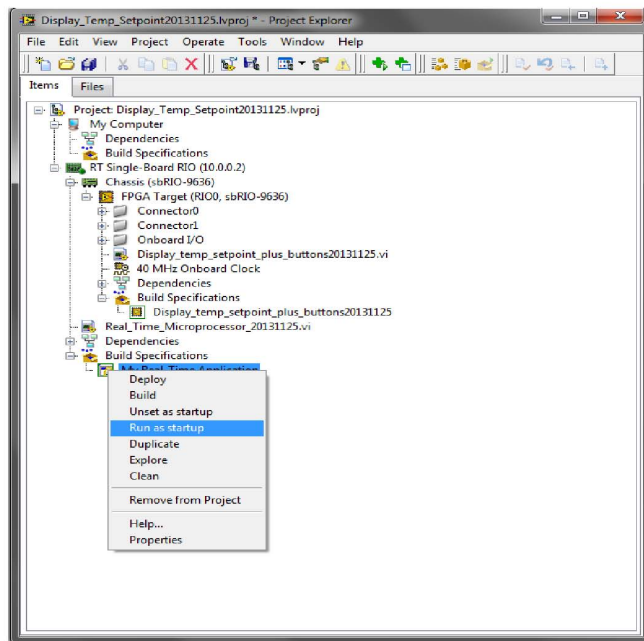Figure A.8: Real-Time Stand-Alone application: step (3).

Figure A.9: Real-Time Stand-Alone application: step (4).

Appendix B

Thorlabs-L785P090 diode laser specifications

In this section we report the characteristics of the diode laser we employed in the system described in chapter 2. It emits at a typical wavelength of 785 nm, 90 mW output power and is featured by a 5.6 mm package. We report the product specification sheet for the details of the diode laser pin diagram (fig.B.1), dimensions (fig.B.2) and typical values for its parameters, at working conditions (fig.B.3).
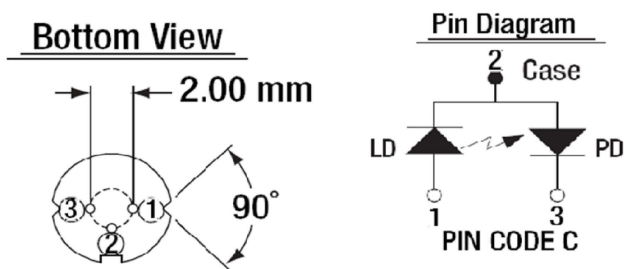

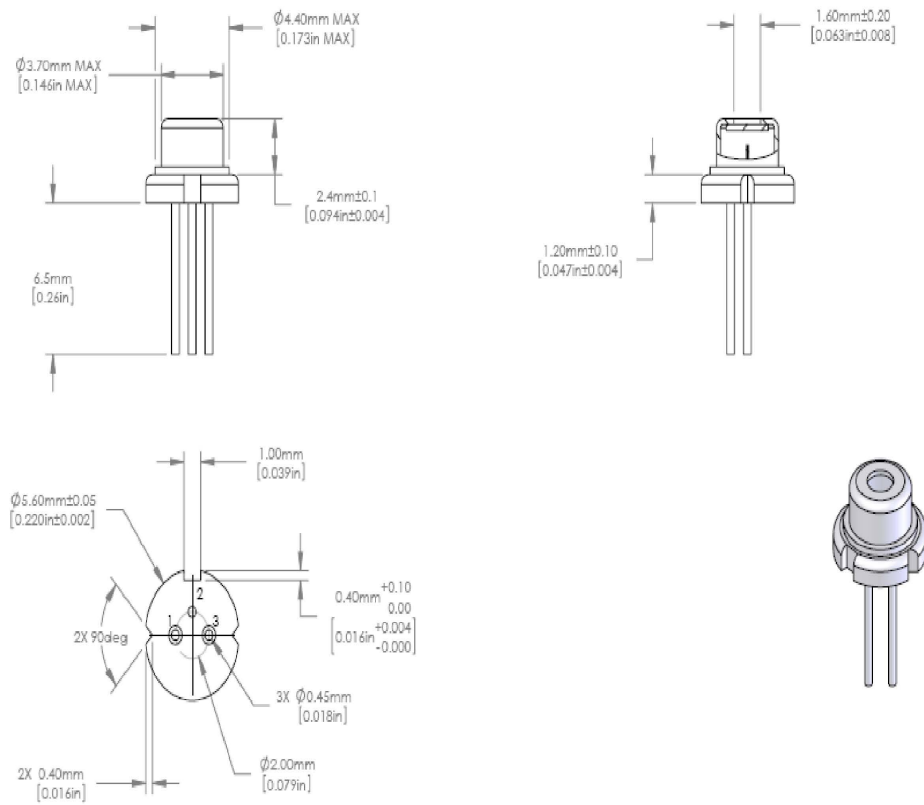Figure B.1: Pin diagram of the cathode grounded Thorlabs-L785P090 diode laser.

Figure B.2: Thorlabs-L785P090 diode laser: dimension specifications.

Absolute Maximum Ratings (T$_c$ = 25 °C)

Specification	Symbol	Value
Optical Output Power	P$_o$	100 mW
LD Reverse Voltage	V$_{r(LD)}$	2 V
PD Reverse Voltage	V$_{r(PD)}$	30 V
Storage Temperature	T$_S$	-40 to 85 °C
Operating Case Temperature	T$_C$	-10 to 70 °C

Typical and Measured Characteristics (T$_c$ = 25 °C)

Specification	Symbol	Min	Typical	Max
Lasing Wavlength*	λ$_p$	775 nm	785 nm	795 nm
Optical Power	P$_o$	-	90 mW	100 mW
Threshold Current*	I$_{th}$	-	35 mA	60 mA
Operating Current*	I$_{op}$	-	120 mA	160 mA
Operating Voltage*	V$_{op}$	1.5 V	2.0 V	2.3 V
Slope Efficiency*	η	0.7 W/A	1.1 W/A	1.4 W/A
Astigmatism	As	-	-	15 μm
Monitor Current	I$_m$	0.3 mA	0.5 mA	1.0 mA
Beam Divergence*	θ//	8°	9°	10°
	θ⊥	15°	16°	20°
Beam Angle Deviation*	θ//	-2°	-	2°
	θ⊥	-2°	-	2°
Emission Point Accuracy	ΔX	-80 μm	-	80 μm
	ΔY	-80 μm	-	80 μm
	ΔZ	-80 μm	-	80 μm

*P$_o$ = 90 mW

Figure B.3: Thorlabs-L785P090 diode laser: manufacturer specifications for the diode's parameters at working conditions.

Bibliography

[1] C. J. Pethick and H. Smith, *Bose-Einstein Condensation in Dilute Gases*, Cambridge University Press, 2002.

[2] R. K. Pathria and P. D. Beale, *Statistical Mechanics*, Third Edition, Elsevier, 2011.

[3] H. J. Metcalf and P. van der Straten, *Laser Cooling and Trapping*, Springer, 1999.

[4] C. E. Wieman and L. Hollberg, *Using diode lasers for atomic physics*, Rewiew Article, 2 August 1990.

[5] L. Ricci et al., *A compact grating-stabilized diode laser system for atomic physics*, Elsevier, 15 June 1995.

[6] X. Baillard, A. Gauguet, S. Bize, P. Lemonde, Ph. Laurent, A. Clairon, P. Rosenbush, *Interference-filter-stabilized external-cavity diode lasers*, Elsevier, 5 May 2006.

[7] A. Yariv, *Optical Electronics in Modern Communications*, Oxford University Press, 1997.

[8] R. W. Balluffi, S. M. Allen, W. C. Carter *Kinetics of Materials*, John Wiley & Sons, 2005.

[9] J. F. O'Hanlon, *A User's Guide to Vacuum Technology*, Third Edition, John Wiley & Sons, 2003.